CENTRO DE INVESTIGACIONES
EN OPTICA, A.C.

"LENSLESS MICROSCOPY USING PARTIALLY COHERENT SYNTHETIC LIGHT SOURCES: EFFECTS ON THE RESOLUTION OF THE RECONSTRUCTED OBJECT"

Thesis to obtain the degree of Master of Science (Optics)

Presents: Miguel Angel Orjuela Moreno, B. Sc.

Thesis director: Geminiano Donaciano Martínez-Ponce, Ph. D.

Approved by:
Geminiano Martínez Ponce, Ph. D.

Final version: Includes changes suggested by reviewers.

León · Guanajuato · México
August 2025

Dedicated to
my Mother,
Miriam Moreno,
my Father,
Alejando Orjuela,
and
especially to my great friend, Sheldom.

No, my dog watched me giving me the necessary
attention
the necessary attention
to make a vain man understand
that being a dog,
with those eyes, purer than mine,
he wasted time, yet he watched me
with the gaze he reserved for me
throughout his sweet, his furry life,
his silent life,
near me, without ever bothering me,
and without asking anything of me.

Pablo Neruda

Aknowledgements

I wish to express my gratitude to my advisor, Geminiano Martínez Ponce, Ph. D., for all the support provided since my arrival at CIO, for his invaluable advice, knowledge, and time dedicated to my formative process.
I thank each member of the GILPI research group for their contributions and recommendations in the development of this project. I also thank the Centro de Investigaciones en Óptica A.C. (CIO) for giving me the opportunity to continue my academic projects, especially the researchers with whom I had the chance to share ideas, as well as the members of DFA for their friendship and unconditional support throughout these years.

I would like to thank the members of my evaluation committee: Geminiano Martínez Ponce, Ph. D., Juan Manuel López Tellez, Ph. D., and Ana Karen Reyes, Ph. D., for all their comments and suggestions that helped bring this project to a successful conclusion. I also wish to thank the *Secretaría de Ciencia, Humanidades, Tecnología e Innovación (SECIHTI)* for the scholarship granted during these two years.

Finally, I would like to express my deepest gratitude to my family—my mother, father, and siblings—who gave me their full support throughout this time and who also helped care for Sheldom. Without their unconditional support and dedication, I would not have been able to carry out this project. I also thank my friends in Colombia for their constant calls and companionship during difficult times, and in Mexico, Gabriel and Pedro for all their support since my arrival to pursue my studies here, as well as the friends I have made in Mexico who have turned this into a second home.

Abstract

This research addresses limitations in lensless holographic microscopy with highly coherent sources, particularly speckle noise. We propose and validate a Schell-Gaussian illumination source with adjustable spatial coherence to optimize system resolution and robustness.
The illumination source was implemented and characterized using rotating diffuser disks, demonstrating that rotation velocity effectively suppresses speckle by transforming the intensity distribution from exponential to Gaussian - indicating improved uniformity. Constant interference fringe visibility in Young's experiment confirmed characteristic Schell-Gauss behavior regardless of slit displacement.

Evaluation of autofocus metrics identified Intensity Variance and Local Contrast as most precise, exhibiting sharper peaks and lower uncertainty with reduced coherence. Speckle suppression significantly improved resolution, decreasing the limit from 22.09 μm to 17.59 μm, and further to 9.8 μm (from 11.0 μm) using a high-resolution sensor. The system demonstrated multi-plane focusing capability and effective operation with biological samples. This study validates spatial coherence control as fundamental for optimizing resolution and image quality in lensless digital holographic microscopy, establishing foundations for designing accessible high-performance systems.

Keywords: Spatial coherence, diffraction, autofocusing metrics, visibility, contrast.

Contents

Figure list

Chapter 1

Introduction

Despite significant advances, conventional microscopy faces inherent limitations associated with the use of refractive optical elements. The presence of lenses introduces chromatic and monochromatic aberrations that necessitate complex compensation designs, increasing both technical sophistication and implementation costs. These constraints motivate the development of alternative approaches such as lensless holographic microscopy, which eliminates the need for intermediate optical elements between the object and sensor, offering advantages in portability, mechanical simplicity, and reduction of systematic aberrations.

A critical aspect in these systems is the nature of the illumination source. While highly coherent laser sources guarantee high resolution, they present drawbacks such as speckle noise patterns, high cost, and safety requirements. Partially coherent sources emerge as a promising alternative, but their impact on the spatial resolution of the reconstructed object requires rigorous characterization.

Here we propose that the use of engineered sources with tunable spatial coherence (Schell-Gaussian model) enables optimization of the trade-off between resolution, cost, and system robustness. This hypothesis is grounded in the fact that the degree of spatial coherence modulates digital hologram formation, directly affecting the transfer of spatial frequencies and the recoverable resolution. Validating this premise requires systematically characterizing how key source parameters (coherence width, angular distribution) relate to resolution metrics in test objects.

This research addresses this challenge through structured objectives combining experimental implementation, quantitative characterization, and performance evaluation, aiming to establish optimal design guidelines for accessible, high-performance lensless microscopy systems.

1.1 Objectives

1.1.1 General objective

Evaluate the effects of the degree of spatial coherence of an illumination source on the resolution of the reconstructed holographic image in a lensless microscopy system.

1.1.2 Specific objectives

- Implement and characterize a synthetic partially coherent light source of the Schell-Gaussian model type based on a rotating optical diffuser.

- Implement and characterize a lensless microscopy system for the generation of holographic images of an object of interest.

- Quantitative evaluation of the effects of the spatial coherence set in the synthetic illumination source on the resolution of the reconstructed object with the lensless microscopy system.

1.2 Justification

One limitation of conventional microscopy is precisely the use of basic elements such as lenses. When implemented in an optical setup, they necessitate compensating for unwanted contributions to the system such as aberrations, whether chromatic or monochromatic depending on the experimental configuration. In this context, developing lensless microscopy techniques becomes essential, as they would eliminate the need to compensate for the aforementioned effects while enabling the design of systems that maintain good resolution, significant cost efficiency, and yield compact, portable assemblies when implemented. Characterizing the lateral resolution of the optical system developed and implemented for this project is critically important, since the proposed illumination sources for implementation are partially coherent sources. These are lower-cost alternatives to high-coherence sources such as lasers.

This research project aims to generate new knowledge in digital in-line holographic microscopy by proposing the use of illumination sources with adjustable spatial coherence. The effects of this light property will be evaluated in the resolution of the reconstructed image of the object under study.

1.3 State of the Art

1.3.1 Introduction to Lensless Microscopy

Microscopy has been a fundamental technique since its invention in the 16th century, revolutionizing numerous fields of knowledge, particularly biology. [1] However, traditional lens-based optical microscopy presents inherent limitations, such as the relationship between spatial resolution and field of view. [2] Additionally, the presence of lenses can introduce aberrations that distort the image and limit resolution. [3, 4] Conventional microscopic systems tend to be costly and require complex configurations. [5] Furthermore, the analysis of biological samples requires labeling, which can be invasive and alter the sample's natural properties. [6, 7]

As a promising alternative addressing these limitations, *lensless microscopy* has emerged. [8, 9, 10] This technique is based on holography principles, initiated by Dennis Gabor in 1948 with his proposal of a *new microscopic principle* to overcome lens limitations in electron microscopy. [11] Gabor's original concept, known as in-line holography or Gabor holography, involved recording an interference pattern (hologram) between a reference wave from the source and an object wave scattered by the sample. [12, 6] Subsequently, object image reconstruction was achieved by illuminating the hologram with a wave similar to the reference wave. [6]
With the advent of digital sensors (CCD and CMOS sensors) and increased computational capacity, optical reconstruction has been replaced by numerical algorithms. [6, 13, 14, 15] This variant, known as digital in-line holography (DIH), has established itself as a key lensless microscopy technique. [14]

Lensless microscopy, and particularly DIH, offers significant advantages over conventional microscopy. Unlike lens-based systems, it avoids optical aberrations associated with lenses. [16, 17] Lensless microscopy devices can be compact, portable, and low-cost, [18, 19] making them particularly attractive for point-of-care applications or resource-limited settings.
Another crucial advantage, especially for biological applications, is the ability to operate with label-free samples. [20] DIH enables retrieval of both amplitude and phase information from the complex optical field, [21, 22] which is valuable for analyzing transparent biological structures. Moreover, from a single two-dimensional hologram, pseudo-3D reconstructions of volumetric objects can be performed, [23] and the technique can be faster for large-volume analysis than scanning techniques like confocal microscopy (which, while improving detail by blocking out-of-focus light, requires point-by-point or line scanning). [24] The simplicity of the in-line configuration contributes to its ease of operation. [18, 25, 7] Various biological applications, including studies of blood cells, spermatozoa, [2, 7] parasites, [26] and cell culture analysis, have been successfully demonstrated using this technique. [20]

1.3.2 The Role of Coherence in Holographic Microscopy

By its very nature, holography requires sufficient coherence between the object wave and reference wave to generate stable interference patterns that can be recorded as holograms. [5] The coherence properties of the illumination source – both temporal and spatial – fundamentally influence light propagation [27] and the quality of the resulting image.

Traditionally, Gabor's in-line holography employed high-coherence sources, such as lasers spatially filtered through small pinholes, to ensure well-defined hologram formation. [12, 28] However, to achieve more compact and cost-effective systems, the use of spatially or temporally partially coherent sources like LEDs (light-emitting diodes) or LDs (laser diodes) has been explored. [9, 29] Although these sources are more accessible and suitable for portable devices, [18, 30] their coherence length is significantly shorter than that of highly coherent lasers.

The use of partially coherent sources presents challenges in lensless holographic microscopy. Numerical reconstruction algorithms, being based on wave diffraction and propagation theory (such as Fresnel methods [6, 31]), often assume fully coherent illumination. This can affect the quality of the reconstructed image. Experimental studies have analyzed the performance of lensless microscopy under partially coherent illumination, [32, 9, 9] finding, for example, that autofocus algorithms designed for highly coherent light do not perform as effectively. [6] Resolution capability may also be influenced by the source type (LED vs LD) and sample distance. [9] Moreover, attempting to improve the spatial coherence of an LED using very small spatial filters does not always enhance resolution and may reduce available light intensity, increasing exposure times. [9]

The relationship between coherence and resolution remains an active research topic in optics. [33, 34, 35] It has been demonstrated that in imaging systems with obstacles in the Fourier plane (analogous to certain microscopy scenarios), reducing the degree of spatial coherence may in some cases improve image quality but inevitably introduces distortions. [35] These effects can be interpreted by decomposing the partially coherent source into a set of coherent pseudo-modes, where modes with specific characteristics (such as maxima at obstacle edges) are responsible for the distortions.

Lensless holographic microscopy with partially coherent sources (primarily LEDs) has been demonstrated for various biological applications and in low-cost portable devices. [2, 14] For instance, portable lensless microscopes have been developed using LEDs coupled to multimode fibers or for detecting waterborne parasites. [8, 36] Recent work describes the development of low-cost, automated portable microscopes employing multi-height and multi-spectral phase retrieval methods with LEDs as illumination sources, achieving resolutions of approximately 5 μm. [7] However, most of these studies utilize sources with a partial coherence degree that is fixed by the source's intrinsic properties (such as LED chip size) or modified in a

limited manner with simple spatial filters. [9] While it is recognized that coherence affects performance, systematic investigation into how **controlled variation of spatial coherence** quantitatively affects **the resolution of reconstructed objects** in lensless holographic microscopy (DIH/Gabor) appears to be an area requiring more detailed exploration.

Theoretical and experimental work exists on generating sources with controllable spatial coherence, such as Gaussian-Schell model (GSM) sources, Multi-Gaussian Schell-model sources, [35] or non-uniformly correlated (NUC) sources, [37] along with methods to independently control the field statistics and irradiance of partially coherent beams. It has been demonstrated that adapting the spatial coherence structure of illumination can improve image quality in systems with obstacles, achieving results comparable to obstacle-free systems. [35] Nevertheless, the specific application and systematic study of these controllable-coherence sources to evaluate their direct impact on object reconstruction resolution in a digital in-line holographic microscopy (lensless) configuration is not prevalent in the reviewed literature.
This research project lies at the intersection of lensless microscopy, digital holography, and the study of spatial coherence of light, addressing a fundamental question: How does controlled variation of the spatial coherence of the illumination source affect the resolution at which objects can be reconstructed in a lensless digital holographic microscope?
The relevance of this project rests on several key points:

1. **Maximizing advantages of lensless microscopy:** Lensless microscopy offers significant potential due to its portability and wide FOV, making it ideal for decentralized applications and resource-limited settings. [20] However, its performance, particularly resolution, is intrinsically linked to the properties of the illumination source used. [38] A deep understanding of how spatial coherence influences resolution is crucial for optimizing the design of these systems and expanding their practical applications.

2. **Addressing a specific knowledge gap:** While the importance of coherence in holography is recognized [9, 39] and its general effect on image quality, [40] a systematic study quantifying the impact of varying the spatial coherence of the illumination source on reconstruction resolution in a DIH setup, using sources specifically designed to vary this parameter, is not widely documented. Existing projects with partially coherent sources typically use sources with fixed coherence (LEDs), [18] without exploring the gradual influence of different coherence levels.

3. **Development of optimal illumination strategies:** By understanding the relationship between spatial coherence and resolution, more sophisticated illumination strategies can be developed. This could involve designing sources with specific spatial coherence profiles tailored to the application (e.g., optimized for resolving certain types of biological samples) or developing more robust reconstruction algorithms capable of compensating for the effects of partial or non-uniform coherence. [41, 33]

Controllable-coherence sources provide the necessary experimental tool for conducting this fundamental research.

4. **Improvement of numerical reconstruction:** The problems observed with reconstruction and autofocus algorithms under partially coherent illumination [9] highlight the need to adapt these methods to controllable illumination conditions. Investigating how different coherence levels directly impact reconstruction quality will provide valuable data for implementing autofocus metrics and their application in holographic reconstructions of complex optical fields.

Compared to other techniques, this project focuses on optimizing the performance of lensless DIH/Gabor microscopy through a fundamental understanding of the illumination source's spatial coherence role. While traditional microscopy is constrained by lenses and the resolution-FOV trade-off, lensless microscopy overcomes this. Techniques such as SA (Synthetic Aperture) or PSR (Pixel Super-Resolution) enhance resolution at the cost of increased hardware or computational complexity but remain limited by partially coherent illumination quality. This project does not seek to replace these techniques but rather to understand and potentially mitigate a fundamental limitation imposed by the light source, providing a foundation for designing better lensless systems from first principles.
In summary, developing a lensless microscope with a controllable spatial coherence illumination source is highly relevant because it enables systematic quantitative investigation of a key optical parameter (spatial coherence) and its direct effect on reconstructed image resolution in a minimal-component microscopic system with high potential (lensless DIH). This will contribute to optimizing lensless microscope design and implementing reconstruction algorithms based on autofocus metrics adapted to partially coherent illumination sources, thereby advancing the adoption of this technology across diverse applications, particularly in biological domains.

1.3.3 Methodological Approach

The project will address this research by combining a digital in-line holographic microscopy setup with a light source enabling controlled variation of its spatial coherence by using rotating diffuser disks. Digital holograms of test objects will be recorded at different levels of controlled spatial coherence. Subsequently, numerical reconstruction algorithms based on the Fresnel transform and angular spectrum propagation will be applied to obtain reconstructed images of both amplitude and phase of the complex optical field. Resolution analysis will be performed using standard test targets (such as the USAF 1951) and autofocus metrics to determine the optimal focal plane, establishing how the resolution of reconstructed features varies with the degree of spatial coherence of the illumination. This integrated experimental-computational methodology is expected to quantify the relationship between source spatial coherence and image resolution in lensless digital holographic microscopy.

Chapter 2

Theoretical framework

In this chapter, some of the fundamental principles governing lensless Gabor microscopy will be explored. Topics such as interference and diffraction, the influence of the source's spatial coherence on hologram formation, and how these factors affect contrast metrics (fringe visibility) and system resolution criteria will be addressed. Furthermore, two of the most widely used numerical reconstruction techniques will be examined, along with how they enable the extraction of quantitative and morphological information from various study samples. This foundation supports applications in digital holographic microscopy with partially coherent illumination sources.

2.1 Interference

Holography emerged from the pursuit of improved resolution in microscopy (initially electron microscopy). Gabor's fundamental idea, which he initially termed wavefront reconstruction, was to record not only the intensity of light but also the complete wavefront information, including its amplitude and phase. [5]

Recall that a wave represents a disturbance in the electromagnetic field caused by a moving electric charge. Furthermore, associated with the electric field are a magnetic field and a direction of propagation. The simplest mathematical expression for an electric field is:

$$\vec{E}(z,t) = \vec{E_0}(t)\cos(kz \pm \omega t + \phi(t)) \tag{2-1}$$

where k relates to the spatial period of the wave and ω is its angular frequency. The description could alternatively be formulated in terms of the magnetic field; however, laboratory detectors are more sensitive to electric fields, given the known relationship $|\vec{E_0}| = c|\vec{B_0}|$. Therefore, in subsequent discussions on wave interference, we will specifically refer to the interference of electric fields.
Since physical recording media, such as the photographic plates originally used, are only

sensitive to light intensity, interference between two waves becomes the fundamental optical principle for achieving this recording. [42]

For observable interference between two optical waves to occur, four fundamental conditions based on the concept of coherence are primarily required:

1. **Wave Superposition**: The two waves must meet and overlap at the same point in space and at the same instant in time. The resulting intensity at that point is the coherent sum of the complex amplitudes of the two waves.
2. **Coherence**: The electric field amplitude and absolute phase do not vary during the observation time.
3. **Polarization**: The two waves must be in the same polarization state (the electric field vectors must be parallel).
4. **Bandwidth**: The spectral content or wavelengths should be minimal (quasi-monochromatic).

If the electric field amplitude in (2-1) and the phase ϕ are constant, then it takes the form:

$$E(z,t) = E_0 \cos(kz \pm \omega t + \phi) \tag{2-2}$$

Assuming two waves with these characteristics, both quasi-monochromatic and having the same polarization state, represented by:

$$\vec{E}_1 = E_{01} e^{i(kz-\omega t+\phi_1)} \hat{e}_1$$

$$\vec{E}_2 = E_{02} e^{i(kz-\omega t+\phi_2)} \hat{e}_2$$

Then, the superposition of these two waves will be represented by:

$$\vec{E}_T = \vec{E}_1 + \vec{E}_2 \tag{2-3}$$

And irradiance is defined as the time average of $\vec{E}_T \cdot \vec{E}_T^*$, where $(*)$ denotes the complex conjugate of the field, i.e. [43]

$$I = \frac{1}{2}\varepsilon_0 c \langle \vec{E}_T \cdot \vec{E}_T^* \rangle$$

$$I = \frac{1}{2}\varepsilon_0 c \langle (\vec{E}_1 + \vec{E}_2) \cdot (\vec{E}_1 + \vec{E}_2)^* \rangle$$

$$I = \frac{1}{2}\varepsilon_0 c \left[\vec{E}_{01}^2 + \vec{E}_{01}^2 + 2\vec{E}_{01} \cdot \vec{E}_{02} \cos(\phi_1 - \phi_2) \right] \tag{2-4}$$

And if $\vec{E}_{01} = \vec{E}_{02}$, (2-4) reduces to:

$$I = 2I_0 + 2I_0\cos(\phi_1 - \phi_2) = 2I_0[1 + \cos(\phi_1 - \phi_2)] = 2I_0\cos^2\left(\frac{\phi_1 - \phi_2}{2}\right) \tag{2-5}$$

From (2-5), the maximum and minimum irradiance can be obtained when $\phi_1 - \phi_2 = 2m\pi$ where $m \in Z$, and $\phi_1 - \phi_2 = 2\left(m + \frac{1}{2}\right)\pi$.
On the other hand, another definition to be used later for determining fringe visibility is optical visibility, defined as:

$$V = \frac{I_{\max} - I_{\min}}{I_{\max} + I_{\min}} \tag{2-6}$$

where $I_{\max} = I_1 + I_2 + 2\sqrt{I_1 I_2}$ and $I_{\min} = I_1 + I_2 - 2\sqrt{I_1 I_2}$

2.2 Scalar Diffraction Theory

Light, in its most fundamental essence, is an electromagnetic wave. Its behavior is precisely governed by Maxwell's equations, a set of differential equations that describe the interconnection between electric and magnetic fields and their sources. [44] These equations reveal the vectorial nature of light, where polarization is a crucial property describing the spatially homogeneous or heterogeneous distribution of its field components. [38]

Although the complete vectorial description is rigorous, the exhaustive treatment of optical phenomena through Maxwell's equations can be extraordinarily complex for many practical problems. Addressing the behavior of all field components, especially when considering complex polarization interactions, often exceeds the needs of most applications and adds considerable computational burden. Therefore, to simplify the analysis and make wave optics more manageable under certain conditions, approximations are resorted to. [5]

This is where scalar diffraction theory comes into play. This theory represents a powerful simplification by considering light as a scalar wave, meaning it focuses on a single polarization component of the electric or magnetic field. The key assumption is that, under certain conditions, different polarization components can be treated independently. Fortunately, this approximation yields accurate and precise results as long as the involved diffraction angles are small or moderate. Although scalar theory intrinsically omits the effects of coupling between the various components of the electromagnetic field imposed by Maxwell's equations, its experimental validity has been demonstrated in a wide range of practical scenarios. [45]

By adopting a scalar approach, the theory focuses on the propagation of a complex scalar amplitude and its associated phase, allowing characterization of how a wave propagates from

an illuminated object to an observation plane. [44, 45] This simplified framework, while not encompassing all the nuances of the vectorial nature of light, is exceptionally effective for understanding and predicting a vast range of diffraction and interference phenomena.

2.2.1 Derivation of the Wave Equation

The scalar wave equation must be derived from the principles of Maxwell's equations, laying the foundations for understanding the propagation and diffraction of optical fields in the scalar regime.
Scalar diffraction theory provides a mathematical framework for analyzing the propagation of light waves when polarization effects can be neglected. This approximation is valid under two fundamental conditions:

1. **Size condition:** The characteristic dimension a of apertures or obstacles must be much larger than the illumination wavelength ($a \gg \lambda$).

2. **Distance condition:** The observation distance z must satisfy the *Fresnel criterion*:

$$z \gg \frac{a^2}{\lambda} \tag{2-7}$$

   This condition ensures that we are in the far-field region, where diffraction effects are fully developed.

Starting from Maxwell's equations in a source-free medium:

$$\nabla \times \vec{E} = -\mu \frac{\partial \vec{H}}{\partial t} \tag{2-8}$$

$$\nabla \times \vec{H} = \epsilon \frac{\partial \vec{E}}{\partial t} \tag{2-9}$$

$$\nabla \cdot \vec{E} = 0 \tag{2-10}$$

$$\nabla \cdot (\mu \vec{H}) = 0 \tag{2-11}$$

where $\vec{E}$ represents the electric field, $\vec{H}$ the magnetic field, μ and ϵ represent the magnetic permeability and electric permittivity in the medium in which the wave is propagating. [27] For a **linear, isotropic, homogeneous, non-dispersive, and non-magnetic** medium, applying the curl to equation (2-8):

$$\nabla \times (\nabla \times \vec{E}) = -\mu \frac{\partial}{\partial t} (\nabla \times \vec{H}) \tag{2-12}$$

Recalling the vector identity stating that $\nabla \times (\nabla \times \vec{E}) = \nabla(\nabla \cdot \vec{E}) - \nabla^2 \vec{E}$ and equation (2-9), then equation (2-12) takes the form:

$$\nabla(\nabla \cdot \vec{E}) - \nabla^2 \vec{E} = -\mu\epsilon \frac{\partial^2 \vec{E}}{\partial t^2}$$

Considering $\nabla \cdot \vec{E} = 0$ and defining $v = 1/\sqrt{\mu\epsilon}$:

$$\nabla^2 \vec{E} - \frac{1}{v^2} \frac{\partial^2 \vec{E}}{\partial t^2} = 0 \tag{2-13}$$

Each Cartesian component individually satisfies the scalar wave equation:

$$\nabla^2 U - \frac{n^2}{c^2} \frac{\partial^2 U}{\partial t^2} = 0, \quad \text{where } n = \sqrt{\frac{\mu\epsilon}{\mu_0 \epsilon_0}} \tag{2-14}$$

This separation justifies the scalar treatment when:

- Polarization effects are secondary.
- There is no significant coupling between components.
- Boundary conditions are primarily scalar.

For what follows, which is the derivation of the Rayleigh-Sommerfeld principle, it is necessary to recall Green's Theorem. Let $U(P)$ and $G(P)$ be complex functions with continuous single-valued first and second derivatives within a volume V enclosed by a surface S:

$$\int_V (U\nabla^2 G - G\nabla^2 U) dv = \iint_S (U\nabla \cdot G - G\nabla \cdot U) \cdot d\vec{S}$$

The physical interpretation indicates whether there are sources or sinks in a region.
The right-hand side of the equation can be written as a directional derivative. If $\frac{\partial f}{\partial \vec{v}} = \nabla_{\vec{v}} f = \nabla \cdot \vec{v}$ and $d\vec{S} = dS\hat{n}$, then the integral becomes:

$$\int_V (U\nabla^2 G - G\nabla^2 U) dV = \iint_S \left(U \frac{\partial G}{\partial n} - G \frac{\partial U}{\partial n} \right) dS \tag{2-15}$$

This last result is known as Green's theorem for diffraction.

2.2.2 Derivation of the Rayleigh-Sommerfeld Principle from Green's Theorem

Consider a monochromatic scalar field $U(\mathbf{r})$ satisfying the Helmholtz equation in the half-space $z > 0$: [44, 46]

$$(\nabla^2 + k^2)U = 0, \quad k = \frac{2\pi}{\lambda}, \tag{2-16}$$

where λ is the wavelength. Let A be an aperture in the plane $z = 0$ (opaque screen), and P an observation point at $z > 0$. The objective is to express $U(P)$ in terms of the values of U over A.

We apply Green's theorem to the functions $U(\mathbf{r})$ and $G_D(\mathbf{r}, \mathbf{r}')$ (Dirichlet Green's function) in the volume V defined by the half-space $z > 0$, excluding a small sphere of radius ϵ around P (to avoid the singularity). The function G_D satisfies:

$$(\nabla^2 + k^2)G_D = -4\pi\delta(\mathbf{r} - \mathbf{r}'), \tag{2-17}$$

and vanishes in the plane $z = 0$:

$$G_D(\mathbf{r}, \mathbf{r}') = \frac{e^{ik|\mathbf{r}-\mathbf{r}'|}}{|\mathbf{r} - \mathbf{r}'|} - \frac{e^{ik|\mathbf{r}-\mathbf{r}'^*|}}{|\mathbf{r} - \mathbf{r}'^*|}, \tag{2-18}$$

where $\mathbf{r}'^* = (x', y', -z')$ is the mirror image of $\mathbf{r}' = (x', y', z')$ with respect to the plane $z = 0$.

Green's theorem states:

$$\iiint_V \left(U\nabla^2 G_D - G_D\nabla^2 U\right) dV = \iint_S \left(U\frac{\partial G_D}{\partial n} - G_D\frac{\partial U}{\partial n}\right) dS, \tag{2-19}$$

where S is the surface enclosing V (plane $z = 0$ excluding A, plus a hemispherical surface at infinity S_∞, plus the surface of the small sphere S_ϵ), and $\partial/\partial n$ is the derivative in the direction of the outward normal.

Substituting the Helmholtz equations (2-16) and (2-17) into (2-19):

$$\iiint_V \left[U(-k^2 G_D - 4\pi\delta(\mathbf{r} - \mathbf{r}_P)) + G_D k^2 U\right] dV = \iint_S \left(U\frac{\partial G_D}{\partial n} - G_D\frac{\partial U}{\partial n}\right) dS, \tag{2-20}$$

which simplifies to:

$$-4\pi U(P) = \iint_S \left(U\frac{\partial G_D}{\partial n} - G_D\frac{\partial U}{\partial n}\right) dS, \tag{2-21}$$

where the volume integral includes the Dirac delta function property.

The surface S consists of three parts:

1. Plane $z = 0$ (includes screen P and aperture A), denoted S_1.
2. Hemispherical surface S_∞ at $|\mathbf{r}| \to \infty$, $z > 0$.
3. Spherical surface S_ϵ of radius ϵ around P.

The integral over S_∞ vanishes due to the Sommerfeld radiation condition ($R|\nabla U - ikU| \to 0$ as $R \to \infty$). On S_ϵ, we parametrize using spherical coordinates centered at P:

$$\iint_{S_\epsilon} \left(U\frac{\partial G_D}{\partial n} - G_D\frac{\partial U}{\partial n}\right) dS = \lim_{\epsilon\to 0} \iint_{S_\epsilon} \left[U\frac{\partial}{\partial r}\left(\frac{e^{ikr}}{r}\right) - \frac{e^{ikr}}{r}\frac{\partial U}{\partial r}\right] r^2 d\Omega, \tag{2-22}$$

where $d\Omega$ is the solid angle element. Expanding:

$$\frac{\partial}{\partial r}\left(\frac{e^{ikr}}{r}\right) = e^{ikr}\left(\frac{ik}{r} - \frac{1}{r^2}\right), \tag{2-23}$$

$$\iint_{S_\epsilon} U\frac{\partial G_D}{\partial r} r^2 d\Omega = \iint_{S_\epsilon} U e^{ik\epsilon}\left(ik\epsilon - 1\right) d\Omega \xrightarrow{\epsilon\to 0} -4\pi U(P), \tag{2-24}$$

$$\iint_{S_\epsilon} G_D\frac{\partial U}{\partial r} r^2 d\Omega = \iint_{S_\epsilon} \frac{e^{ik\epsilon}}{\epsilon}\frac{\partial U}{\partial r}\epsilon^2 d\Omega \xrightarrow{\epsilon\to 0} 0. \tag{2-25}$$

Thus, the integral over S_ϵ is $-4\pi U(P)$.
Substituting into (2-21):

$$-4\pi U(P) = \iint_{S_1}\left(U\frac{\partial G_D}{\partial n} - G_D\frac{\partial U}{\partial n}\right) dS - 4\pi U(P), \tag{2-26}$$

which implies:

$$0 = \iint_{S_1}\left(U\frac{\partial G_D}{\partial n} - G_D\frac{\partial U}{\partial n}\right) dS. \tag{2-27}$$

On S_1 ($z = 0$), $G_D = 0$ by construction. Furthermore, in the screen region (outside A), we assume $U = 0$ (opaque screen condition). Thus, (2-27) reduces to:

$$\iint_A U\frac{\partial G_D}{\partial n} dS = 0. \tag{2-28}$$

To include the singularity contribution, we consider the complete equation:

$$-4\pi U(P) = \underbrace{\iint_{S_1}\left(U\frac{\partial G_D}{\partial n} - G_D\frac{\partial U}{\partial n}\right) dS}_{0 \text{ (from 2-28)}} + \underbrace{\iint_{S_\epsilon} \cdots dS}_{-4\pi U(P)}, \tag{2-29}$$

leading to an inconsistency. The correction requires explicitly including S_ϵ from the beginning. Starting from (2-21) and using the results for S_ϵ and S_∞:

$$-4\pi U(P) = \iint_{S_1}\left(U\frac{\partial G_D}{\partial n} - G_D\frac{\partial U}{\partial n}\right) dS - 4\pi U(P), \tag{2-30}$$

adding $4\pi U(P)$ to both sides:

$$0 = \iint_{S_1}\left(U\frac{\partial G_D}{\partial n} - G_D\frac{\partial U}{\partial n}\right) dS. \tag{2-31}$$

With $G_D|_{S_1} = 0$ and $U = 0$ on the screen:

$$\iint_A U\frac{\partial G_D}{\partial n} dS = 0. \tag{2-32}$$

This indicates that the expression for $U(P)$ must be derived considering the homogeneous solution. The correct form is:

$$U(P) = -\frac{1}{4\pi}\iint_{S_1} U\frac{\partial G_D}{\partial n}dS, \tag{2-33}$$

valid when P is not on S_1. In A, U is the incident field, and on the screen $U = 0$, so:

$$U(P) = -\frac{1}{4\pi}\iint_{A} U(\mathbf{r}')\frac{\partial G_D}{\partial n}\bigg|_{\mathbf{r}'} dS'. \tag{2-34}$$

We compute $\partial G_D/\partial n$ at $z = 0$. The outward normal to V ($z > 0$) is $\hat{n} = -\hat{z}$, so $\partial/\partial n = -\partial/\partial z$. For $\mathbf{r}'$ at $z = 0$, with G_D defined as in (2-18):

$$G_D(\mathbf{r}, \mathbf{r}') = \frac{e^{ikR_1}}{R_1} - \frac{e^{ikR_2}}{R_2}, \tag{2-35}$$

$$R_1 = \sqrt{(x - x')^2 + (y - y')^2 + (z - z')^2}, \tag{2-36}$$

$$R_2 = \sqrt{(x - x')^2 + (y - y')^2 + (z + z')^2}. \tag{2-37}$$

At $z' = 0$, $R_1 = R_2 = R = \sqrt{(x - x')^2 + (y - y')^2 + z^2}$. The normal derivative is:

$$\frac{\partial G_D}{\partial n} = -\frac{\partial G_D}{\partial z'}\bigg|_{z'=0} = -\left[\frac{\partial}{\partial z'}\left(\frac{e^{ikR_1}}{R_1}\right) - \frac{\partial}{\partial z'}\left(\frac{e^{ikR_2}}{R_2}\right)\right]_{z'=0}. \tag{2-38}$$

Each term:

$$\frac{\partial}{\partial z'}\left(\frac{e^{ikR}}{R}\right) = e^{ikR}\left(ik - \frac{1}{R}\right)\frac{1}{R}\frac{\partial R}{\partial z'}. \tag{2-39}$$

For R_1: $\partial R_1/\partial z' = -(z - z')/R_1$, at $z' = 0$: $\partial R_1/\partial z' = -z/R$. For R_2: $\partial R_2/\partial z' = (z + z')/R_2$, at $z' = 0$: $\partial R_2/\partial z' = z/R$. Substituting:

$$\frac{\partial G_D}{\partial n} = -\left[e^{ikR}\left(ik - \frac{1}{R}\right)\frac{1}{R}\left(-\frac{z}{R}\right) - e^{ikR}\left(ik - \frac{1}{R}\right)\frac{1}{R}\left(\frac{z}{R}\right)\right] \tag{2-40}$$

$$= \frac{2z}{R}e^{ikR}\left(ik - \frac{1}{R}\right)\frac{1}{R} = 2\frac{\partial}{\partial z}\left(\frac{e^{ikR}}{R}\right). \tag{2-41}$$

Substituting into (2-34):

$$U(P) = -\frac{1}{4\pi}\iint_{A} U(\mathbf{r}')\cdot 2\frac{\partial}{\partial z}\left(\frac{e^{ikR}}{R}\right)dS' = -\frac{1}{2\pi}\iint_{A} U(\mathbf{r}')\frac{\partial}{\partial z}\left(\frac{e^{ikR}}{R}\right)dS'. \tag{2-42}$$

Expanding the derivative:

$$\frac{\partial}{\partial z}\left(\frac{e^{ikR}}{R}\right) = e^{ikR}\left(ik - \frac{1}{R}\right)\frac{z}{R^2}, \tag{2-43}$$

and noting that $z/R = \cos\theta$ (where θ is the angle between vector $\mathbf{R} = \mathbf{r} - \mathbf{r}'$ and the normal $\hat{z}$), we obtain the **first Rayleigh-Sommerfeld formula**:

$$U(P) = -\frac{1}{2\pi}\iint_A U(\mathbf{r}')e^{ikR}\left(ik - \frac{1}{R}\right)\frac{\cos\theta}{R}dS'. \tag{2-44}$$

In the far-field approximation ($R \gg \lambda$), the $1/R$ term is negligible compared to $k = 2\pi/\lambda$, resulting in the standard form:

$$U(P) = \frac{1}{i\lambda}\iint_A U(\mathbf{r}')\frac{e^{ikR}}{R}\cos\theta dS', \tag{2-45}$$

which is the Rayleigh-Sommerfeld diffraction principle.

2.2.3 Angular Spectrum Approximation

The angular spectrum formulation provides an exact method for optical field propagation through plane wave decomposition. We start from the Rayleigh-Sommerfeld expression in Fourier space: [27, 47]

$$U(x, y, z) = \frac{1}{(2\pi)^2}\iint_{-\infty}^{\infty}\tilde{U}(k_x, k_y; 0)\, e^{i(k_x x + k_y y + k_z z)}dk_x dk_y, \tag{2-46}$$

where $\tilde{U}(k_x, k_y; 0)$ is the Fourier transform of the field at plane $z = 0$:

$$\tilde{U}(k_x, k_y; 0) = \iint_{-\infty}^{\infty}U(x', y', 0)\, e^{-i(k_x x' + k_y y')}dx'dy', \tag{2-47}$$

and k_z is given by the dispersion relation:

$$k_z = \begin{cases}\sqrt{k^2 - k_x^2 - k_y^2} & \text{for } k_x^2 + k_y^2 \leq k^2 \\ i\sqrt{k_x^2 + k_y^2 - k^2} & \text{for } k_x^2 + k_y^2 > k^2\end{cases} \tag{2-48}$$

The physical interpretation is:

- When $k_x^2 + k_y^2 \leq k^2$, k_z is real and corresponds to propagating waves.
- When $k_x^2 + k_y^2 > k^2$, k_z is imaginary and represents evanescent waves.

The propagation algorithm consists of:

1. Compute the Fourier transform of the initial field: $\tilde{U}(k_x, k_y; 0)$
2. Multiply by the propagator: $H(k_x, k_y; z) = e^{ik_z z}$

3. Compute the inverse Fourier transform

Mathematically:

$$U(x, y, z) = \mathcal{F}^{-1}\left\{\mathcal{F}\{U(x, y, 0)\} \cdot e^{ik_z z}\right\} \tag{2-49}$$

This formulation is *exact* and valid for any distance $z > 0$, including the near-field region where evanescent components dominate.

2.2.4 Fresnel Approximation

The Fresnel approximation, valid in the paraxial region ($z \gg \lambda$ and small angles), is obtained through binomial expansion of R in the Rayleigh-Sommerfeld integral:[47, 27]

$$R = \sqrt{(x - x')^2 + (y - y')^2 + z^2} = z\sqrt{1 + \frac{(x - x')^2}{z^2} + \frac{(y - y')^2}{z^2}} \tag{2-50}$$

Taylor series expansion:

$$R \approx z\left[1 + \frac{(x - x')^2}{2z^2} + \frac{(y - y')^2}{2z^2} - \frac{[(x - x')^2 + (y - y')^2]^2}{8z^4} + \cdots\right] \tag{2-51}$$

In the Fresnel approximation we retain only quadratic terms:

$$R \approx z + \frac{(x - x')^2 + (y - y')^2}{2z} \tag{2-52}$$

Substituting into the Rayleigh-Sommerfeld expression:

$$U(x, y, z) = \frac{1}{i\lambda}\iint_{-\infty}^{\infty} U(x', y', 0)\,\frac{e^{ikR}}{R}\cos\theta\,dx'dy' \tag{2-53}$$

$$\approx \frac{1}{i\lambda z}\iint_{-\infty}^{\infty} U(x', y', 0)\,e^{ik\left[z + \frac{(x-x')^2 + (y-y')^2}{2z}\right]}\,dx'dy' \tag{2-54}$$

Simplifying yields the **Fresnel diffraction formula**:

$$U(x, y, z) = \frac{e^{ikz}}{i\lambda z}e^{i\frac{k}{2z}(x^2+y^2)}\iint_{-\infty}^{\infty} U(x', y', 0)e^{i\frac{k}{2z}(x'^2+y'^2)}e^{-i\frac{2\pi}{\lambda z}(xx'+yy')}dx'dy' \tag{2-55}$$

Recognizing the Fourier transform form:

$$U(x, y, z) = \frac{e^{ikz}}{i\lambda z}e^{i\frac{k}{2z}(x^2+y^2)} \cdot \mathcal{F}\left\{U(x', y', 0)e^{i\frac{k}{2z}(x'^2+y'^2)}\right\}_{f_x=\frac{x}{\lambda z}, f_y=\frac{y}{\lambda z}} \tag{2-56}$$

The approximation is valid when the **Fresnel criterion** is satisfied:

$$z^3 \gg \frac{\pi}{4\lambda}\left[(x - x')^2 + (y - y')^2\right]^2_{\max} \tag{2-57}$$

The Fresnel formula can be interpreted as:

- A Fourier transform of the field multiplied by a quadratic phase factor
- A convolution with the Fresnel kernel: $h(x,y) = \frac{e^{ikz}}{i\lambda z} e^{i\frac{k}{2z}(x^2+y^2)}$
- An approximation that preserves diffraction characteristics while significantly simplifying calculations

2.3 Coherence Theory

The theory of optical coherence is a fundamental field of optics focused on studying the statistical properties of light and their influence on the observable characteristics of optical fields. [48] Specifically, this theory describes the *statistical similarity* correlation of light fields at different points in space and/or instants in time. [49]

Historically, the modern concept of coherence dates to the late 19th and early 20th centuries, with key figures including Verdet, Von Laue, Berek, van Cittert, and Zernike. [45] However, Emil Wolf emerged as the dominant figure in optical coherence theory from the mid-20th century onward, making significant contributions to its formulation in the space-frequency domain. [48] Classical experiments such as Young's demonstration of spatial interference and the Michelson interferometer for temporal interference were crucial to its initial development. [45] A fundamental milestone is the van Cittert-Zernike theorem, which demonstrates how a spatially incoherent source can generate a partially coherent field upon light propagation. This theorem has been generalized to electromagnetic fields, where the degree of coherence increases with propagation while the degree of polarization remains unchanged. [50]

Coherence is primarily divided into two aspects: temporal coherence and spatial coherence. [45, 5] Temporal coherence describes the correlation between fields emitted at different time instants. Spatial coherence, conversely, describes the correlation between fields at distinct spatial positions. These concepts are generalized through the mutual coherence function (MCF) and its Fourier transform, the cross-spectral density (CSD). [51] The CSD is fundamental for describing optical fields in the space-frequency domain, extending coherence theory to this domain. [52] For electromagnetic fields, the concept is expanded through the beam coherence-polarization matrix (BCPM) and the cross-spectral density matrix (CSDM). [53] The degree of coherence (DOC), or complex spectral degree of coherence (SDOC), is a normalized function quantifying correlation and is directly related to fringe visibility in interference patterns.

Various approaches model and study partially coherent light. Schell-model (SM) sources are widely used, characterized by Gaussian spectral density and spectral degree of coherence. [54] Quasi-homogeneous sources serve as excellent models for many physical thermal

sources (e.g., stars) and are globally nearly spatially incoherent. [48] Pseudo-Schell model (PSM) sources exhibit radial symmetry, where all points on concentric circles are perfectly correlated, and can generate beams with sharper profiles and higher peak values. [55] Coherent mode decomposition allows representing a partially coherent field as an incoherent superposition of individual coherent modes, facilitating analysis and propagation. [51] Alternatively, pseudo-modes provide a flexible approach for generating partially coherent sources. [53]

Propagation of partially coherent light through media and optical systems can be addressed by solving Helmholtz equations for the correlation function or using the Wigner function in phase space. [56] The extended Huygens-Fresnel principle is also employed for propagation in random media. [48] Furthermore, partially coherent beams exhibit reduced sensitivity to atmospheric turbulence effects compared to coherent beams, making them promising for free-space optical communications. [57, 58]

Understanding optical coherence is vital for numerous practical applications. Partially coherent light is extensively used in microscopy, [59] lithography, and optical communications. [57] In lensless digital in-line holographic microscopy (DIHM)—which overcomes lens limitations through numerical image reconstruction—partially coherent light reduces speckle noise and enhances the signal-to-noise ratio. [9] This technique is compact, cost-effective, and has been used for 3D tracking of cells and microorganisms, as well as telemedicine applications. [56] Multi-height and multi-spectral phase retrieval methods have been developed to improve image quality in lensless microscopy. [7] Other notable applications include optical coherence tomography (OCT), optical particle manipulation, and remote sensing. [5] Holography, particularly digital holography, relies on adequate coherence for wavefront recording and reconstruction, with algorithms developed for twin-image removal in in-line holography. [32]

This chapter will explore these fundamentals of optical coherence theory, focusing specifically on definitions related to the spatial coherence theory of electromagnetic waves.

2.3.1 Mathematical Foundations of Optical Coherence

Mutual Coherence Function

The mutual coherence function $\Gamma(P_1, P_2, \tau)$ characterizes the spatiotemporal correlations between two points P_1 and P_2 on the wavefront Σ_1 as depicted in Fig. **2-1**

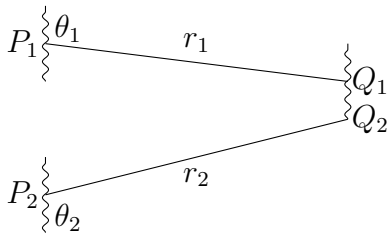

Figure 2-1: Geometry for propagation of mutual coherence, where θ_1 and θ_2 represent the angle between the lines r_1 and r_2 respectively and a normal line to the surface where are the points P_1 and P_2 Σ_1 and Σ_2.

Consider two wave-fronts where Σ_1 is fully characterized. The objective is to propagate each point from Σ_1 to Σ_2. Applying the narrow-band condition, i.e., the illumination source has a narrow spectral width. The statistical description of partially coherent optical fields is based on the *mutual coherence function* (MCF), defined as the second-order cross-correlation between two field points:

$$\Gamma(Q_1, Q_2, \tau') = \langle u(Q_1, t + \tau') \times u^*(Q_2, t) \rangle \tag{2-58}$$

where $u(\mathbf{r}, t)$ is the complex optical disturbance, $\langle \cdot \rangle_T$ denotes time average, and τ is the time delay. [45] This function unifies the concepts of temporal and spatial coherence.
To propagate this coherence to Σ_2, we start from the disturbances at Q_1 and Q_2:

$$u(Q_1, t + \tau') = \iint_{\Sigma_1} \frac{1}{j\lambda r_1} u\left(P_1, t + \tau' - \frac{r_1}{c}\right) \chi(\theta_1) dS_1 \tag{2-59}$$

$$u(Q_2, t) = \iint_{\Sigma_1} \frac{1}{j\lambda r_2} u\left(P_2, t - \frac{r_2}{c}\right) \chi(\theta_2) dS_2 \tag{2-60}$$

Where $\chi(\theta_1)$ and $\chi(\theta_2)$ are the obliquity factors for each disturbance. Substituting into $\Gamma(Q_1, Q_2; \tau') = \langle u(Q_1, t + \tau') u^*(Q_2, t) \rangle$ and using the Γ definition for P_1 and P_2:

$$\Gamma(Q_1, Q_2; \tau') = \iint_{\Sigma_1} \iint_{\Sigma_1} \frac{\langle u(P_1, t + \tau' - \frac{r_1}{c}) u^*(P_2, t - \frac{r_2}{c}) \rangle}{\bar{\lambda}^2 r_1 r_2} \chi(\theta_1)\chi(\theta_2) dS_1 dS_2 \tag{2-61}$$

$$\Gamma(Q_1, Q_2; \tau') = \iint_{\Sigma_1} \iint_{\Sigma_1} \Gamma\left(P_1, P_2; \tau' + \frac{r_2 - r_1}{c}\right) \frac{\chi(\theta_1)}{\bar{\lambda} r_1} \frac{\chi(\theta_2)}{\bar{\lambda} r_2} dS_1 dS_2. \tag{2-62}$$

For quasi-monochromatic light ($\Delta\nu \ll \bar{\nu}$), the mutual intensity $J(Q_1, Q_2) = \Gamma(Q_1, Q_2; 0)$ is:

$$J(Q_1, Q_2) = \iint_{\Sigma_1} \iint_{\Sigma_1} J(P_1, P_2) e^{-j\frac{2\pi}{\lambda}(r_2 - r_1)} \frac{\chi(\theta_1)}{\bar{\lambda} r_1} \frac{\chi(\theta_2)}{\bar{\lambda} r_2} dS_1 dS_2. \tag{2-63}$$

Note that both coherence and mutual intensity functions exhibit forms similar to the Fresnel diffraction integral, while also satisfying wave propagation properties. Furthermore, to determine the intensity distribution at a point Q, it is obtained when $Q_1 \to Q_2$:

$$I(Q) = \iint_{\Sigma_1} \iint_{\Sigma_1} J(P_1, P_2) e^{-j\frac{2\pi}{\lambda}(r_2' - r_1')} \frac{\chi(\theta_1')}{\bar{\lambda} r_1'} \frac{\chi(\theta_2')}{\bar{\lambda} r_2'} dS_1 dS_2, \tag{2-64}$$

where r_1' and r_2' are the distances from P_1 and P_2 to Q.

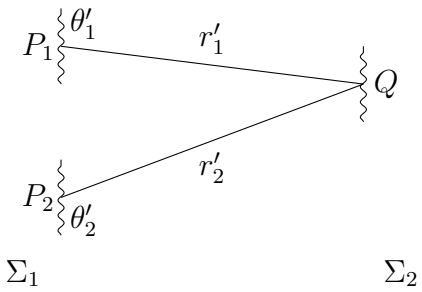

Figure 2-2: Propagation geometry from surfaces Σ_1 to Σ_2 from points P_1, P_2 to point Q.

Coherent, Incoherent, and Partially Coherent Fields

The statistical description of a random optical wave relies on information about its correlation (average similarity) with its own versions and other (reference) waves taken at various sets of positions and/or times, [45] a process known as amplitude division. In practice, no light source is perfectly monochromatic; all contain a range of frequencies. [60] An interferogram, for example, is a photographic record of intensity as a function of optical path difference between two interfering waves.

Various instruments exist to measure temporal coherence, the most relevant (due to its historical importance) being the Michelson interferometer. Near zero path difference, elementary fringes add in phase, producing high fringe visibility. [45] As the delay increases, phase changes lead to partially destructive addition and decreased fringe visibility. The loss of fringe visibility can be understood as decorrelation. The complex degree of coherence ($\gamma(\tau)$) mathematically describes the interference, its modulus $|\gamma(\tau)|$ being related to the fringe visibility ν defined in equation (2-6), a concept introduced by Michelson.

Spatial coherence, on the other hand, refers to the ability of a light beam to interfere with itself after a spatial displacement (without temporal delay). This process is known as wavefront division. [45] Young's classic double-slit experiment is fundamental for demonstrating and studying spatial coherence. In this experiment, light from two pinholes (P_1 and P_2) interferes to form fringes on a screen, and its corresponding complex degree of mutual coherence

$\gamma(P_1, P_2)$ describes the correlation between two spatial points P_1 and P_2.

An optical field is fully coherent (in the spatial context) when the waveforms at two points P_1 and P_2 are perfectly correlated for all delays τ. If its complex degree of coherence satisfies:

$$|\gamma(P_1, P_2, \tau)| = 1 \quad \forall P_1, P_2 \text{ and } \forall \tau \tag{2-65}$$

where γ is defined as: [27]

$$\gamma(P_1, P_2, \tau) = \frac{\Gamma(P_1, P_2, \tau)}{\sqrt{I(P_1)I(P_2)}}, \quad \Gamma(P_1, P_2, \tau) = \langle U(P_1, t+\tau)U^*(P_2, t)\rangle \tag{2-66}$$

However, this definition is restrictive and applies perfectly only to ideal monochromatic waves. [45, 48]

Conversely, a field is incoherent if:

$$|\gamma(P_1, P_2; \tau)| = 0 \quad \text{for} \quad P_1 \neq P_2, \text{ and } \forall \tau \tag{2-67}$$

This means there is no correlation between any two distinct points P_1 and P_2. In practice, this definition is of limited utility, as it would imply vanishing intensity after integration.

Finally, a field is partially coherent when $0 < |\gamma(\tau)| < 1$. Such fields exhibit random fluctuations in space and time, and the coherence functions describing them may contain phase singularities, and as mentioned before, the spatial degree of coherence can be determined through the visibility ν (2-6). [5]

Coherence is a crucial property of light beams that can be used to reduce turbulence-induced degradation in optical communications, enhance information encryption, and achieve robust far-field imaging. [38]

2.3.2 Gaussian Schell-Model

Gaussian Schell-model (GSM) fields constitute a fundamental framework in statistical optics for describing partially coherent light fields. Their significance stems from mathematical tractability and analytical convenience, making them particularly valuable in coherence theory. [5]
A Schell-model field is defined by having a complex spectral degree of coherence (or spectral mutual coherence function) that depends exclusively on the difference between spatial coordinates of observation points. This implies translational invariance in coherence properties, expressed as:

$$\mu(\vec{r}_1, \vec{r}_2, \omega) = \mu(\vec{r}_2 - \vec{r}_1, \omega) \tag{2-68}$$

where μ denotes the complex degree of coherence and ω the angular frequency. This model was initially proposed by A.C. Schell. [45, 48, 5] GSM fields represent a special case where both the spectral intensity $I(\vec{r})$ and spectral degree of coherence $\mu(\Delta\vec{r})$ exhibit Gaussian distributions in the source plane. [5]
The mutual intensity function $J(\vec{r}_1, \vec{r}_2)$ (corresponding to mutual coherence at $\tau = 0$) for a GSM field is defined as:

$$J(\vec{r}_1, \vec{r}_2) = \sqrt{I(\vec{r}_1)I(\vec{r}_2)}\mu(\vec{r}_2 - \vec{r}_1) \tag{2-69}$$

Equivalently, when expressed in center-difference coordinates ($\bar{\xi} = \frac{\xi_1+\xi_2}{2}$, $\bar{\eta} = \frac{\eta_1+\eta_2}{2}$) and coordinate differences ($\Delta\xi = \xi_2 - \xi_1$, $\Delta\eta = \eta_2 - \eta_1$):

$$J(\bar{\xi}, \bar{\eta}, \Delta\xi, \Delta\eta) = A\left(\bar{\xi} - \tfrac{\Delta\xi}{2}, \bar{\eta} - \tfrac{\Delta\eta}{2}\right) A\left(\bar{\xi} + \tfrac{\Delta\xi}{2}, \bar{\eta} + \tfrac{\Delta\eta}{2}\right) \mu(\Delta\xi, \Delta\eta) \tag{2-70}$$

where $A(\vec{r}) = \sqrt{I(\vec{r})}$ is the field amplitude.
This coordinate transformation is not merely mathematical: it reveals fundamental physical properties about the spatial structure of coherence. As established by Goodman [45], the transition to center-difference coordinates $(\bar{\xi}, \bar{\eta}, \Delta\xi, \Delta\eta)$ allows expressing the mutual intensity as:

$$J(\bar{\vec{r}}, \Delta\vec{r}) = A\left(\bar{\vec{r}} - \tfrac{\Delta\vec{r}}{2}\right) A\left(\bar{\vec{r}} + \tfrac{\Delta\vec{r}}{2}\right) \mu(\Delta\vec{r}) \tag{2-71}$$

where $\bar{\vec{r}} = (\bar{\xi}, \bar{\eta})$ is the coherence center position and $\Delta\vec{r} = (\Delta\xi, \Delta\eta)$ is the spatial separation vector. This formulation highlights two key physical aspects: First, the separability of spatial coherence. The function $\mu(\Delta\vec{r})$ depends exclusively on the spatial separation $\Delta\vec{r}$, reflecting that coherence is a statistical property intrinsic to point pairs, independent of their absolute location in the source plane. This is the defining characteristic of Schell-model fields. [45]

Second is the geometric coupling of intensities; the term $A(\bar{\vec{r}} - \frac{\Delta\vec{r}}{2})A(\bar{\vec{r}} + \frac{\Delta\vec{r}}{2})$ describes how optical intensity modulates coherence as a function of central position $\bar{\vec{r}}$. For Gaussian profiles, this product simplifies remarkably:

$$A\left(\bar{\xi} \mp \tfrac{\Delta\xi}{2}, \bar{\eta} \mp \tfrac{\Delta\eta}{2}\right) = \sqrt{I_0} \exp\left[-\frac{(\bar{\xi} \mp \frac{\Delta\xi}{2})^2 + (\bar{\eta} \mp \frac{\Delta\eta}{2})^2}{4\sigma_s^2}\right] \tag{2-72}$$

Third, translational symmetry: when $\mu(\Delta\vec{r})$ depends solely on $\Delta\vec{r}$ (as in GSM), the field exhibits wide-sense stationarity [45], implying invariance under translations of the point pair. This property enables complete factorization:

$$J(\bar{\vec{r}}, \Delta\vec{r}) = \underbrace{\sqrt{I_0} \exp\left(-\frac{\bar{\xi}^2 + \bar{\eta}^2}{2\sigma_s^2}\right) \exp\left(-\frac{(\Delta\xi)^2 + (\Delta\eta)^2}{8\sigma_s^2}\right)}_{\text{Intensity term}} \cdot \underbrace{\exp\left(-\frac{(\Delta\xi)^2 + (\Delta\eta)^2}{2\sigma_\mu^2}\right)}_{\text{Coherence term}} \tag{2-73}$$

Equation (2-73) explicitly shows the separation between intensity contributions (dependent on $\vec{\bar{r}}$) and coherence contributions (dependent on $\Delta\vec{r}$), an essential characteristic that facilitates propagation analysis through optical systems using linear operators. [45]
For a Gaussian Schell-model source, the spatial profiles are:

$$I(\xi,\eta) = I_0 \exp\left(-\frac{\xi^2+\eta^2}{2\sigma_s^2}\right) = I_0 \exp\left(-\frac{\rho^2}{2\sigma_s^2}\right) \tag{2-74}$$

$$\mu(\Delta\xi,\Delta\eta) = \exp\left(-\frac{\Delta\xi^2+\Delta\eta^2}{2\sigma_\mu^2}\right) = \exp\left(-\frac{\rho'^2}{2\sigma_\mu^2}\right) \tag{2-75}$$

with $\rho = \sqrt{\xi^2+\eta^2}$ and $\rho' = \sqrt{\Delta\xi^2+\Delta\eta^2}$. Here, σ_s denotes the spatial intensity width and σ_μ the transverse correlation length. The relationship between these parameters determines the coherence state:

- $\sigma_\mu \gg \sigma_s$: Coherent field ($\mu \approx 1$)
- $\sigma_\mu \ll \sigma_s$: Incoherent field ($\mu \approx \delta(\Delta\vec{r})$)
- $\sigma_\mu \sim \sigma_s$: Partially coherent field

The GSM framework has been extended to vector electromagnetic fields and underlies generalized Schell-model sources where μ depends on coordinate difference powers. This enables exotic propagation effects like self-shifting and self-focusing, with applications in optical particle manipulation and materials processing. [61] It also plays a fundamental role in light scattering studies. [62]
These models serve as powerful analytical tools for investigating how interference visibility (directly linked to $|\mu|$) governs intensity redistribution during propagation. In Young's experiments with GSM sources, fringe visibility depends solely on aperture separation ($\Delta\vec{r}$) and remains position-independent—a direct consequence of coherence translational invariance.

2.4 Auto-focus Metrics

Auto-focus metrics are essential tools for determining the plane of best focus in optical and imaging systems, particularly in digital microscopy and holography contexts. They enable the calculation of the axial position (distance z) where the image or pattern of interest exhibits maximum sharpness or quality. Below, we explore the theoretical foundations, application, use cases, and advantages/disadvantages of intensity variance, total gradient, information entropy, and local contrast metrics, based on the provided information.

2.4.1 Intensity Variance

Intensity variance is a statistical measure quantifying intensity fluctuations in an image [45, 51]. In thermal or pseudo-thermal light contexts, it directly relates to integrated intensity variance and light fluctuation contrast. A related term is the scintillation index, defined as the normalized variance of fluctuating intensity [48]. For electromagnetic fields, intensity fluctuation contrast ($c_I(r)$) is expressed as $Tr[\Gamma(r,r;0)^2]/Tr[\Gamma(r,r;0)]^2$. [51]

In autofocus, intensity variance identifies the axial plane where intensity fluctuations are maximized. A focused image contains sharper details (edges and textures), resulting in higher intensity variance compared to a defocused image, which appears blurred with lower variance. The variance is calculated for multiple images at different z-planes, selecting the plane maximizing this value.

This metric applies to analyzing statistical properties of light, especially when fluctuations follow non-Gaussian statistics, or in electromagnetic theory where contrast values depend on beam polarization properties beyond coherence. [51] It is relevant for systems handling stochastic light (e.g., thermal or pseudo-thermal sources). [45, 53]

Advantages include direct measurement of image sharpness and detail since well-focused images exhibit greater intensity variations. The ability to control intensity fluctuations is key in light beam characterization. [63] Disadvantages include noise sensitivity, as noise introduces intensity fluctuations that may cause incorrect focusing if unmanaged.

Variance quantifies intensity dispersion relative to its mean, defined as:

$$\sigma^2(z) = \frac{1}{N_x N_y} \sum_{x=1}^{N_x} \sum_{y=1}^{N_y} [I(x,y;z) - \mu(z)]^2 \tag{2-76}$$

where:

- $I(x,y;z)$: Reconstructed intensity at position (x,y) at distance z
- $\mu(z) = \frac{1}{N_x N_y} \sum_{x,y} I(x,y;z)$: Mean intensity value
- N_x, N_y: Spatial dimensions of the hologram

This metric peaks at the best-focus plane due to maximal intensity dispersion.

2.4.2 Total Gradient Metric (Sum-of-Gradients)

Known as *Sum-of-gradients based Focus Measure*, it sums gradient magnitudes of intensity in an image. [9] Gradients measure pixel intensity change rates, peaking at edges and fine

features. Total Variation (TV), while not a direct autofocus metric, is a related concept used as a regularizer in image denoising and de-blurring, based on image gradient sums. [64, 65] It quantifies spatial sharpness via the gradient operator:

$$G_r(m,n) = \sqrt{(\partial_x G(m,n))^2 + (\partial_y G(m,n))^2} \tag{2-77}$$

where $G_x(m,n)$ is the gradient of $G(m,n)$ along the x direction, and $G_y(m,n)$ is the gradient of $G(m,n)$ along the y direction. [9]

Auto-focus with this metric calculates gradient magnitude sums across z-planes. The best-focus plane maximizes this sum, indicating the sharpest edges and most detail. Its use has been investigated in lensless microscopy with partially coherent illumination. [9] Gradient-based variants (e.g., *Gini-index-of-gradients*, *Tamura-coefficients-of-gradients*) effectively identify focus points, showing clear peaks in auto-focus curves.
These metrics are robust for focus determination since focused images maximize edge information. Their predictable peak behavior favors computational automation. However, noise can influence gradient values, and performance varies with illumination type and sample [9]. Some metrics may generate multiple peaks/valleys, complicating automated focus detection when seeking absolute maxima/minima.

2.4.3 Information Entropy Metric

While not conventionally described as an auto-focus metric, entropy is referenced as *eigenvalue entropy for measuring partial coherence*. [56] Here, lower entropy implies higher coherence in the light field. Entropy measures randomness or disorder in a probability distribution; applied to images, a focused image may have a more ordered intensity distribution than a defocused one.

Typically for auto-focus, a focused image would exhibit minimum entropy (or maximum, depending on the specific sharpness definition). However, sources focus on its use for coherence measurement, not direct image sharpness. We used the definition adapted for 8-bit digital images:[66]

$$H(z) = -\sum_{k=0}^{255} p_k(z) \log_2[p_k(z) + \epsilon] \tag{2-78}$$

where $p_k(z)$ is the probability of intensity level k (estimated as normalized histogram count), and $\epsilon = 2.22 \times 10^{-16}$ prevents logarithmic singularities. The upper limit of summation ($k = 255$) explicitly constrains this metric to 8-bit imagery, as:

1. Digital 8-bit sensors encode intensity values in the range $[0, 255]$ ($2^8 = 256$ discrete levels)

2. The probability mass function $p_k(z)$ is derived from the image histogram with exactly 256 bits

3. This quantization matches the discrete formulation of Shannon entropy for digital systems

This formulation primarily characterizes light coherence properties through intensity distribution. While its direct application as an auto-focus metric for determining the optimal image plane is not extensively documented in the literature, it was selected for comparative evaluation with other metrics to assess auto-focus efficiency in 8-bit imaging systems.

An advantage is its potential to measure information order/structure in images, theoretically correlating with focus. However, its direct relationship with image sharpness for auto-focus is less clear than conventional metrics.

2.4.4 Local Contrast Metric

Local contrast is intrinsically related to interference fringe visibility. [45] In Young's experiment, fringe visibility measures the spatial coherence degree. [51] Intensity interferometers (e.g., Hanbury Brown-Twiss) extract modulus information of the complex coherence factor. [48, 53] The term *Concentration-Based Focus Measure* [9] is relevant since higher intensity concentration at the focus implies greater contrast/sharpness.

For auto-focus, this metric identifies the axial plane maximizing image contrast. A contrast metric (based on max-min intensity differences or energy concentration) is computed at each z-plane, selecting the z with the highest value. It evaluates spatial variations via local standard deviation:

$$C = \frac{1}{N_w} \sum_{m=1}^{N_w} \frac{\sigma_m}{\mu_m + \epsilon} \tag{2-79}$$

calculated in 9×9 pixel windows, with $\epsilon = 10^{-6}$ for numerical stability.
It is fundamental in optical coherence experiments (e.g., interferometry) for characterizing light sources and coherence. [45] In microscopy, interference fringe contrast is crucial for spatial resolution, [8] implying good resolution (and focus) associates with high contrast. Intensity concentration metrics have been tested in lensless microscopy with LED/laser illumination. [9] Advantages include intuitiveness and effectiveness since focused images naturally exhibit higher contrast. Theoretical support comes from fringe visibility in interferometry. [51]

Disadvantages include susceptibility to noise and image quality (SNR), reducing observable resolution/contrast. [67] Self-image contrast decreases with illumination coherence length, affecting focus range in some systems. [54]

2.5 Resolution Criteria

For lateral calibration of an optical system, the U.S.A.F. 1951 test target is typically employed. This target comprises groups of horizontal and vertical line patterns with standardized dimensions and spacings that progressively decrease in size. Here, lateral resolution refers specifically to the minimum spatial separation between distinguishable features in the transverse plane. To determine this parameter, the reconstructed image is inspected to identify the smallest resolvable element (specified by group and element number) where individual lines remain clearly distinguishable under standard resolution criteria. [14, 68]

Resolution is conventionally expressed in line pairs per millimeter (lp/mm) or equivalently as the corresponding line width in micrometers. As shown in Fig. **2-3**, the USAF 1951 target follows a standardized structure organized into *groups* and *elements*:

- The target contains 7 distinct groups (typically numbered from -2 to 7 or 1 to 7 depending on configuration)
- Each group consists of 6 elements (numbered 1 to 6)
- Resolution increases progressively: Group n has higher resolution than Group $n-1$
- Within each group, element m has higher resolution than element $m-1$

The resolution value for any element is calculated as:

$$\text{Resolution}\,(\text{lp/mm}) = 2^{\left(\text{Group}+\frac{\text{Element}-1}{6}\right)} \tag{2-80}$$

This logarithmic scaling explains the division by 6 in the exponent: each group spans one octave (factor of 2 in resolution), while the 6 elements provide equally spaced logarithmic steps within each octave. For instance, element 1 of group 7 corresponds to:

$$2^{\left(7+\frac{1-1}{6}\right)} = 2^7 = 128\text{lp/mm}$$

equivalent to a line width of 3.91μm (calculated as $\frac{1000\mu\text{m/mm}}{2\times128} = 3.91\mu$m per line + space pair).

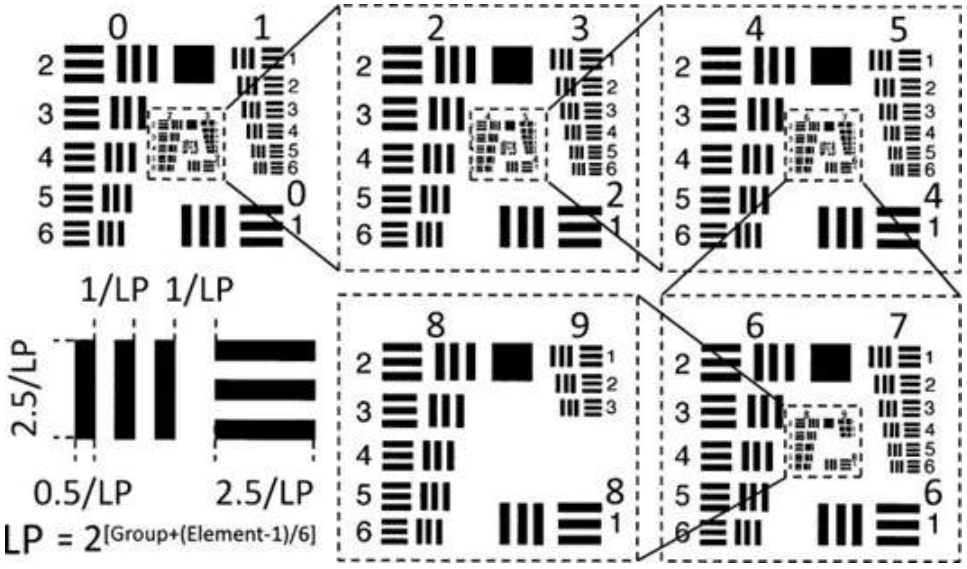

Figure 2-3: Graphical representation of a U.S.A.F. 1951 calibration target.

The resolution limit of an experimental setup depends on various factors, such as numerical aperture, wavelength, pixel size, and the reconstruction algorithms employed (depending on near-field or far-field regimes); however, for this particular case, the aim is to determine how variations in the spatial coherence of the illumination source impact the resolution of reconstructed objects.

The *10%-90% criterion* is a practical methodology used to quantify resolution or edge sharpness in reconstructed images of microscopy systems, particularly in lensless microscopy. This criterion is applied to intensity profiles (lineouts) taken across reconstructed patterns, such as the lines of a USAF 1951 test target. It involves measuring the distance (in pixels) over which the intensity transition at an edge spans from 10% to 90% of its maximum value (or minimum value in the case of a dark line). This measurement reflects the edge *slope* in the digital image.[20]

This distance can be converted to micrometers by multiplying the number of pixels by the sensor pixel size and the system magnification factor. The resolution (R) is calculated as: $R = n_{(10\%-90\%)} \times \Delta_{pixel}$ where $n_{10\%-90\%}$ denotes the number of pixels comprising the rising (or falling) edge between 10% and 90% intensity levels, and Δ_{pixel} is the effective pixel size in the transverse direction.

Chapter 3

Experimental Setup

Lensless microscopy or lensless Holographic Microscopy (LHM), is an emerging and promising imaging technique distinguished by its simplicity and compact configuration, often eliminating traditional optical lenses. Unlike conventional microscopes that rely on complex optical systems for image formation, lensless systems replace these lenses with computational algorithms that process light scattered by the sample. [20]
This technique is based on the original holographic principle proposed by Gabor in 1948 to enhance electron microscopy resolution. The fundamental concept involves recording an interference pattern, known as a hologram, which encodes both the amplitude and phase of the object's light wave, unlike conventional photography that only records intensity. [**?**]
Experimental setups for lensless microscopy are typically remarkably simple, contributing to advantages such as low cost, portability, and a large field of view (FOV).

A typical lensless microscope requires only a few principal components [42], including: (1) A light source, which may be a laser diode (LD) or light-emitting diode (LED). Semiconductor laser sources, such as those from Blu-ray players, are valued for their compactness and efficiency. LEDs are also employed due to their lower cost, high reliability, and reduced safety concerns, though they may require spatial filters to improve coherence. [18] (2) A pinhole (spatial aperture), commonly used to generate a diverging spherical point source. [14] The pinhole diameter is critical for image quality and illumination coherence. [42] (3) The sample under study, positioned between the light source and detector. For in-line microscopy, samples are typically small and semi-transparent. (4) A digital image sensor, usually a CCD (charge-coupled device) or CMOS (complementary metal-oxide-semiconductor) camera. Advances in CMOS technology have increased their adoption due to enhanced sensitivity and reduced pixel size. (5) A processing unit (computer) for sample acquisition and processing. [18]

3.1 Experimental Setup for lensless Microscopy

The first implemented experimental arrangement was a classical lensless microscopy configuration. Hologram recording utilized a $532nm$ wavelength laser beam and a system comprising a $40X$ microscope objective with a $20\mu m$ pinhole. This assembly functioned as a spatial filter and beam expander to uniformly illuminate the sample. Polystyrene microspheres deposited on a glass slide served as the test object. The setup is illustrated in Fig. **3-1**.

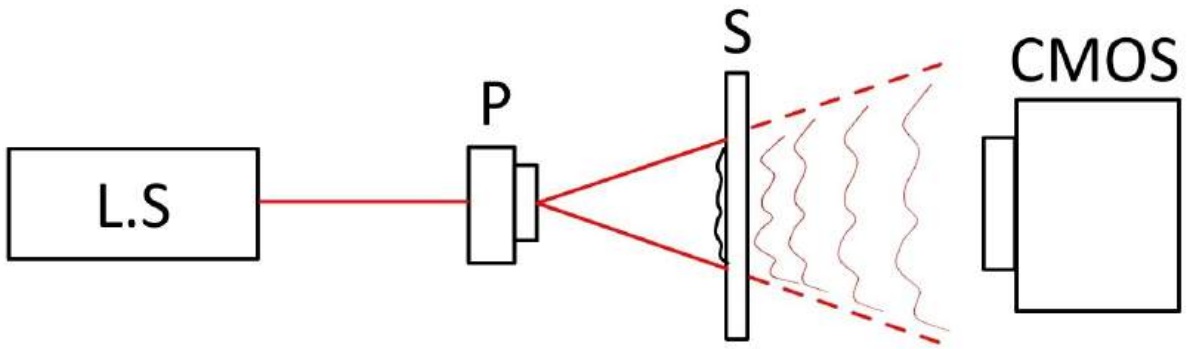

Figure 3-1: Experimental setup for holographic recordings. **L.S.**: Illumination source, **P**: Beam expanding system, **S**: Sample under study, **CMOS**: CMOS sensor for holographic recording.

The beam from the illumination source (L.B.) impinges on the beam expanding system. After expansion, it illuminates the sample, and the light transmitted through the microspheres and coverslip strikes the CMOS sensor. For this experiment, a monochromatic CMOS sensor of 2.3 MP with $4.8 \times 4.8\mu m$ pixel size with a pixel depth of 10 bits and $1920X1200$@165 FPS resolution model MV-SUA202GM was used.
The reference beam was defined as the light transmitted through the coverslip with a refractive index of 1.515 alone, while the object beam corresponded to light diffracted by the red polystyrene microspheres with average sizes between $53 - 63\mu m$. These beams interfered at the sensor plane, where holograms were recorded for subsequent complex optical field reconstruction (see appendix A).

3.2 Experimental Setup for Spatially Controllable Coherence Source

For the development of this research project stage, a modification to the illumination source of the system shown in Fig. **3-1** was implemented. Instead of directly using the highly

coherent illumination source represented in the system as $L.S$, a system to control the spatial coherence of the illumination source was implemented, as depicted in Fig. **3-2**.

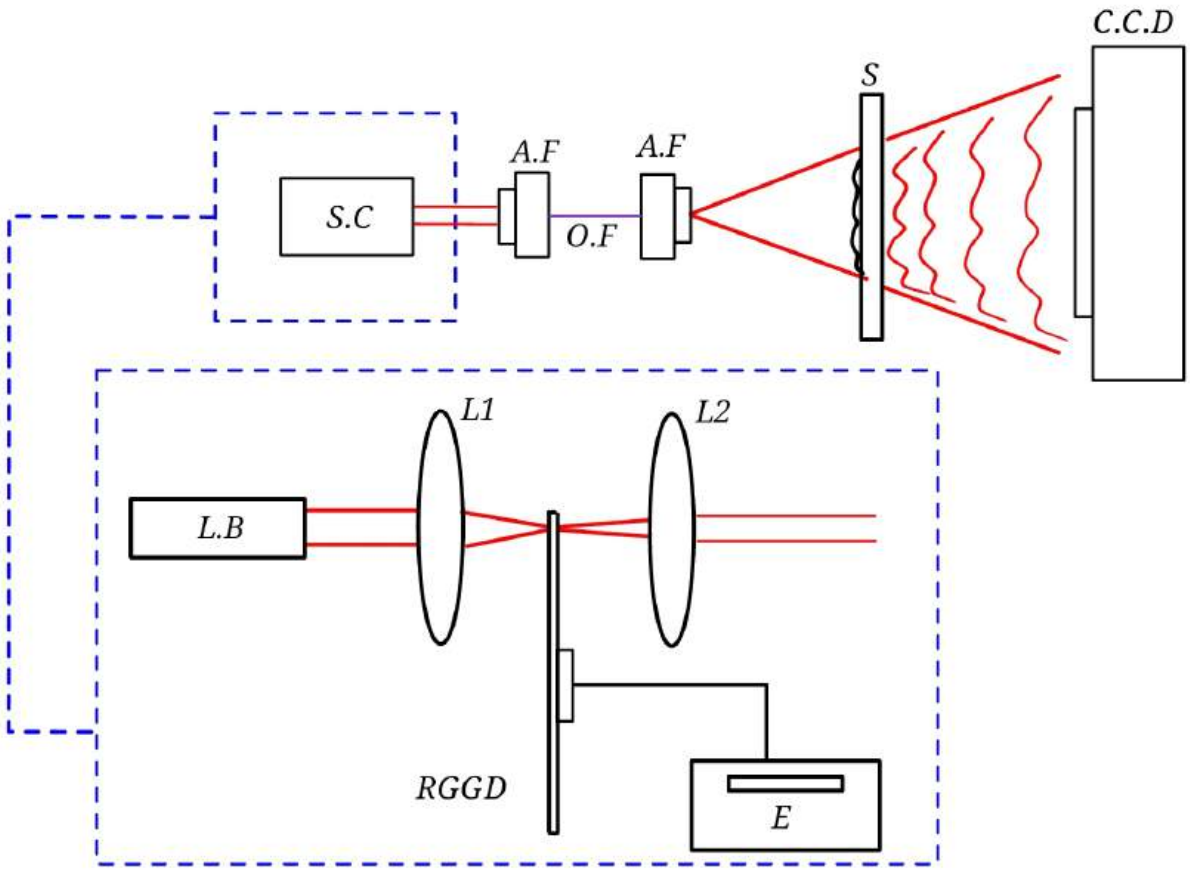

Figure 3-2: Experimental setup for a lensless microscopy system and schematic of the proposed configuration to obtain a partially coherent beam of the Schell-Gaussian model. $S.C$: Illumination source with controlled coherence, $L.B$: $532nm$ laser source, converging lenses L_1 and L_2, $RGGD$: rotating optical diffuser, $A.F$: Optical fiber couplers. $O.F$: Optical fiber. S: Sample. E: Stepper motor. $C.C.D$: CCD camera.

The inset represents the various components comprising the source ($S.C$), utilizing the high-coherence illumination source with a wavelength of $532nm$, followed by a lens (L_1) and a rotating diffuser disk with variable grain size (models DG10-120-F01, DG10-220-F01, DG10-600-F01, and DG10-1500-F01[1], for different tests) positioned at the Fourier plane of this lens. Following the diffuser, a second lens (L_2) was placed at its focal length distance (note this is a collimator system with a diffuser at the Fourier plane). A motor connected to the diffuser disk was installed to rotate it at various speeds, thereby controlling the spatial coherence of the illumination source.

[1]The number 120, 220,600 and 1500 refers to the approximate number of grains per square inch

For the optical fiber tests, multi-mode optical fibers were used. Initial tests employed fibers with $400\mu m$ core diameters, followed by $100\mu m$ and $50\mu m$ fibers respectively. Tests were conducted with various diffuser disk assemblies, lens focal lengths, and fiber sizes to determine the role of each element in reconstruction results and identify the optimal combination of optical components; for instance, different grain sizes offer scattering ranging from fine to coarse. Finer grains produce a small diffusion pattern, while coarser grains yield a broader diffusion pattern, as observed in Fig. **3-3**.

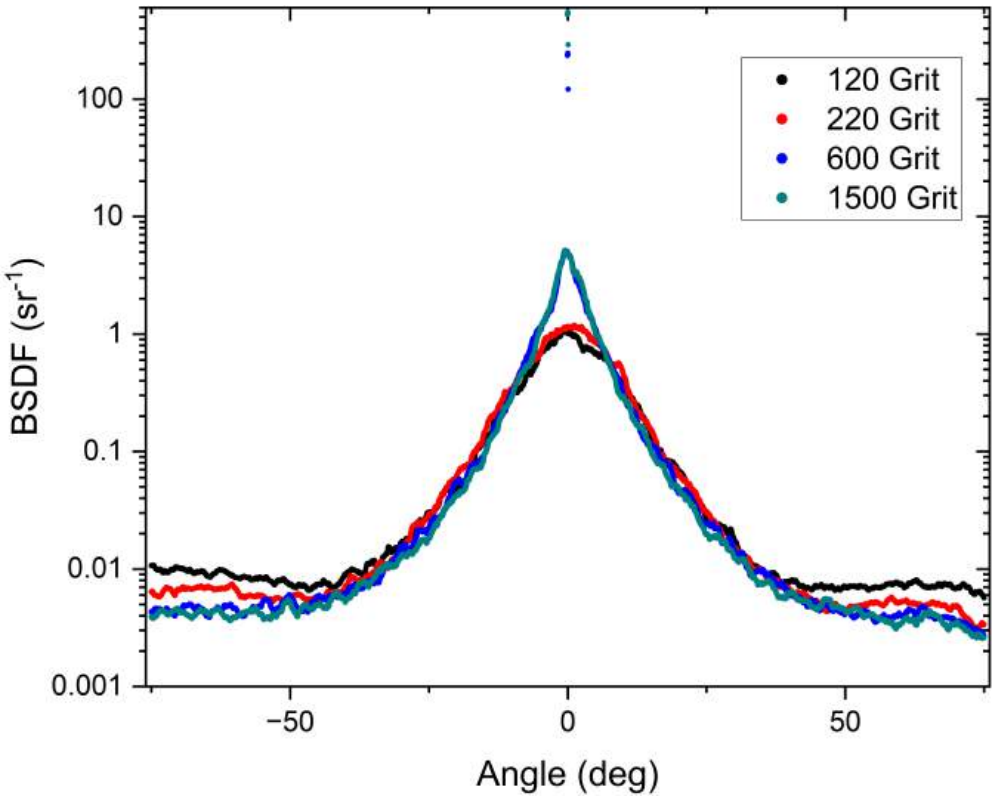

Figure 3-3: Bidirectional Scattering Distribution Function

Speckle pattern formation is inherently non-deterministic. This results from the random nature of microscopic height variations (roughness) on a surface when illuminated by coherent laser light. Each point on this surface acts as a light scattering center. Random height differences between these points induce corresponding random phase variations in the scattered light. When these randomly phased scattered waves coherently interfere at an observation plane (such as a sensor or screen), the characteristic speckle pattern emerges.

Typical dimensions of individual speckle grains are on the order of the diffraction limit, expressed by the relation $\lambda z/D$; where λ is the light wavelength, z is the distance from the diffusing surface to the observation plane, and D is the diameter of the laser beam incident on said surface [47]. To mitigate the adverse effect of speckle in imaging systems, a rotating

diffuser disk is commonly employed. The rotation drastically reduces the coherence time ($\tau c = a/v$, where a is the beam diameter and v is the tangential velocity of the diffuser). When this effective coherence time is significantly shorter than the detector exposure time, the highly dynamic speckle pattern averages out during capture. This temporal averaging is essential for suppressing speckle-associated visual noise and consequently improving perceived image quality. [47]

3.3 Contrast Coefficient Measurement

A challenge with highly coherent sources is increased speckle, arising from mutual interference of coherent waves scattered from rough surfaces. Speckle patterns are characterized by detectors responding to optical intensity rather than complex amplitude. For fully developed speckle, the intensity distribution follows [47, 69, 70, 71]:

$$p_I = \frac{1}{\langle I \rangle} \exp\left(\frac{-I}{\langle I \rangle}\right) \tag{3-1}$$

where $\langle I \rangle$ denotes mean intensity. Speckle magnitude is quantified by contrast, defined as the ratio of standard deviation to mean intensity:

$$C = \frac{\sigma_I}{\langle I \rangle} \tag{3-2}$$

where σ_I is the standard deviation of the speckle intensity pattern.

Using equation (3-2) and the experimental setup shown in Fig. **3-2** without any sample, recordings were performed to determine the coefficient as a function of the rotation speed of the diffuser disks, employing a different diffuser disk for each test (See appendix B).

3.3.1 Verification of a Schell-Gauss model source

An experimental setup was arranged to perform a Young's double-slit experiment to verify the correlation between various points across the screen by calculating the fringe visibility. The following experimental configuration was implemented:

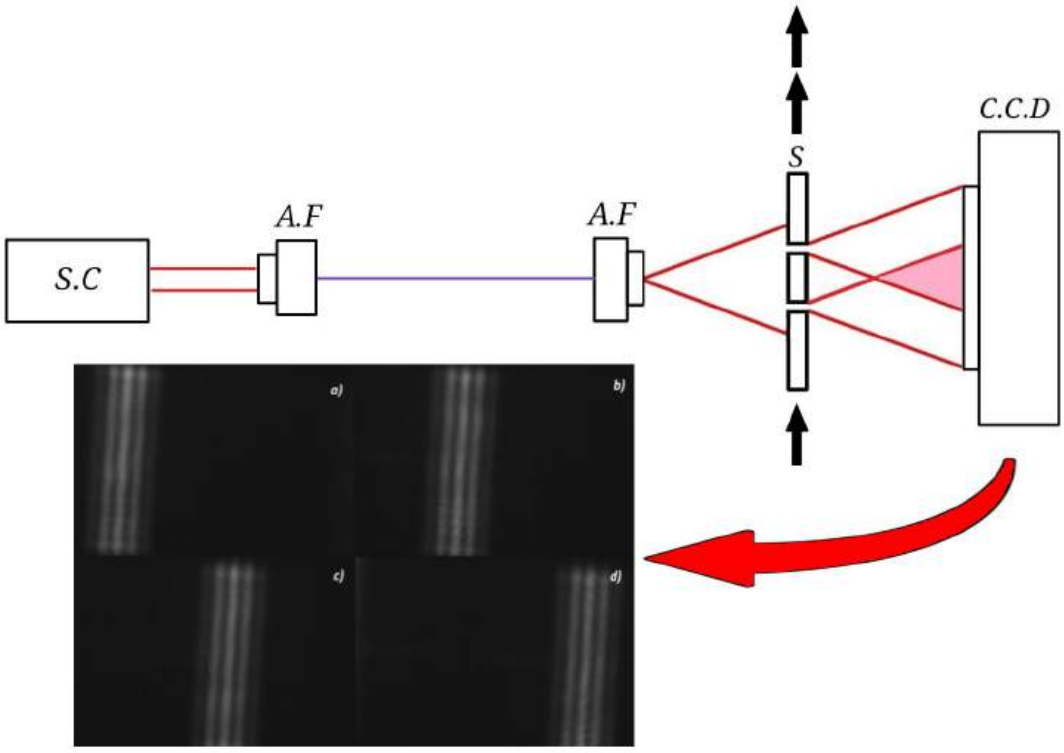

Figure 3-4: Modified experimental setup for the Young's experiment. $S.C$: Illumination source with controlled coherence, $A.F$: Optical fiber couplers. $O.F$: Optical fiber. S: Double slit with $0.08mm$ width and $0.250mm$ slit separation. E: Stepper motor. $C.C.D$: CCD camera. In panels a), b), c) and d), the recording of the interference pattern by shifting the double slit along the observation screen is shown.

For this experimental setup, a double slit was positioned as the sample and translated across the screen. Corresponding recordings were made as the double slit was controllably displaced horizontally. Intensity profiles were obtained by vertically scanning all pixel rows from the top to the bottom of the sensor, calculating average visibility values and associated uncertainties for each holographic recording (see appendix C). This experiment allowed us to verify one of the properties of Schell-Gauss model sources, which states that spatial coherence does not depend on the absolute positions of the radiating elements, but only on the differences between their positions.

3.3.2 Computational implementation

For the computational implementation of the contrast coefficient, visibility coefficient, propagation and reconstruction, and metric calculations, several programs were developed using MATLAB software (see appendix A. For the reconstruction of the amplitude and phase of the optical complex field, propagation methods utilizing the Fresnel approximation, as well

as angular spectrum propagation, are employed. These methods reconstruct the amplitude and phase of the complex optical field.

After obtaining these fields, the calculation of metrics for each propagation distance z between the sensor and the illumination source is executed in parallel. Alternatively, a region of interest can be defined. Finally, to enable comparative analysis between metrics, the results for each metric are normalized. Uncertainties associated with each metric are also calculated (see appendices B, C and D).

3.4 Samples study

As study samples, polystyrene microspheres reference $REDPMS - 0.98$ with average size between $53.63\mu m$ arranged on different planes were used. Some samples were positioned very close to the sensor plane, while others were placed approximately $2cm$ away from the sensor. For lateral calibration and calculation of the system resolution limits, a U.S.A.F. 1951 resolution test target (as described in Fig. **3-5**) was employed, containing groups from 2 to 7. Finally, biological samples of molar tissues were utilized; samples supplied by the laboratory *Laboratorio de Citopatología, Neuropatología, Anatomía Patológica, Inmunohistoquímica y Biología Molecular (CITOPAT)*; the detailed information will be shown in the analysis chapter.

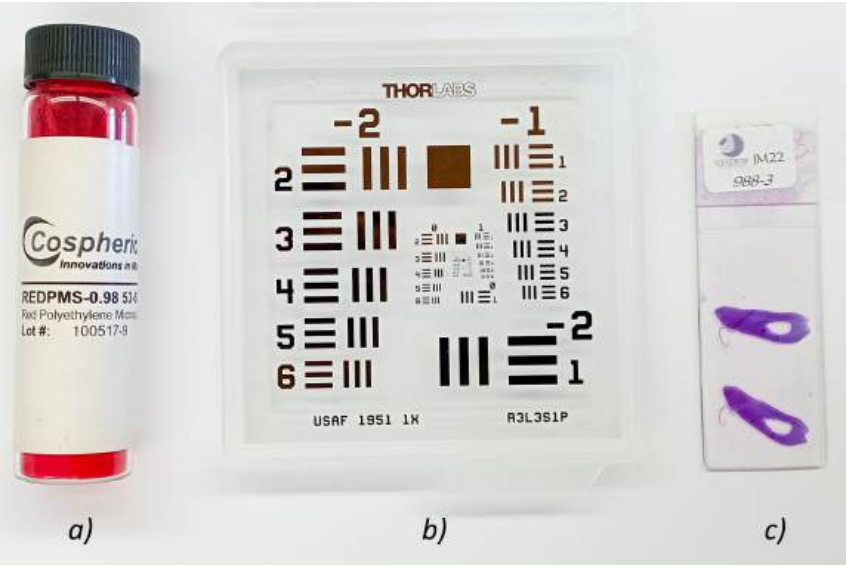

Figure 3-5: a) polystyrene microspheres reference $REDPMS - 0.98$. b) a U.S.A.F. 1951 resolution test target. c) biological samples of molar tissues.

Chapter 4

Results and Analysis

4.1 Lensless Microscopy

The digital hologram, recorded using the experimental setup shown in Fig. **3-1**, was numerically reconstructed at different planes using the algorithm implemented (see appendix A). This propagation distance scanning allows us to select the best reconstruction plane that was located, approximately, at $z = 1225\ \mu m$, This was achieved after conducting 12 experimental trials by varying the sample distance. For these specific tests, it was decided to place the microspheres directly on the sensor's filters. At this stage, the primary objective was solely to verify that the implemented software functioned adequately. For the experiments performed using a source with controllable spatial coherence, other configurations were taken into account. With this in hand, it was possible to contrast the efficiency performance between both numerical reconstruction techniques: the angular spectrum algorithm and the Fresnel propagation method. Furthermore, it was feasible to evaluate the diffractive effects on the reconstructed holograms. Due to the propagation distance, the diffraction pattern spreads over a reduced area at the image sensor plane, preventing adequate intensity sampling. In the case of polystyrene microspheres spread over a cover-slip as the object, high frequency details are lost in the reconstructed image at the optimized propagation distance. At the numerical holographic reconstruction stage, with the aim of compensating for substrate thickness, a reference hologram of the cover-slip clean was acquired to be subtracted.
Fig.s **4-1** and **4-3** exhibit artifacts in the upper-right, lower-right, and left corners, attributed to the Bayer filters of the CCD sensor. This conclusion is supported by comparative tests with reference holograms, where complex optical field subtraction consistently reproduced identical irregularities. These anomalies disappeared when using Bayer-free sensors (naked sensors).
Notably, both reconstruction methods (angular spectrum and Fresnel) show significant similarities: under these experimental conditions, they resolve identical details.

It should be noted that no additional processing techniques were employed, such as pixel

super-resolution (PSR), [72] a method for resolution enhancement using multiple images with sample displacements or the phase retrieval algorithms (e.g., Gerchberg-Saxton), [67] determining phases from image and diffraction plane measurements. This is because the primary objective was to analyze the effects of spatial coherence variation on the resolution of reconstructed objects; hence, these techniques were not implemented. However, their future implementation could be considered.

Figure 4-1: Amplitude reconstruction of the complex optical field at 1225 μm using angular spectrum propagation.

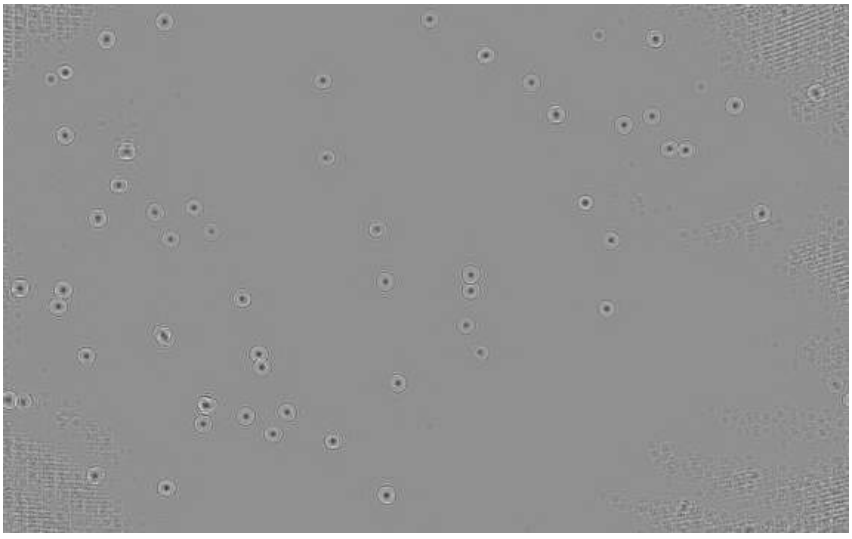

Figure 4-2: Phase reconstruction of the complex optical field at 1225 μm using angular spectrum propagation.

Under identical conditions, the optical field was reconstructed using the Fresnel propagation algorithm. The computed holographic image is shown in Fig. **4-3**

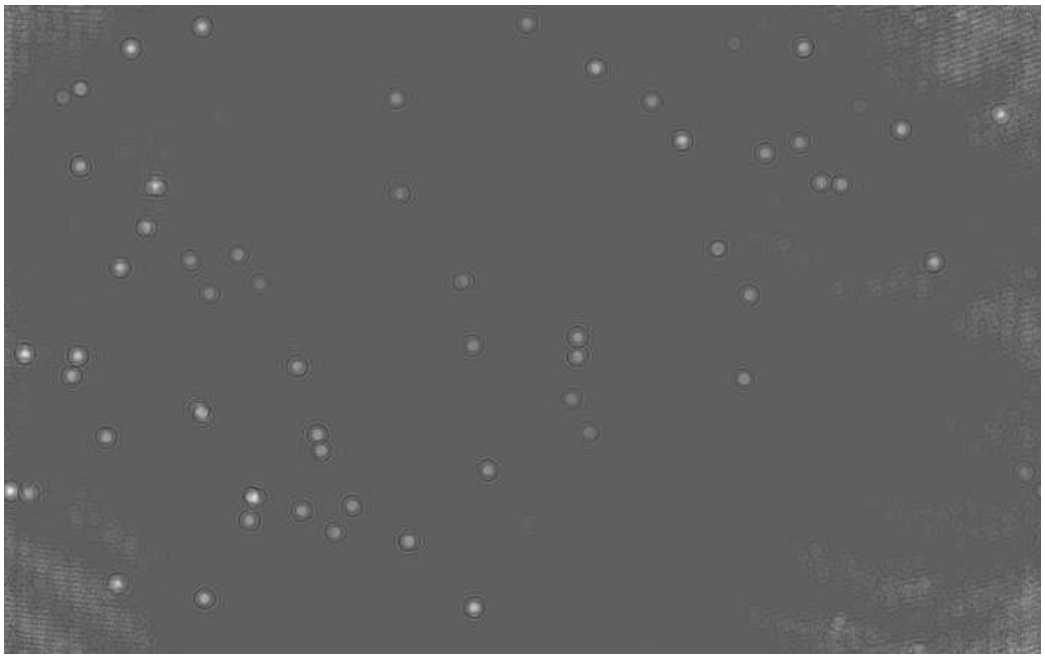

Figure 4-3: Amplitude reconstruction of the complex optical field at 1225 μm via Fresnel diffraction integral.

This experimental stage served as the foundation for implementing the lensless microscopy setup and for testing the developed algorithms, specifically, the angular spectrum method and Fresnel propagation method to reconstruct the amplitude and phase of complex optical fields. It further enabled the identification of key variables for implementing the Schell-Gauss type source.

4.2 Controllable Spatial Coherence Source

Using the experimental setup depicted in Fig. **3-2**, a variable spatial coherence light source was implemented. This pseudo-thermal source employed a high-coherence 532 nm illumination source and diffuser disks from THORLABS (models DG10-120-F01, DG10-220-F01, DG10-600-F01, and DG10-1500-F01). The spatial coherence of the resulting beam was modulated by rotating the diffuser disks.

Intensity distributions were recorded at different speeds while maintaining a fixed exposure time of 4.998 ms for each measurement. The beam incidence point on each diffuser was positioned 9 mm from the rotation center. To obtain robust measurements of the light field statistical properties, 10 recordings were taken for each motion state (i.e., 10 stationary

recordings and 10 recordings for each speed from one to ten revolutions per second (linear speed of v_i=0 m/s, v_f =0.38 m/s)). Average images for each speed were computed from these series. Speckle contrast calculations were performed on these averaged images using Equation (3-2), with associated uncertainties computed for each motion state.

For a configuration using lenses $L_1 = L_2 = 10$ cm focal length and a 400 μm core multimode fiber (defining the spot size on the diffuser), the plot shown in Fig. 4-4.

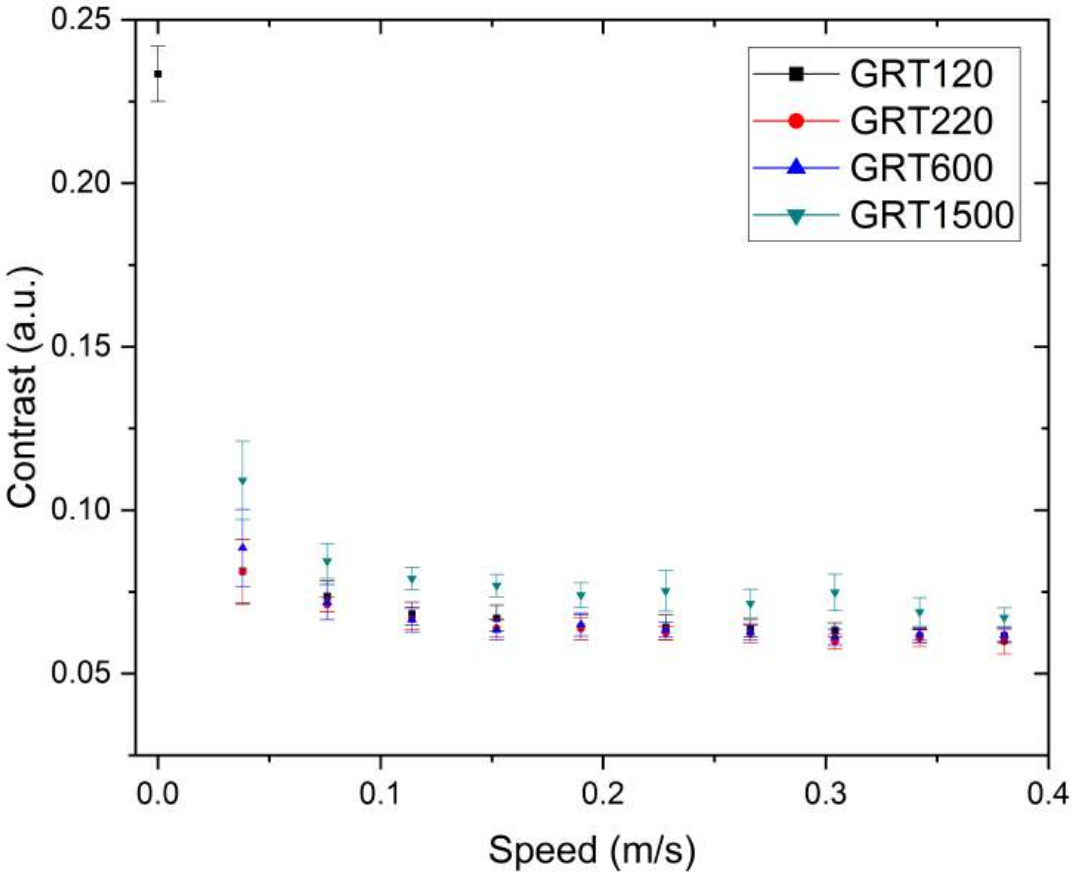

Figure 4-4: Speckle contrast versus rotation speed for $f = 10$ cm focal length lenses.

It is observed that speckle contrast decreases as the diffuser rotation speed increases. This phenomenon is attributed to temporal averaging of speckle patterns at the detector since the exposure time (4.998 ms) is significantly longer than the light field temporal coherence time (determined by the linear spot velocity on the diffuser). Additionally, the calculated uncertainties decrease substantially, consistent with the expected reduction in statistical fluctuations from this averaging process.

To visualize the reduction in data dispersion more clearly, the coefficient of variation (CV) was computed. In this context, CV is analogous to speckle contrast and is defined as:

$$\mathrm{CV} = \left(\frac{\sigma}{\bar{x}}\right) \times 100\% \tag{4-1}$$

where σ denotes the standard deviation of a data series and $\bar{x}$ represents its arithmetic mean. The following plot illustrates how dispersion values decrease with diffuser rotation speed:

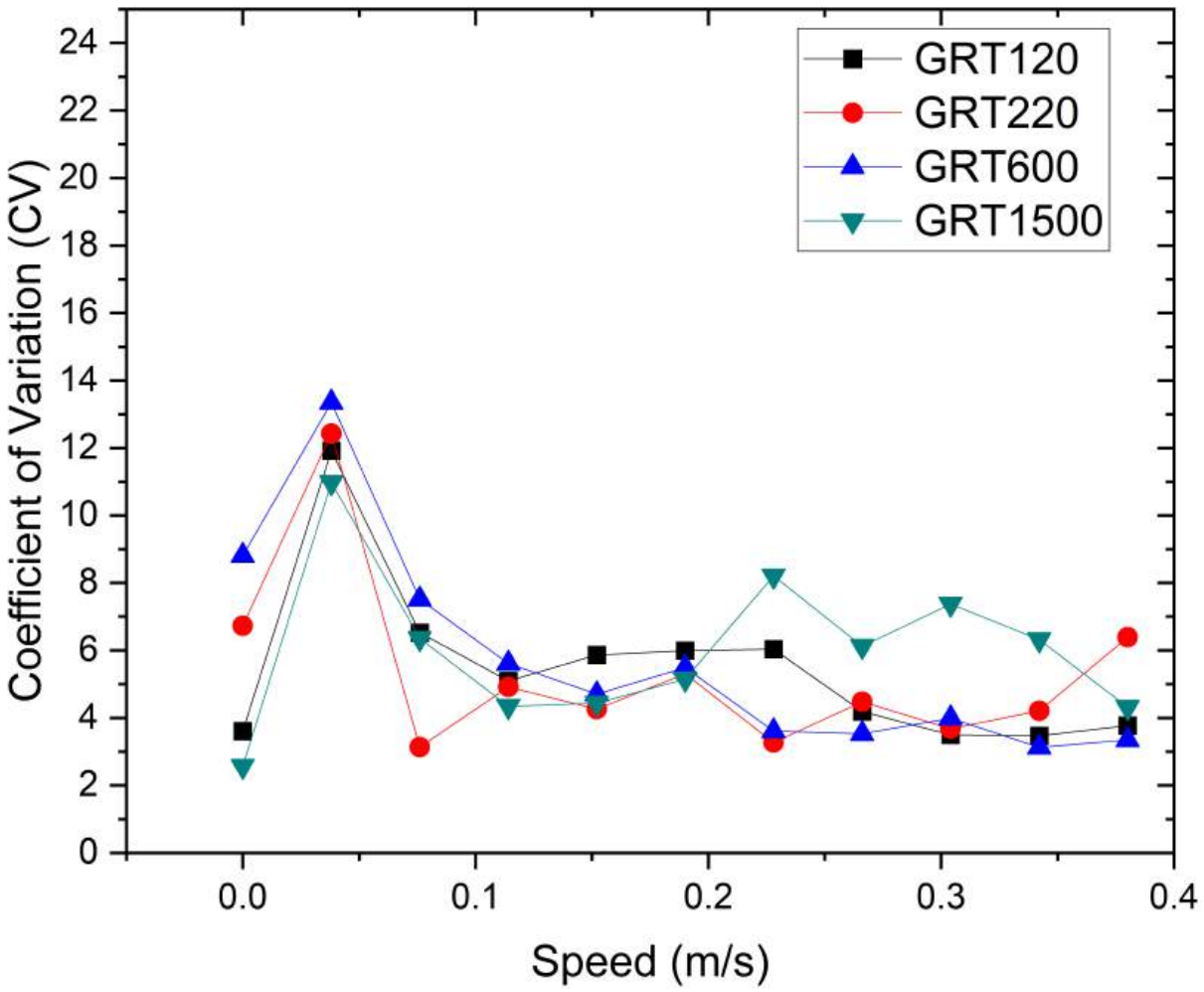

Figure 4-5: Coefficient of variation versus diffuser rotation speed for $L_1 = L_2 = 10\ cm$ lenses

Fig. 4-5 shows that the computed dispersion values (i.e., speckle contrast) converge to between 3% and 4% for most disks, indicating strong speckle suppression and approaching spatially incoherent light. However, the DG10-1500-F01 diffuser exhibits distinct behavior with consistently higher residual contrast values.

This result correlates with the intrinsic properties of the diffuser disk shown in Fig. 3-3, as this is the only disk whose Bidirectional Scattering Distribution Function (BSDF) approaches high values at normal light incidence. This suggests that its inherent scattering characteristics (potentially related to the correlation length of its surface roughness) affect the efficacy of

temporal averaging, resulting in less complete speckle suppression.

Rotating diffuser disks are an effective component for reducing speckle and enhancing image uniformity in optical systems. As illustrated in Fig. 4-6, as the diffuser rotation speed increases (from 0 m/s to 0.38 m/s), the captured image becomes visually more uniform with reduced noise. This phenomenon occurs because continuous diffuser rotation generates multiple statistical realizations of the speckle pattern within the detector's integration time, resulting in the averaging of intensity fluctuations. Speckle, a random granular pattern, is a type of coherent noise arising from the interference of coherent light scattered by optically rough surfaces.

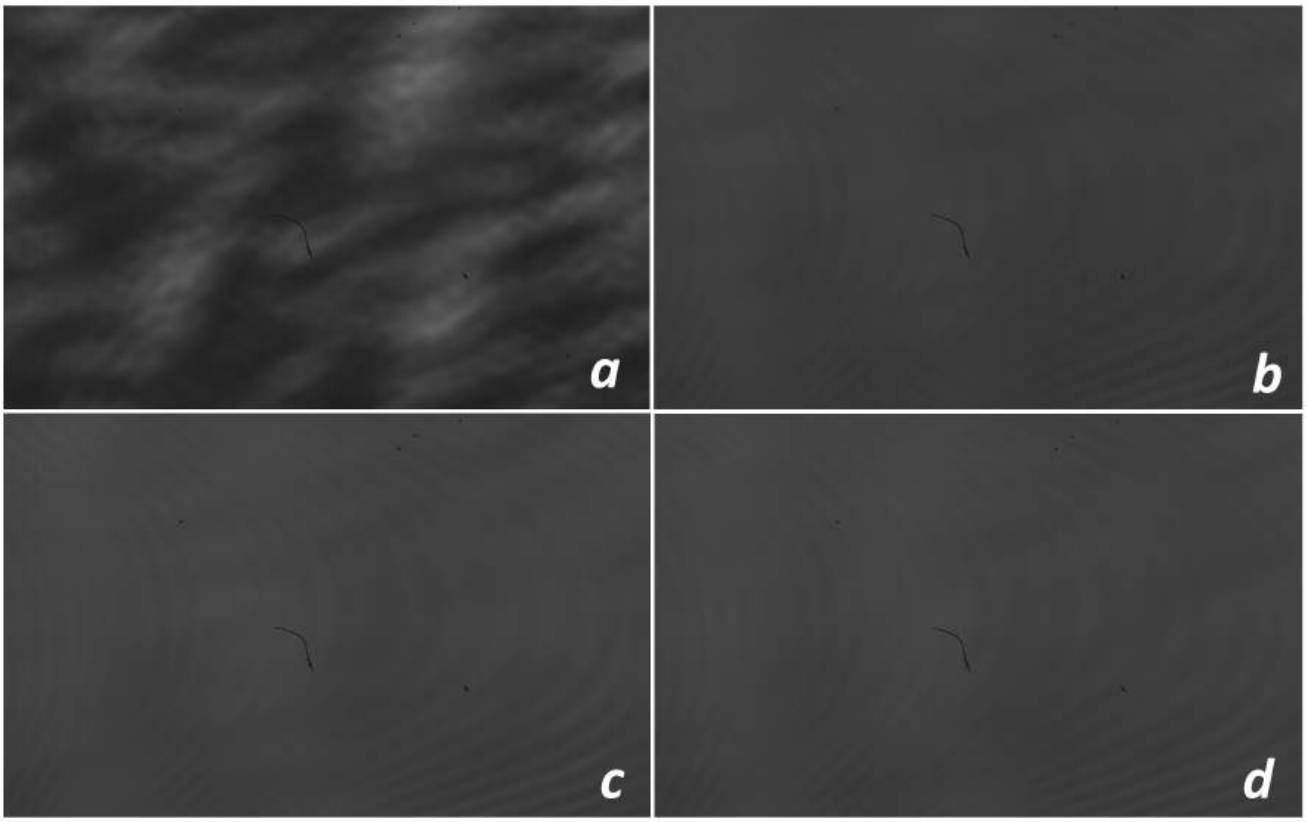

Figure 4-6: Intensity distributions using DG10-120-F01 diffuser filter. a) 0 m/s, b) 0.114 m/s, c) 0.228 m/s, d) 0.38 m/s.

Speckle reduction is quantitatively reflected in the probability distribution of recorded intensities. Analysis of intensity histograms obtained with a diffuser disk system (such as DG10-120-F01) reveals in the Fig. 4-7.

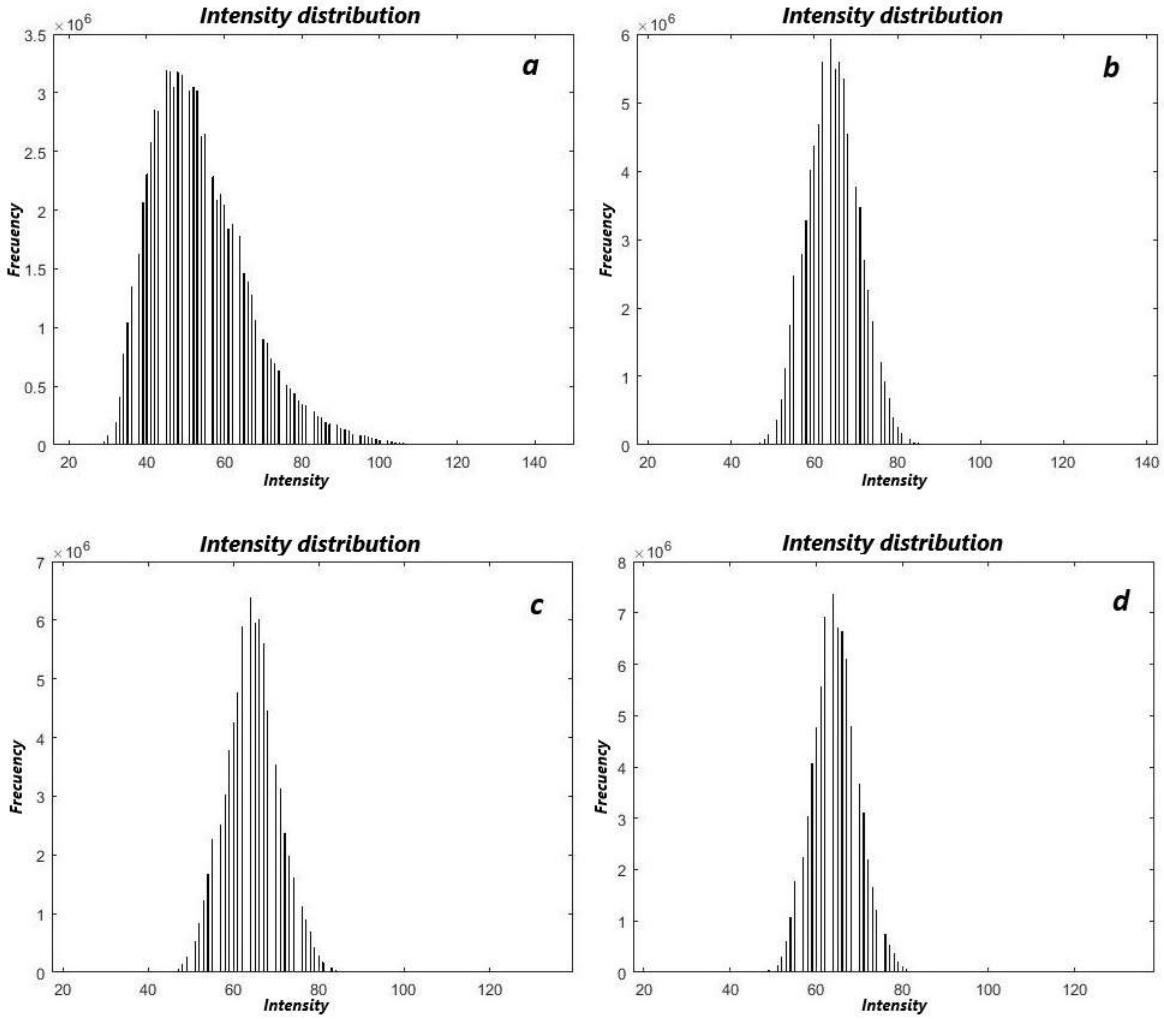

Figure 4-7: Intensity histograms for DG10-120-F01 diffuser filter at various rotation speeds. a) 0 m/s, b) 0.114 m/s, c) 0.228 m/s, d) 0.38 m/s.

When the diffuser disk is stationary, the intensity distribution (Fig. 4-7a) behaves similarly to that of a pseudo-thermal source. In this state, fully developed speckle intensities follow a negative exponential distribution. This characteristic is a hallmark of speckle patterns formed by interference of numerous random phasors [47, 45].

As diffuser rotation speed increases, faster intensity fluctuations occur; the detector averages a greater number of independent speckle patterns during its exposure time. Consequently, intensity histograms progressively cluster around a mean value. The probability distribution of integrated intensity tends to approach a Gaussian form, with its width (variance) decreasing significantly. This contraction of intensity distribution directly manifests effective speckle contrast reduction, leading to a smoother final image. This behavior is consistent with properties expected from partially coherent light sources, such as those characterized by

Gaussian Schell-model (GSM) sources.

Now, modifying the focal length such that L_1 remains at 10 cm while L_2 is adjusted to 5 cm, and repeating the procedure described for the previous configuration yields the following comparative plot:

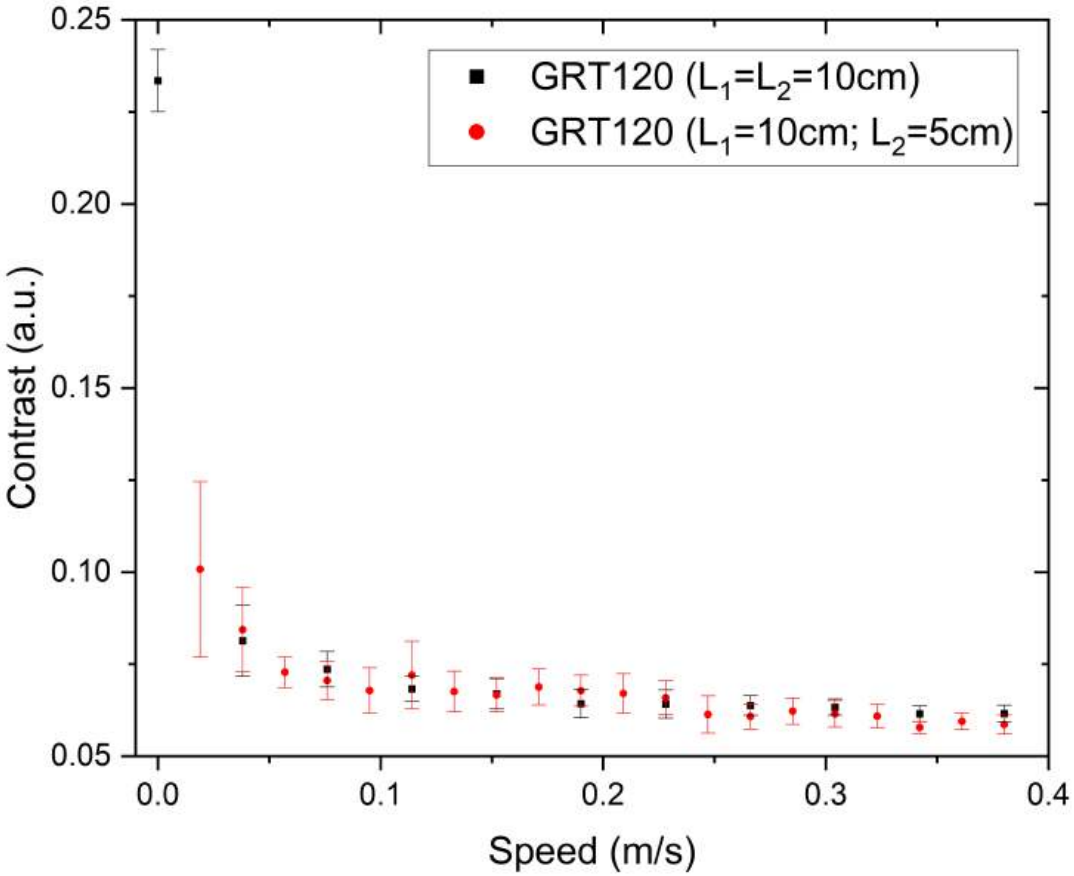

Figure 4-8: Speckle contrast versus rotation speed for DG10-120-F01 diffuser disk, comparing configurations $L_1 = L_2$ =10 cm versus L_1 =10 cm and L_2 =5 cm.

Fig. 4-8 shows statistically indistinguishable speckle contrast behavior between the $L_1 = L_2$ = 10 cm and L_1 = 10 cm with L_2 = 5 cm configurations. This result aligns with Gaussian Schell-model (GSM) source theory. The spatial coherence width of the GSM source is primarily governed by the size of the laser beam focused spot on the diffuser disk (denoted w_0), which is determined by lens L_1.
Since L_1 the focal length remained constant (10 cm) in both configurations, the spot size w_0 on the diffuser remained essentially identical. Furthermore, a fundamental property of GSM beams is the invariance of the coherence width to beam radius ratio when propagating through optical systems such as lenses. Therefore, although the lens L_2 altered the output beam size by changing its focal length, it proportionally scaled both beam size and coherence

width, preserving their effective coherence ratio. As speckle contrast directly reflects this relative beam coherence, and the rotating diffuser temporally averages the speckle, residual speckle behavior showed no significant changes between configurations.
Upon implementing a new modification to the experimental setup, lens L_2 was replaced by a lens with a focal length of 15 cm; additionally, the 400 μm optical fiber was replaced by a 105 μm optical fiber. The results are presented in Fig. 4-9

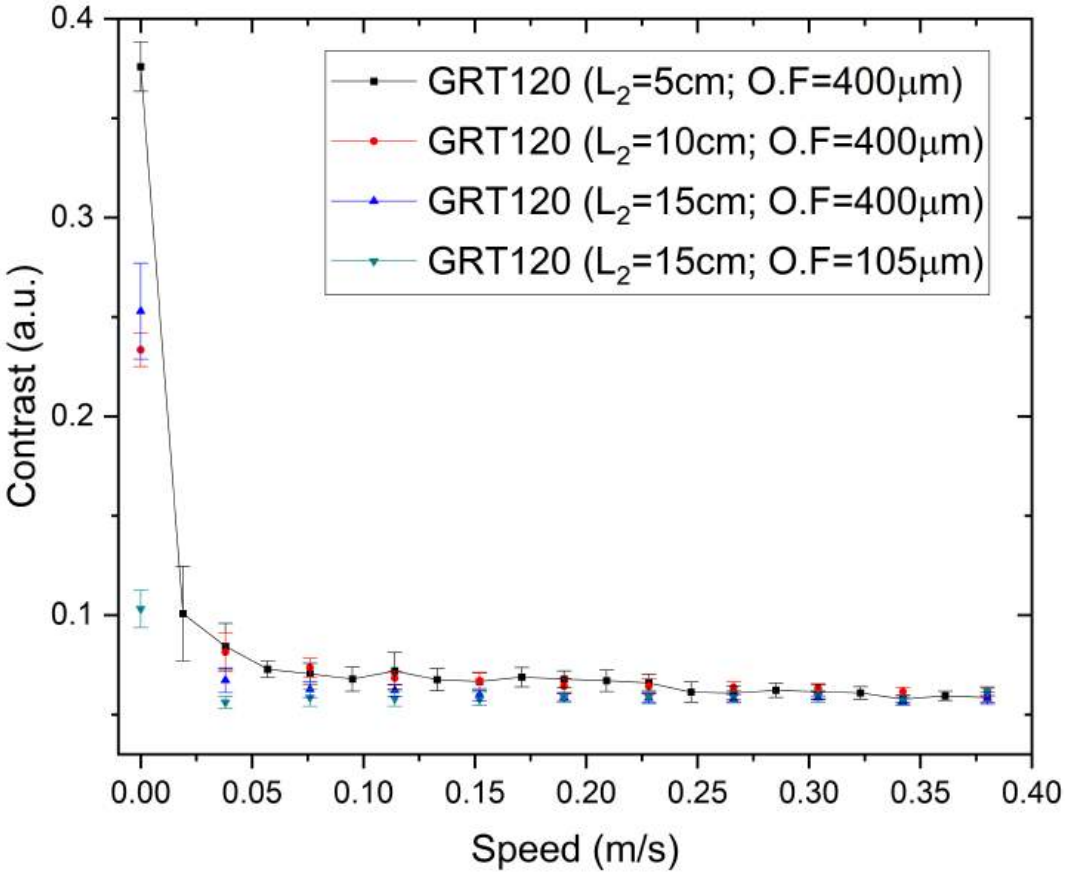

Figure 4-9: Plot of speckle contrast vs. rotation speed using diffuser disk DG10-120-F01 and comparison of configurations L_2 =50 cm, L_2 =10cm, L_2 =15 cm with 400 μm optical fiber, versus configuration with L_2 =15 cm and 105 μm optical fiber

From Fig. 4-9, it can be observed that although the speckle contrast values at rest are lower for the configuration with 105 μm optical fiber (and lens L_2 = 15 cm) compared to the 400 μm optical fiber configurations (with lenses L_2 = 50 cm, L_2 = 10 cm, L_2 = 15 cm), a result that might suggest reduced effective spatial coherence in the 105 μm configuration, [9] as the rotation speed of the diffuser disk increases, both configurations exhibit asymptotic convergence toward the same average speckle contrast value. This asymptotic behavior is explained by effective speckle suppression through temporal averaging of the intensity patterns generated by rapid diffuser disk rotation. This process reduces coherent noise, [8]

driving the speckle contrast to a minimum stable value representing the average illumination, independent of the initial static coherence conditions of the beam. [47]
The key findings of this section reveal that following experimental modifications, including replacement of lens L_2 with a 15 cm focal length lens and substitution of the optical fiber with 105 μm core, the system exhibited lower initial speckle contrast values compared to previous 400 μm configurations. This initial contrast reduction is particularly intriguing since smaller fiber diameters typically correlate with higher spatial coherence, [9, 20] which would theoretically produce higher speckle contrast under static conditions. Despite these differences in static coherence properties, all evaluated configurations (both 400 μm and 105 μm fibers) demonstrated asymptotic convergence to the same minimum speckle contrast value as the diffuser rotation speed increased. This unified behavior confirms effective speckle suppression achieved through temporal averaging of intensity patterns, which drastically reduces coherent noise and *erases* initial coherence variations of the beam incident on the diffuser.

4.3 Experimental Verification of a Schell-Gauss Model Source

To verify that the illumination source behaves as a Schell-Gauss source – as previously discussed in Section 2.3.2 regarding lensless microscopy systems with variable spatial coherence achieved through rotating diffusers – the following checks must be performed, consistent with statistical optics principles:

- **Statistical Properties Verification (Diffuser Effect)**: Intensity frequency distributions (histograms) from the source must cluster around a central value. The spread of these distributions should decrease with higher diffuser rotation speeds, as anticipated in Fig. **4-7**. This behavior characterizes pseudo-thermal sources from rotating diffusers, where temporal averaging of speckle fluctuations increases the effective *degrees of freedom* captured during fixed integration times. Higher degrees of freedom reduce intensity measurement dispersion around the mean, indicating enhanced statistical stability and effective temporal averaging.

- **Spatial Coherence Homogeneity (Young's Experiment)**: For Schell-Gauss sources, the modulus of the complex degree of spatial coherence ($|\mu|$) must remain invariant under lateral shifts of a double-slit across the source plane while maintaining fixed slit separation. This spatial homogeneity reflects the defining feature of Schell-model sources where coherence depends solely on the vector difference $r_2 - r_1$, not absolute positions. Crucially, while a Gaussian intensity profile causes individual slit intensities (I_1, I_2) to vary during translation affecting the classical fringe visibility

$V = 2\sqrt{I_1 I_2}/(I_1 + I_2) \cdot |\mu|$ – the coherence modulus $|\mu|$ itself must stay constant for fixed slit separation to confirm Schell-model behavior.

The experimental setup (Fig. **3-4**) employed four double slits:

- Slits A and B: widths 0.04mm with separations of 0.25 mm and 0.50mm respectively.
- Slits C and D: widths 0.08mm with separations of 0.25 mm and 0.50mm respectively.

This configuration probes coherence properties under different spatial sampling conditions.

Young's experiment used a 532 nm source with a Thorlabs DG10-120-F01 diffuser. Double-slit positions were shifted in 25 μm steps across the source plane to sample representative beam regions. This procedure evaluates spatial homogeneity of the degree of coherence, a hallmark of Schell-model sources where coherence depends exclusively on point separation, not absolute location.

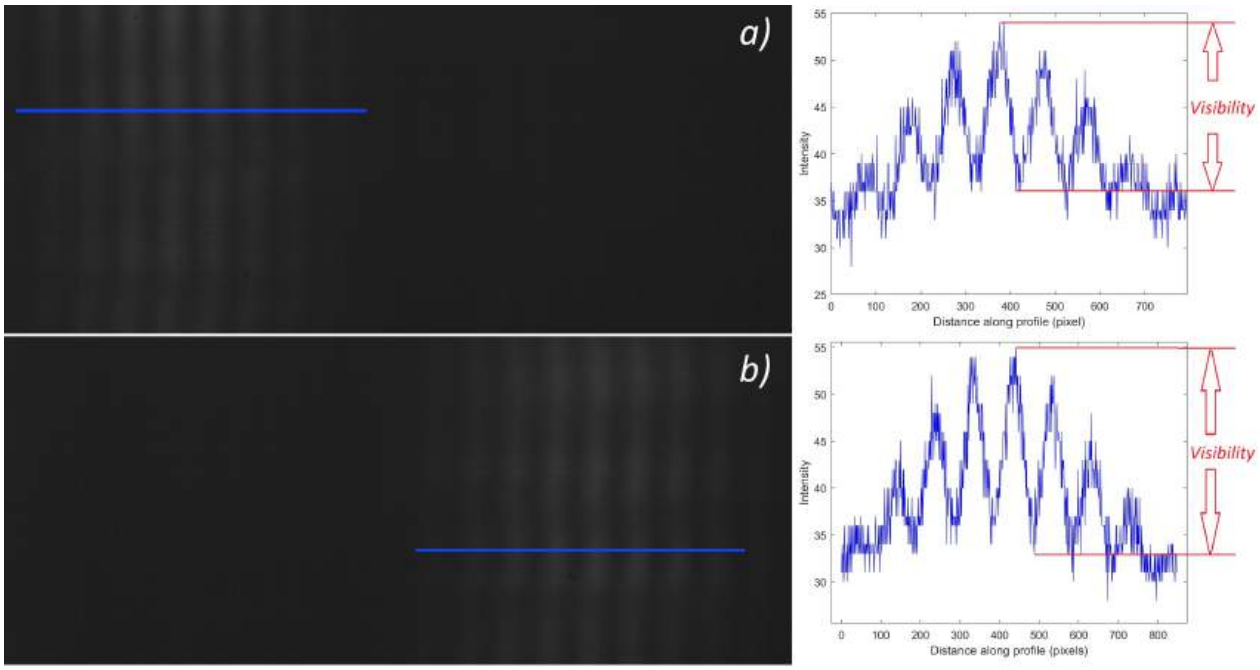

Figure 4-10: Interference patterns using double-slit A (0.04 mm width, 0.25 mm separation) with DG10-120-F01 diffuser at ∼0.314 m/s rotation speed.

Interference patterns (e.g., Fig. **4-10** a-b) are shown regions (1920 × 800 pixels) with full vertical coverage of interference fringes. Quantitative analysis employed horizontally averaged profiles across all 800 vertical pixels, computing the mean and standard deviation for all 98 captured images.

Experimental results are summarized in:

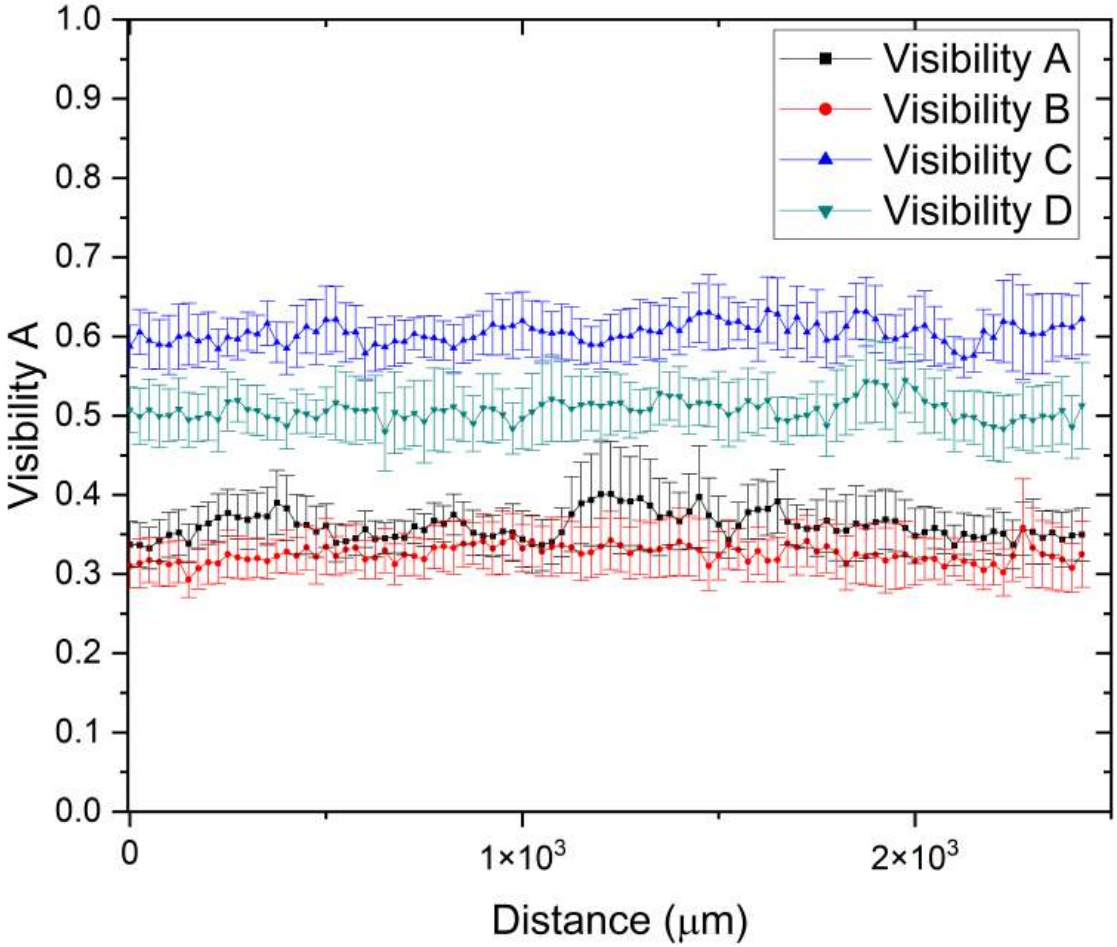

Figure 4-11: Fringe visibility vs. displacement for slits A-D using DG10-120-F01 diffuser at ∼0.314 m/s

Fig. 4-11 demonstrates behavior consistent with Schell-Gauss theory: The complex degree of spatial coherence (and thus fringe visibility in Young's experiment) depends fundamentally on sampled point separation, not absolute position. Constant visibility during slit translation confirms spatial coherence homogeneity.

Visibility measurement reliability was quantified via coefficient of variation (CV): $CV_A = 9.42\%$, $CV_B = 9.66\%$, $CV_C = 5.67\%$, $CV_D = 7.58\%$. Lower variability for slits C-D (<7.58%) versus A-B (>9.42%) indicates superior statistical stability. Consequently, subsequent analyses used slits C-D as they provide more consistent ensemble-averaged field properties from the rotating diffuser.

To understand the relevance of using an illumination source with controllable spatial coherence, such as the Schell-Gauss source implemented in our initial experiment, a series of comparative tests were performed. The purpose of these experiments was to demonstrate how the visibility behavior of interference fringes manifests under different illumination source coherence

conditions. Three distinct scenarios were configured:

- **Source with controllable spatial coherence (Schell-Gauss model)**: This scenario replicates the pseudo-thermal source generated by laser illumination on a rotating diffuser disk. As established in our initial experimental setup, such sources are expected to maintain relatively constant fringe visibility when displacing the double-slit, indicating spatial homogeneity of the coherence degree after ensemble averaging of instantaneous field realizations.

- **High spatial coherence source**: A 532nm wavelength laser source with high coherence was used. For an ideally coherent source, near unity fringe visibility (maximum contrast) is anticipated in the Young's interference pattern. On average, higher visibility values are expected compared to sources with variable spatial coherence.

- **Pseudo-thermal source (stationary diffuser disk)**: In this third scenario, the diffuser disk remained static. Crucially, unlike the rotating diffuser case where coherence statistics are averaged, a stationary diffuser generates a static speckle pattern. The observed visibility in this case therefore represents neither the ensemble-averaged spatial coherence degree nor the inherent speckle contrast within a single instantaneous realization of the optical field. This setup allows direct evaluation of static speckle's impact on interference pattern observation.

The geometric and optical parameters from the initial Young's experiment were maintained, with only the exposure time modified to 2.5952 ms to avoid saturation effects on the interference patterns of the different double slits. Experiments were performed on double slits C and D, selected for their demonstrated measurement stability and reliability. All three sources were tested on slit C, while only comparative plots between the controllable-spatial-coherence source and the high-spatial-coherence source were generated for slit D.

For double slit C, the results illustrated in Fig. **4-12** were obtained:

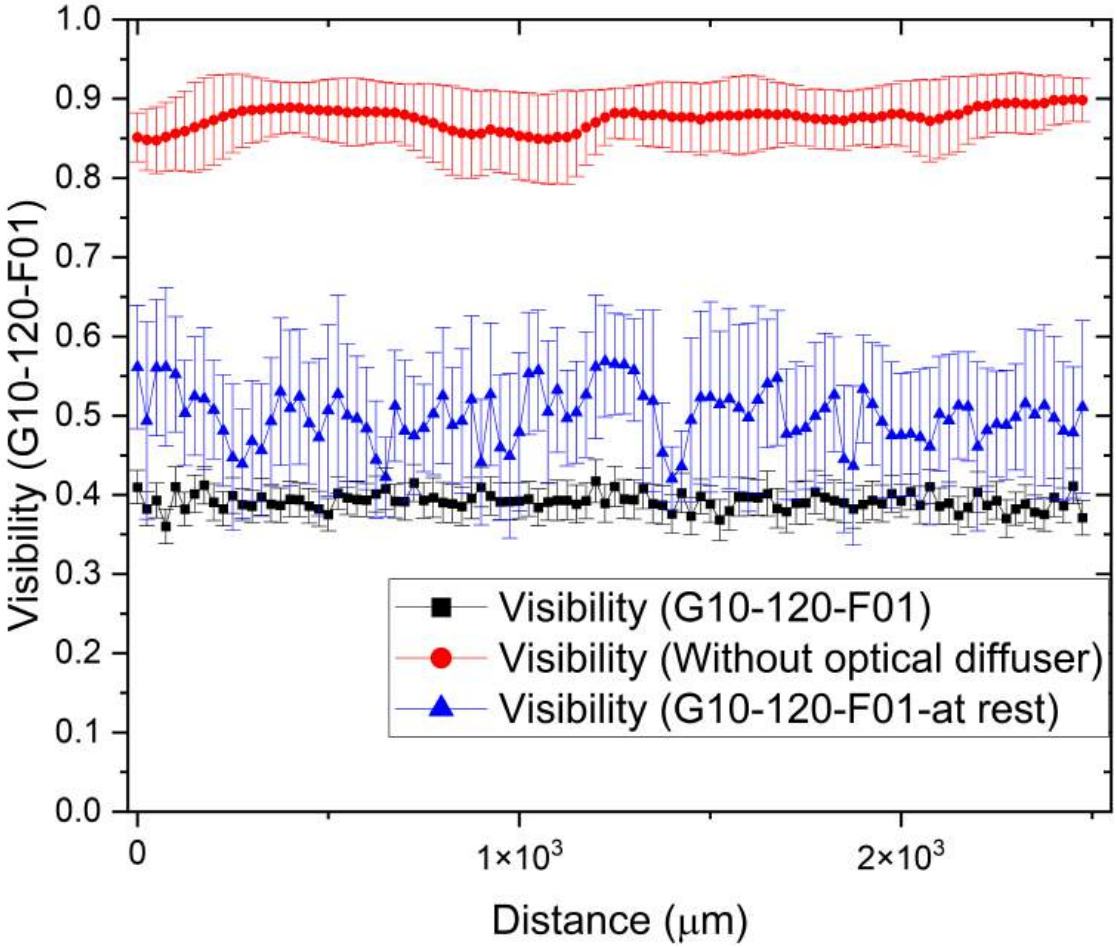

Figure 4-12: Visibility versus displacement for slit C with DG10-120-F01 diffuser disk stationary, rotating at approximately 0.314 m/s, and without diffuser.

Fig. 4-12 demonstrates that the fringe visibility behavior fully satisfies theoretical expectations for each source type, consistent with prior discussion:

- For the high-spatial-coherence source (no diffuser), the average fringe visibility values remain consistently high, approaching the maximum ($\nu \approx 1$). This aligns with expectations for an ideal coherent source where light waves maintain stable phase relationships, maximizing interference contrast.

- Results for the pseudo-thermal source (stationary diffuser) show random, erratic visibility distributions without predictable displacement dependence. This directly manifests the static speckle pattern generated by the stationary diffuser. Since each measurement corresponds to a single instantaneous realization of the fluctuating optical field without temporal or ensemble averaging, the visibility at specific slit positions varies drastically according to local speckle intensity and phase. This interpretation is strongly supported

by high dispersion values calculated for each recorded image during slit displacement, confirming the random and unpredictable nature of individual speckle realizations.

- For the controllable-coherence source (rotating diffuser), visibility exhibits remarkably stable behavior throughout displacement. This stability characterizes Schell-Gauss-type sources where the complex spatial coherence degree depends solely on point separation, not absolute position. Moreover, this configuration shows the lowest dispersion values in the experiment, even compared to the high-coherence source. This empirical result is crucial and explained by the ensemble-averaging inherent to diffuser rotation. By averaging multiple random field realizations, speckle noise is significantly mitigated, enabling more robust measurement of the underlying spatial coherence statistics. This behavior perfectly matches expectations for Schell-Gauss sources and validates their implementation as controllable, statistically stable spatial coherence sources.

For double-slit D, the results illustrated in Fig. **4-13** were obtained:

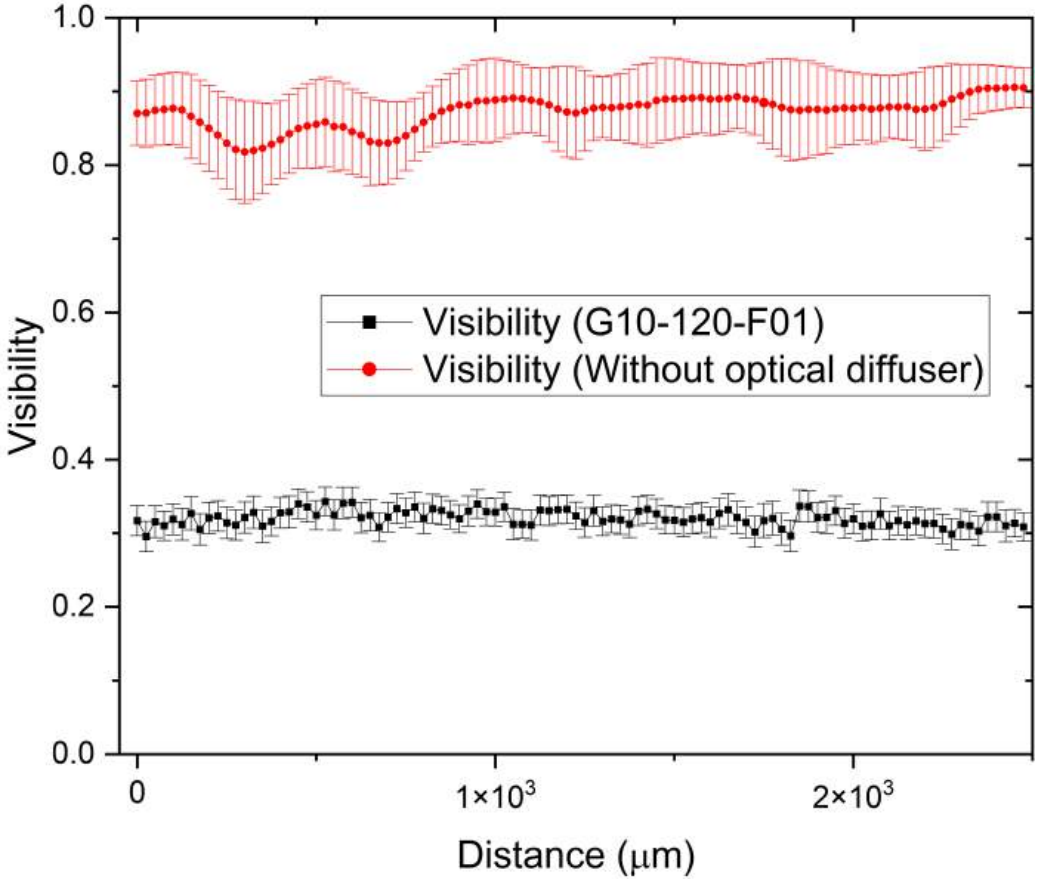

Figure 4-13: Visibility versus displacement for slit D with DG10-120-F01 diffuser disk rotating at approximately 0.314 m/s and without diffuser.

Fig. 4-13 shows general fringe visibility behavior similar to slit C for both source configurations. Specifically:

- For the high-spatial-coherence source (no diffuser), average fringe visibility remains consistently high ($\nu \approx 1$), as expected when stable phase relationships maximize interference contrast.
- For the controllable-coherence source (rotating diffuser), visibility shows characteristically stable behavior with low dispersion during displacement. This pattern is distinctive of Schell-Gauss sources where the complex spatial coherence degree is spatially homogeneous, and field statistics stabilize through ensemble averaging during diffuser rotation. However, a key difference emerges between slits D and C for the Schell-Gauss source: the average visibility is consistently lower for slit D. This behavior is directly attributable to visibility's dependence on slit separation in Young experiment. For partially coherent sources like Schell-Gauss models, the magnitude of the complex spatial coherence degree (equivalent to visibility for equal slit intensities) decreases with increasing transverse separation between observation points. Given that slit C separation is smaller than slit D (as previously indicated), the higher average visibility for slit C constitutes an expected and coherent result.

In summary, the results for double-slit D, both in their general behavior and visibility differences compared to slit C, are fully consistent with theoretical expectations for sources with different coherence states. They validate the relationship between system geometry and the manifestation of the spatial coherence degree.

4.4 Autofocus Metrics

Section 2.4 presented the theoretical framework for the implemented autofocus metrics. The core objectives of applying these metrics to experimental analysis are summarized below, crucial for evaluating optical system performance with controlled illumination sources:

Identification of optimal focal planes: The primary objective is to precisely determine optimal focal planes for each experimental configuration. This computational identification of diffraction distances (z-distance) is essential for the faithful reconstruction of complex light fields in lensless systems such as holographic microscopes.

Quantifying spatial coherence effects on focusing accuracy: We quantify how variations in the spatial coherence degree of illumination sources influence the reliability and precision of focal plane determination. This analysis is vital since partially coherent sources (e.g., LEDs, LDs) commonly used in compact, low-cost devices exhibit distinct behaviors in autofocus algorithms compared to highly coherent sources. Spatial coherence directly

modulates interference pattern formation (fringe visibility) and coherent noise reduction (e.g., speckle suppression), thereby impacting the robustness and accuracy of focus metrics.

Various autofocus metrics were implemented, categorized by the image properties they quantify. The metrics implemented were the local contrast metric, the intensity variance metric, the gradient metric, and the entropy metric; these were described in section 2.4.

To enable comparative analysis of autofocus metrics and evaluate their sensitivity and robustness in identifying optimal focal planes, all metric outputs were normalized. This normalization established a unified scale to:

Characterize metric response profiles: Assessing how each autofocus function varies with axial displacement (z-distance), critical for evaluating its capacity to identify a unique focus peak (or valley).

Determine inter-metric consistency: Verifying convergence of different metrics toward identical focal planes. Agreement among metrics serves as a key reliability indicator for autofocus performance across experimental configurations, particularly important given the established influence of spatial coherence on autofocus algorithm precision.

The experimental configuration positioned the sample (24 ± 0.05) mm from the sensor, with (230 ± 0.57) mm between the source and sensor. Camera exposure time was fixed at 5 ms. A DG10-120-F01 rotating diffuser disk was implemented at 0.38013 m/s. Normalized metric outputs are shown in Fig. **4-14**.

Two primary observations emerge from the normalized autofocus metrics in Fig. **4-14**: First, nearly all metrics exhibit maxima at the origin (except entropy, minimized at focus). This artifact is attributed to microscopic particulates or dust motes on the sensor surface (evident in Fig. **4-15** a), which generate spurious focus peaks at $\mathbf{z \approx 0}$ due to direct in-plane focusing. Second, gradient-based and local contrast metrics reveal sample focusing at a distinct plane, showing a prominent local maximum at $2.24 \times 10^4 \mu m$. This measured focal distance shows minimal deviation from the expected $2.4 \times 10^4 \mu m$ sample position, demonstrating strong consistency with the experimental setup despite positioning challenges inherent to the vertical configuration.

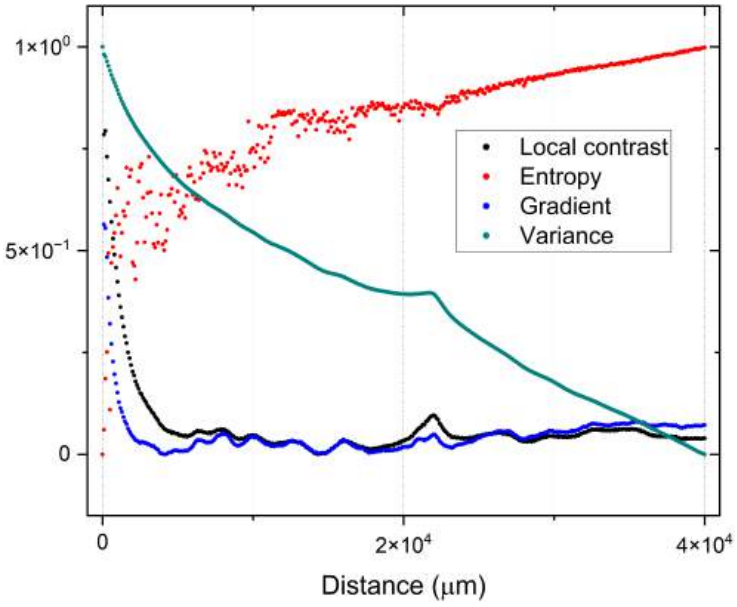

Figure 4-14: Normalized metrics with DG10-120-F01 diffuser disk at 0.38013 m/s.

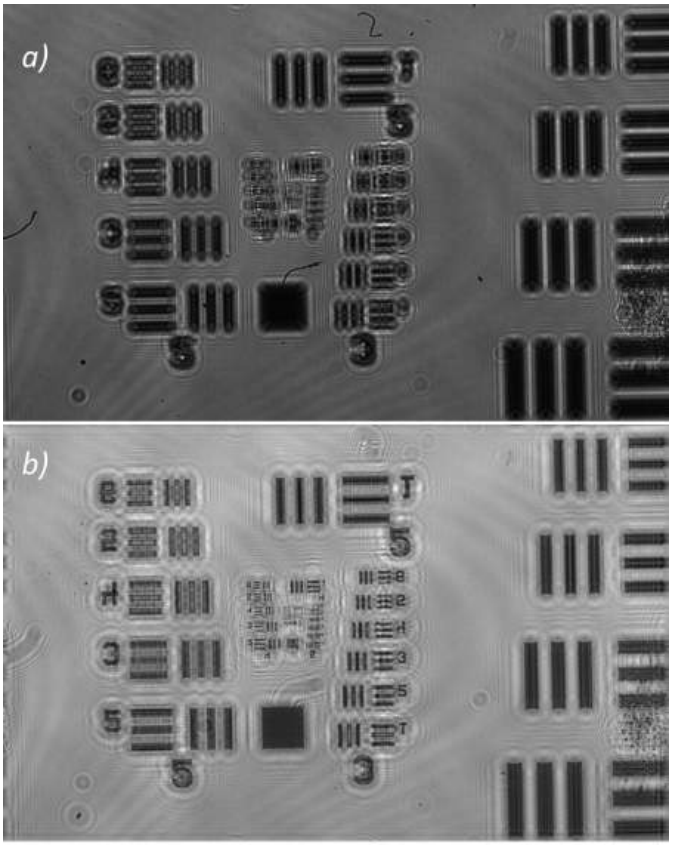

Figure 4-15: Reconstructed amplitude of the complex optical field at a) $0\mu m$. b) $2.24 \times 10^4 \mu m$.

Having validated the metrics, we now investigate how spatial coherence manipulation affects autofocus metric behavior.

For the subsequent experiment, key parameters were held constant to ensure rigorous control of illumination and acquisition conditions. These included the camera exposure time, physical configuration of the diffuser disk, and precise distances between the sensor and the U.S.A.F. 1951 calibration target. Measurements started with the stationary diffuser disk (0 m/s velocity), establishing a high-coherence baseline. Systematic measurements then followed with linear disk velocities incrementally increased from 0 to 0.2618 m/s in controlled 0.052 m/s steps. This velocity modulation strategy enabled precise control of the illumination's spatial coherence degree - a crucial factor for evaluating speckle noise reduction and image quality enhancement in the holographic system. Metric calculations were performed at $z = 100\mu m$ intervals.

Results for the variance metric are shown below:

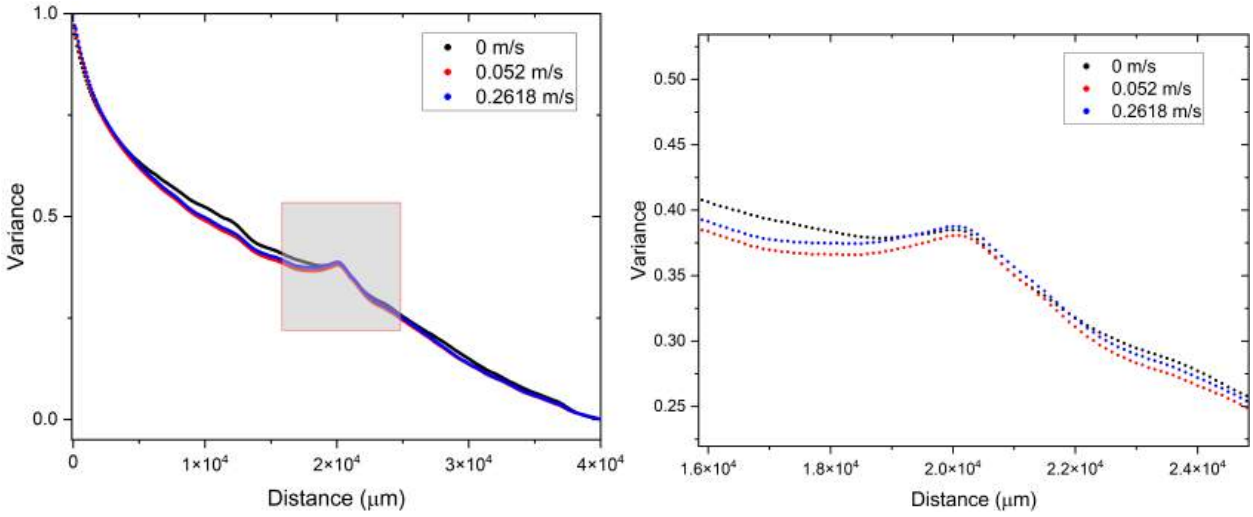

(a) (b)

Figure 4-16: (a) Intensity variance metric at different rotation velocities of DG10-120-F01 diffuser disk. (b) Region of interest detail.

Fig. 4.16(b) demonstrates that increasing diffuser rotation velocity sharpens the best-focus plane region. This directly results from effective speckle noise suppression, which enhances image quality through improved contrast and signal-to-noise ratio (SNR) in holographic reconstructions. Consequently, the variance metric - intrinsically sensitive to image sharpness and contrast - identifies and characterizes the optimal focal plane with greater precision and reliability as the illumination's spatial coherence decreases. This enables more defined best-focus determination, essential for obtaining clear images and robust autofocus in lensless microscopy systems.

Results for the local contrast metric are presented below:

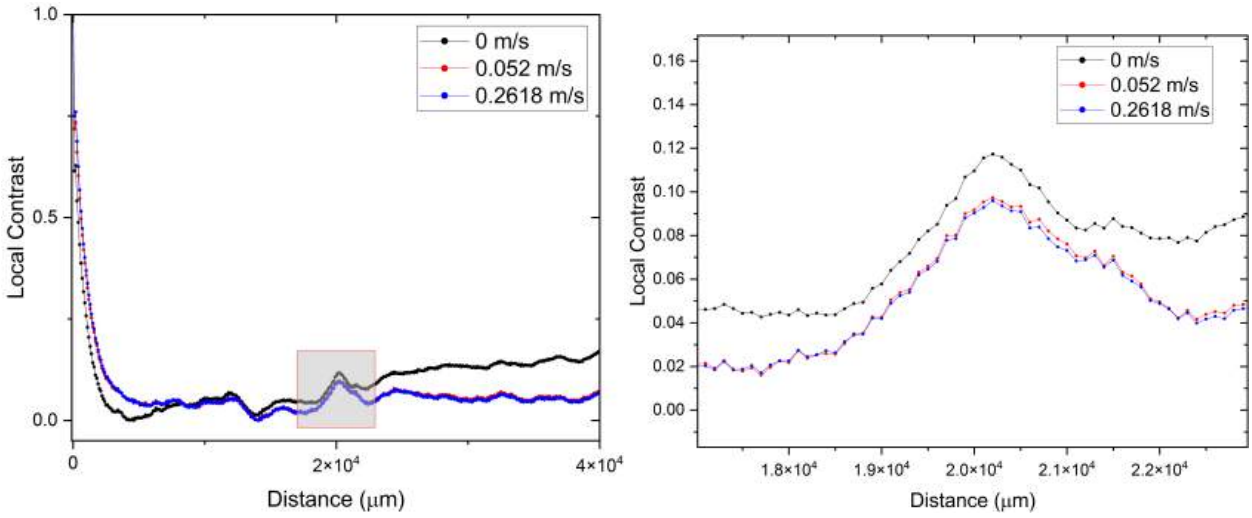

(a) (b)

Figure 4-17: (a) Local contrast metric at different rotation velocities of DG10-120-F01 diffuser disk. (b) Region of interest detail.

Fig. 4.17(a) and 4.17(b) reveal analogous behavior to the variance metric regarding focal plane resolution. For pseudo-thermal sources, the local contrast metric loses discrimination with axial distance, evidenced by increasing off-focus values in Fig. 4.17(a). This reduced focal discrimination stems from inherent speckle noise under partial spatial coherence, which diminishes effective image contrast and obscures the true focal plane. However, increasing diffuser rotation velocity improves speckle suppression, enabling more efficient and precise identification of the best-focus plane even at extended axial distances by reducing coherent noise that otherwise masks object contrast.

Similar behavior appears in the gradient metric Fig. 4.18(a), which also benefits from increased rotation velocity for focal plane definition. However, this metric exhibits greater sensitivity to high-frequency fluctuations and image components. While these fluctuations regularize with increasing calculation plane distance, post-focus values remain persistently elevated, suggesting susceptibility to residual artifacts or high-frequency coherent noise that persists despite speckle suppression.

Conversely, the entropy metric Fig. 4.18(b) shows neither consistent results nor clear trends comparable to other focus metrics. This suggests that entropy - quantifying global randomness or disorder in image intensity distribution - fails as an effective metric for precise best-focus determination in this experimental configuration. Its fundamental nature appears uncorrelated with focal sharpness when imaging complex dynamic patterns generated by speckle in pseudo-thermal sources, even under partial suppression.

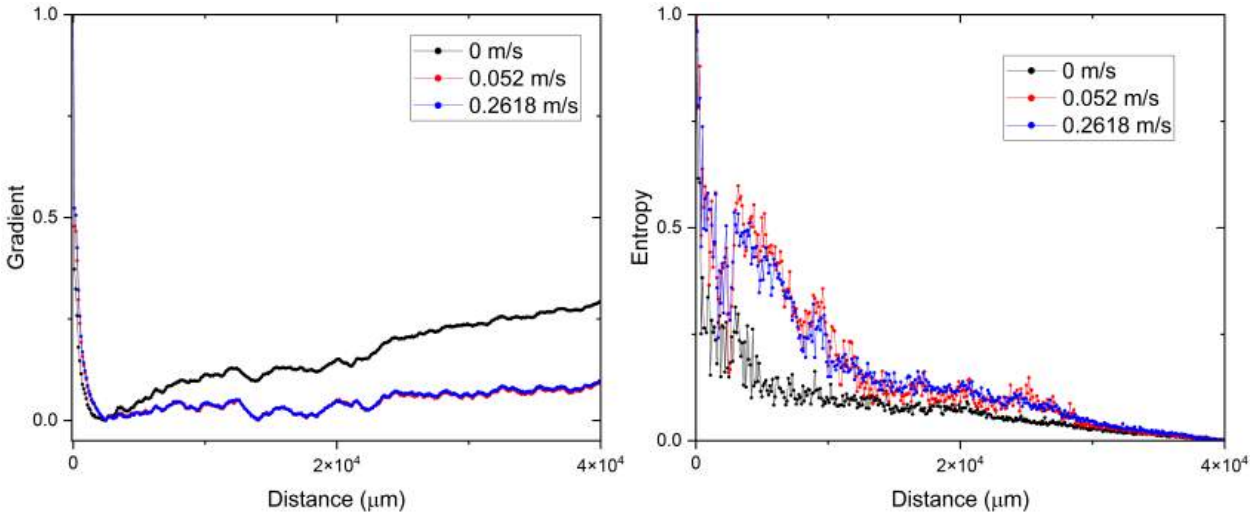

Figure 4-18: (a) Gradient metric at different rotation velocities of DG10-120-F01 diffuser disk. (b) Entropy metric.

Additional tests employed modified samples to evaluate spatial coherence impact on resolving objects with distinct optical properties. Reference polystyrene microspheres (REDPMS-098) with average diameters of 53-63 μm were used. Unlike the amplitude-modulating USAF 1951 target where dark regions absorb/block light and transparent zones permit full transmission, these microspheres primarily function as phase objects, modifying the light wave phase rather than amplitude.

Microspheres were mounted on a 0.16 mm-thick cover glass positioned approximately 2 cm from the illumination source. System parameters remained constant while diffuser rotation velocity varied systematically from 0.1885 m/s to 0.3770 m/s.

This study focused on observing morphology and resolution in reconstructed objects under different spatial coherence conditions, rather than quantitative phase recovery. Specific refractive indices are not presented since visibility was evaluated through resulting amplitude information. Crucially, the red microspheres were illuminated with green light ($\sim$532 nm). Being complementary colors, the spheres pigments absorbed green photons, causing detectable amplitude reduction in transmitted/reflected waves due to energy loss. This absorption-induced contrast enables clear morphological discrimination in amplitude reconstructions despite their primary phase-object nature.

Autofocus metric results for polystyrene microspheres are summarized in Fig. **4-19**:

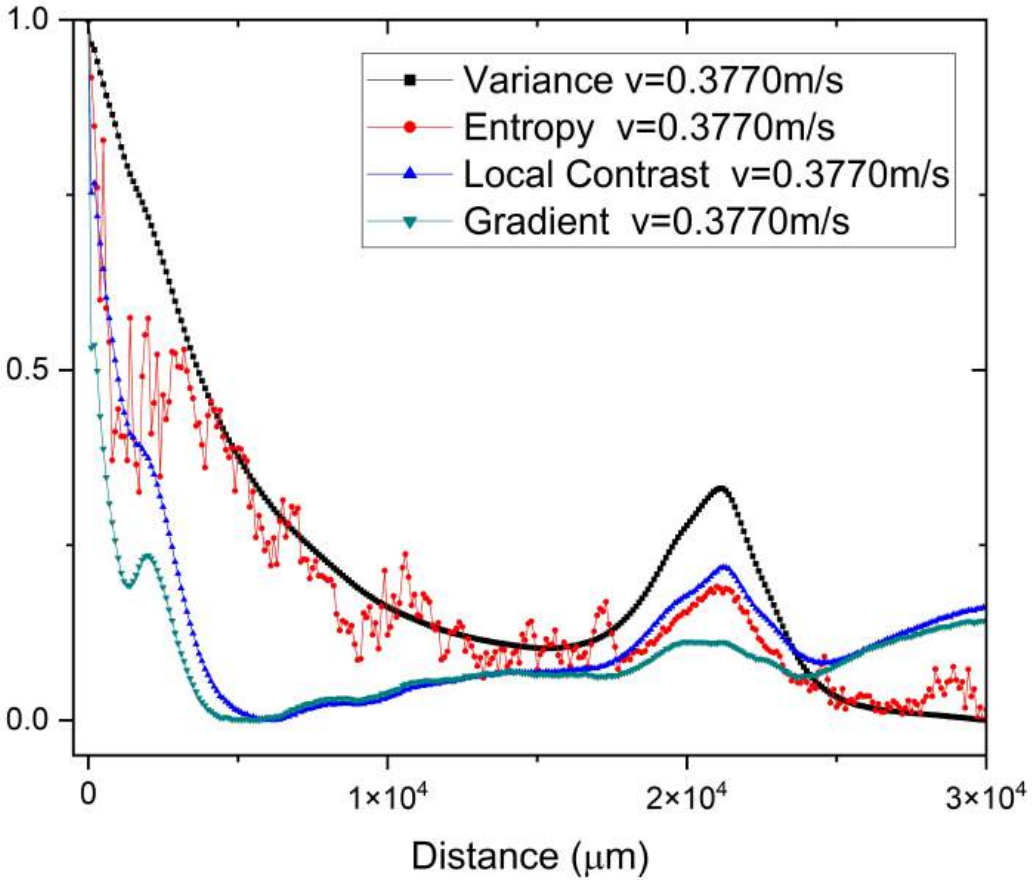

Figure 4-19: Autofocus metrics applied to polystyrene microsphere study

Fig. **4-19** shows all four metrics successfully identified the best-focus plane, a significant finding particularly for entropy. Unlike previous amplitude-object experiments (e.g., USAF 1951 target) where entropy proved ineffective, its success here stems from the microspheres properties. Though primarily phase objects, their red pigmentation under ∼550 nm green illumination causes incident light absorption, introducing detectable amplitude modulations in transmitted/reflected waves. These modulations create intensity distribution variations that entropy - quantifying image randomness - can now correlate with focal position. However, entropy exhibits pronounced variations away from focus, reflecting its inherent sensitivity to randomness and noise in severely defocused images or residual speckle.

Conversely, intensity variance and local contrast metrics demonstrate superior focal-plane determination precision. This aligns with prior observations since both metrics are highly sensitive to image sharpness, edges, and contrast. Effective speckle noise suppression via temporal averaging through diffuser rotation dramatically improves SNR and contrast, enabling robust focus identification. The reliable ensemble-averaged properties provided by the Schell-Gauss source are crucial for measurement stability.
Intensity variance metric results are shown in **4-20**.

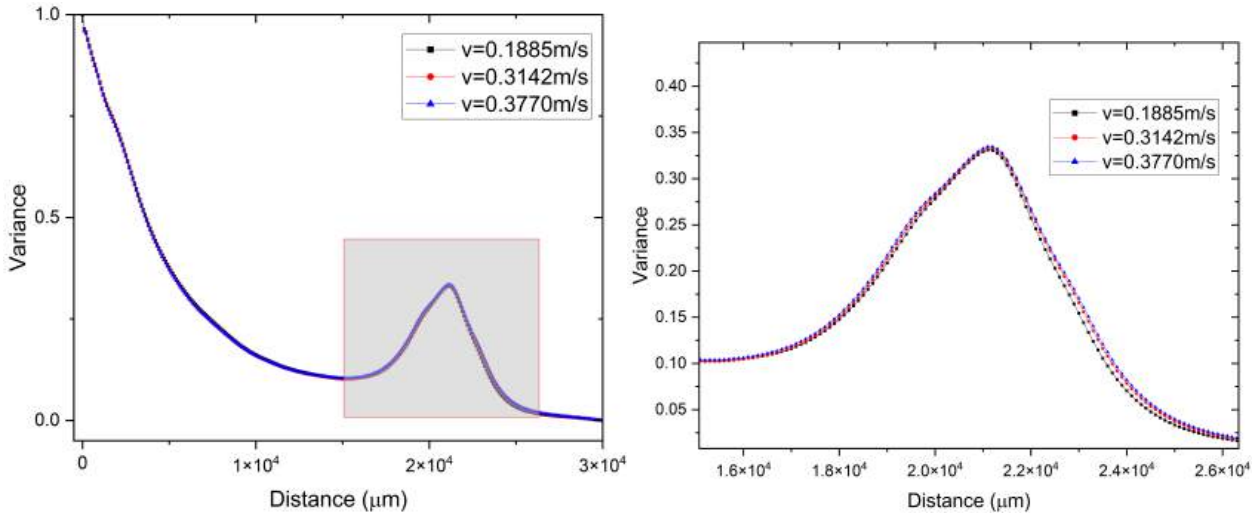

Figure 4-20: (a) Intensity variance metric at different rotation velocities of DG10-120-F01 diffuser disk. (b) Region of interest detail.

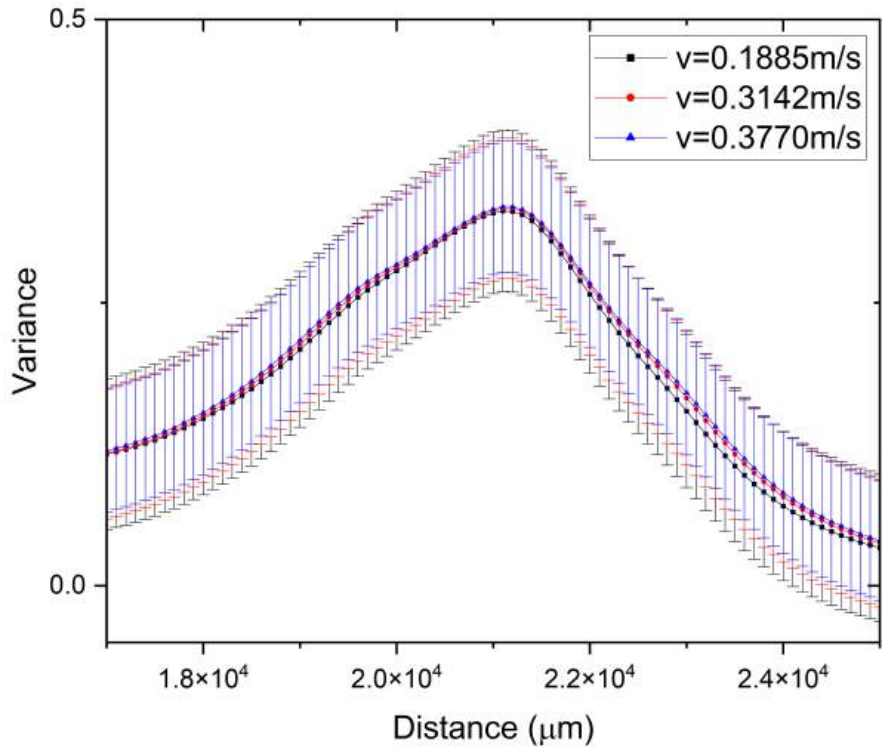

Figure 4-21: Intensity variance metric with associated uncertainties at different rotation velocities

Near the diffuser's maximum rotation velocity (∼0.380 m/s), intensity variance behavior converges across reported speeds. This occurs because maximal achievable speckle suppression

via temporal averaging has been attained - further velocity increases produce negligible changes in averaged intensity patterns. When plotting metric uncertainties (Fig. **4-21**), a crucial phenomenon emerges: uncertainties progressively decrease with higher rotation velocities. This directly results from effective temporal averaging of speckle noise.

Diffuser rotation integrates more spatially independent speckle realizations within the sensor exposure time. Theoretically, speckle contrast decreases inversely with the square root of averaged independent realizations, significantly reducing intensity signal variability. [45] This enables reliable ensemble-averaged property extraction from the generated Schell-Gauss field, essential for statistical optics.

This uncertainty reduction and stability enhancement mirrors findings in Section 2.3.2 for Schell-Gauss sources. There, lower coefficients of variation (CV) in Young's experiment fringe visibility measurements indicated greater data stability and reliability, demonstrating how controlled spatial coherence and speckle suppression enable precise metrology. Reducing uncertainties to achieve stable measurements constitutes a critical factor for reliability in lensless microscopy applications.

Comparative tests evaluated image quality metric behavior against two fundamental numerical propagation methods in lensless holographic microscopy: Fresnel propagation and angular spectrum propagation. These trials assessed reconstruction consistency and numerical precision. Results demonstrated that under our experimental conditions, both methods yield virtually identical metric behavior, with minimal differences appearing only in the least significant decimal digits.

For instance, at a focusing distance of 2.05 $\times 10^4 \mu$m, the intensity variance metric (identified as optimal for best-focus determination in our setup) yielded values of 0.40497 (Fresnel) and 0.40492 (Angular Spectrum). For the local contrast metric (second-best performer), values at the same plane were 0.10357 (Fresnel) and 0.10302 (Angular Spectrum) (see Fig. 4.22(a), 4.22(b), 4.23(a), 4.23(b)). These fourth-decimal-place differences for variance and third-decimal-place differences for local contrast are numerically insignificant, indicating strong agreement.

This close similarity aligns with literature predictions for specific operational regimes. While the Angular Spectrum method is recognized as an exact solution to the Rayleigh-Sommerfeld diffraction problem (valid even at short propagation distances), Fresnel propagation constitutes a paraxial approximation. However, when propagation distances and apertures satisfy Fresnel approximation validity conditions (i.e., for low to moderate Fresnel numbers) or when numerical implementations are optimized - such as the SDD approach maintaining a constant field-of-view for microscopic objects in Angular Spectrum propagation - both methods can produce nearly identical numerical results. The observed minimal differences confirm reconstruction robustness under this study's conditions and suggest practical method

interchangeability, which is fundamental for measurement reliability in lensless microscopy applications.

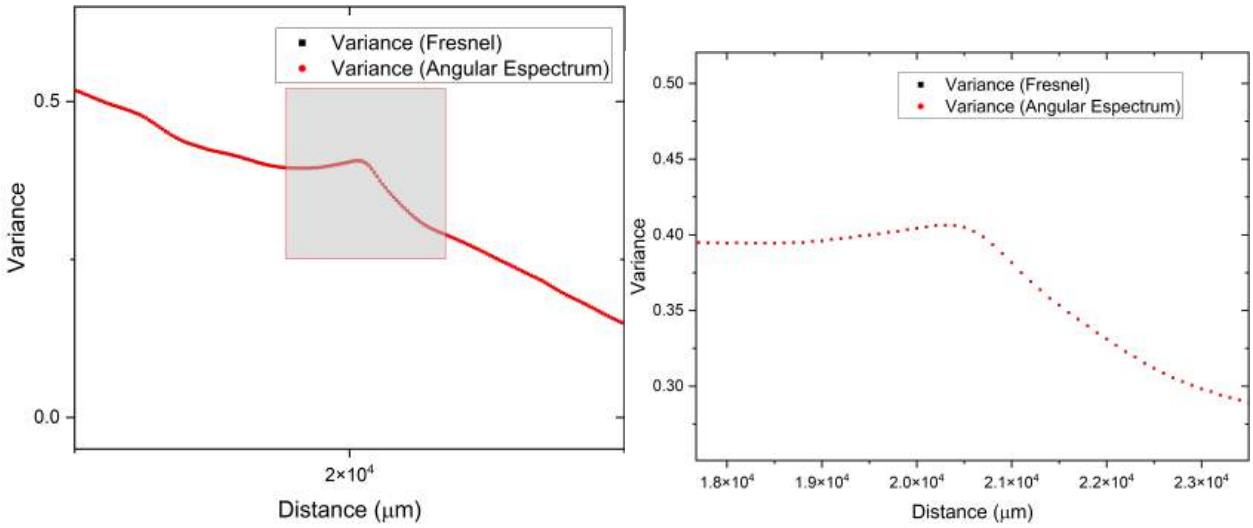

(a) (b)

Figure 4-22: (a) Intensity variance metric calculated via Fresnel and Angular Spectrum propagation methods. (b) Region of interest detail.

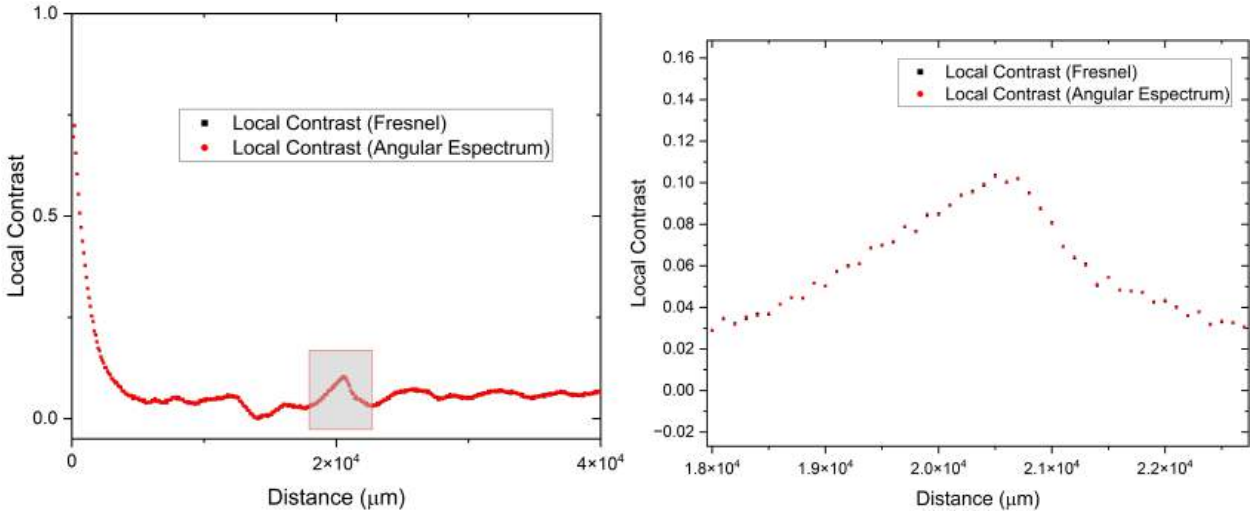

(a) (b)

Figure 4-23: (a) Local contrast metric calculated via Fresnel and Angular Spectrum propagation methods. (b) Region of interest detail.

4.5 Effects of Spatial Coherence

Analysis of intensity profiles in amplitude reconstructions at the best-focus plane (Section 2.5), Fig. **4-28** revealed significant improvements in contrast and resolution as functions of diffuser disk rotation velocity.

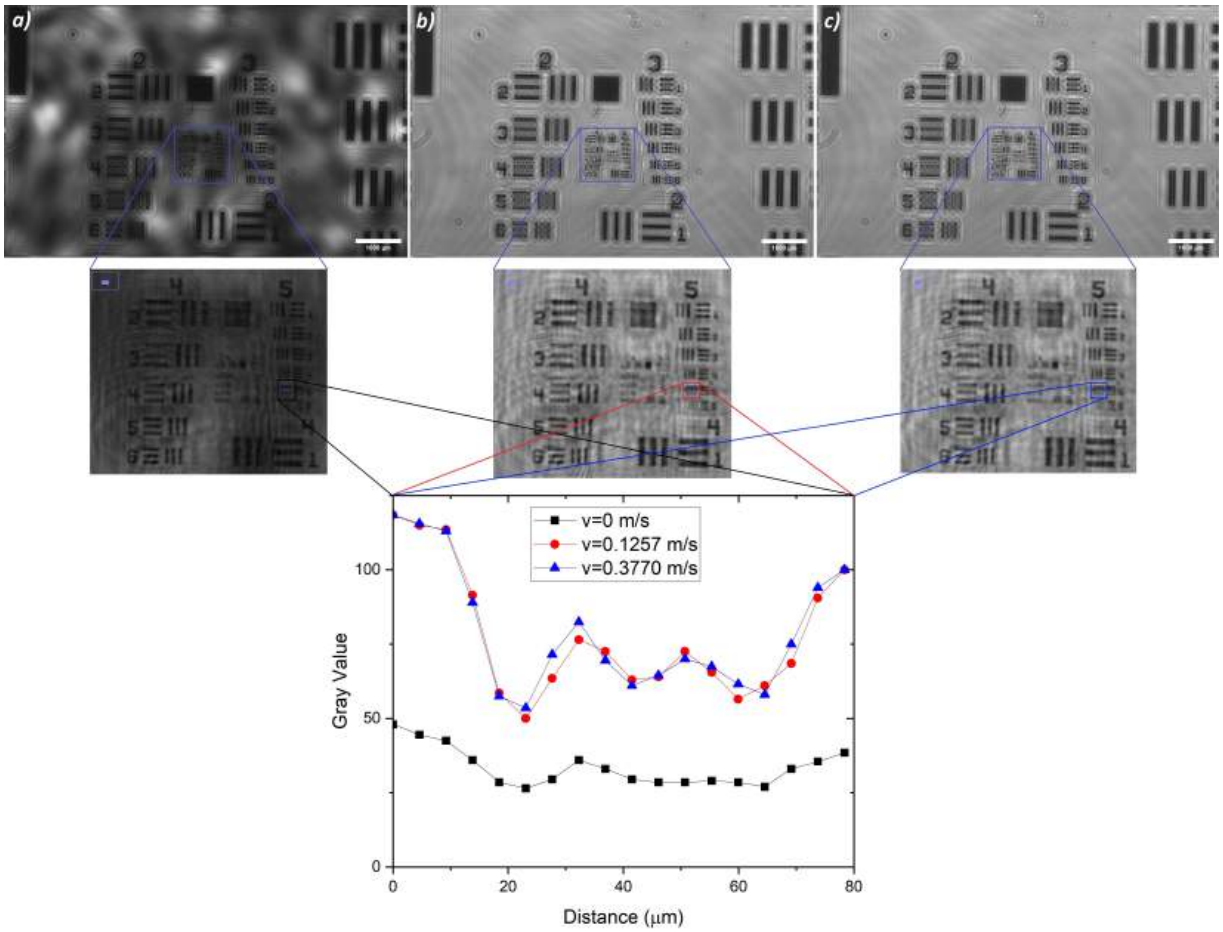

Figure 4-24: Reconstructed complex optical field amplitude at velocities: a) 0 m/s, b) 0.1257 m/s, c) 0.3770 m/s

For the stationary diffuser (0 m/s), the dynamic intensity range was considerably compressed (grayscale: 26.5-48). Rotation at 0.1257 m/s and 0.3770 m/s expanded this range to 50 - 118.5 grayscale units. This contrast enhancement directly results from speckle reduction, where temporal averaging of spatially independent speckle patterns during sensor exposure converts coherent speckle noise into incoherent noise. This process increases the signal-to-noise ratio (SNR) of recorded holograms and reconstructed images - a key benefit of partially coherent illumination in lensless holographic systems.

Image quality enhancement directly improved the system's resolution limit from 22.09±0.08μm

(stationary diffuser) to $17.59 \pm 0.06\mu$m (speckle-reduced conditions). This aligns with theoretical expectations in lensless holographic microscopy, where reduced coherent noise facilitates fine detail discrimination. The result underscores coherence management's importance for high-resolution imaging in such configurations.

A final experimental configuration employed an IDS U3-36P2XLS-M Rev.1.2 image sensor (20 MP resolution, 1.4 μm pixel size, 10-bit depth). Exposure time remained fixed at 5 ms (operational range: 0.017-1144 ms) for consistency. A USAF resolution target was positioned approximately 7 cm from the sensor.
Intensity variance metric results (Fig. **4-25**) previously identified as optimal for focus determination revealed significant findings. The zoomed view (Fig. 4.25(b)) shows a notably sharper peak near best focus under controllable spatial coherence versus high spatial coherence (H.S.C.) or stationary diffuser conditions.
This variance peak sharpness robustly indicates optimized focus detection and substantial image quality improvement. Effective speckle reduction drives this result: speckle constitutes coherent noise inherent to laser illumination, manifesting as granular interference patterns that degrade contrast and resolution. Thus, variance metric enhancement confirms speckle mitigation is essential for high-fidelity reconstructions and precise focus determination in lensless microscopy.

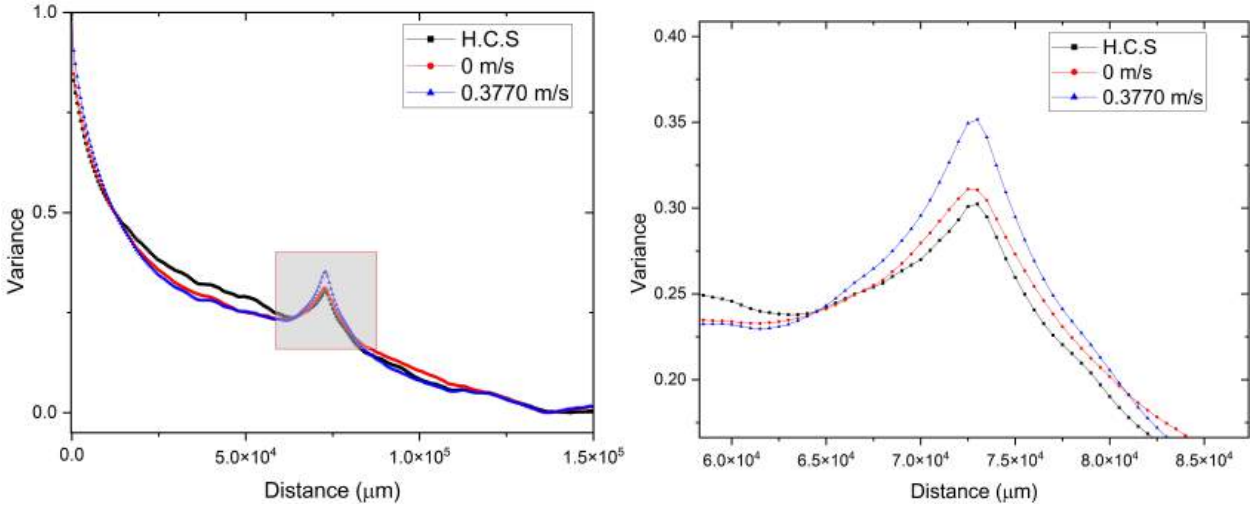

(a) (b)

Figure 4-25: (a) Intensity variance metric via Fresnel propagation. High Spatial Coherence source (H.S.C). (b) Region of interest detail.

Local contrast metric results reinforce image quality consistency, showing harmonic behavior with variance observations. Fig. 4.26(b) demonstrates sharper peaks coinciding with the variance-identified focus plane. This contrast enhancement directly manifests effective speckle

suppression under controllable coherence. The variance-contrast correlation robustly indicates autofocus reliability and system effectiveness in artifact removal. Enhanced local contrast facilitates fine detail discrimination - crucial for resolving USAF targets - confirming spatial coherence management's positive impact on quantitative reconstruction quality.

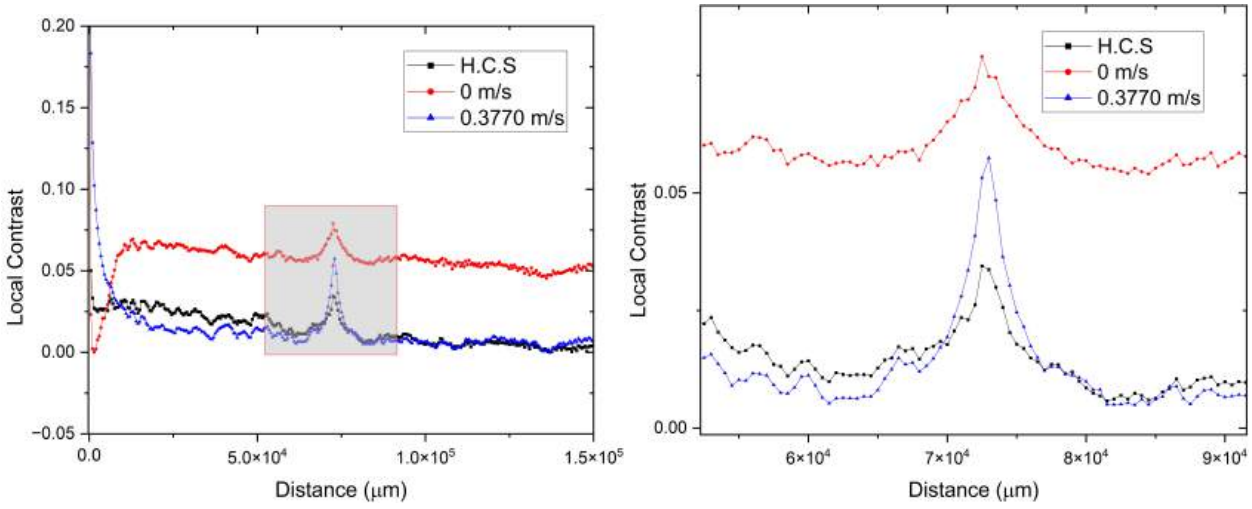

(a) (b)

Figure 4-26: (a) Local contrast metric via Fresnel propagation. H.S.C.: high spatial coherence source. (b) Region of interest detail.

This 20 MP configuration (pixel size: 1.4 μm vs. prior 4.8 μm; sample distance: $\sim$7 cm) significantly improved metric performance. Entropy results (Fig. 4.27(b)) showed superior behavior versus the 2.3 MP setup. This enhancement stems from the sensor's capacity to capture finer details: entropy quantifying intensity distribution randomness develops sharper peaks at maximum sharpness due to higher pixel density, enabling precise focus discrimination.

The gradient metric (Fig. 4.27(a)) effectively identified the focus region but exhibited lower precision than variance and contrast metrics. This may arise from the gradient's heightened sensitivity to noise or inherent edge-definition characteristics, causing focus determination fluctuations despite correct region identification.

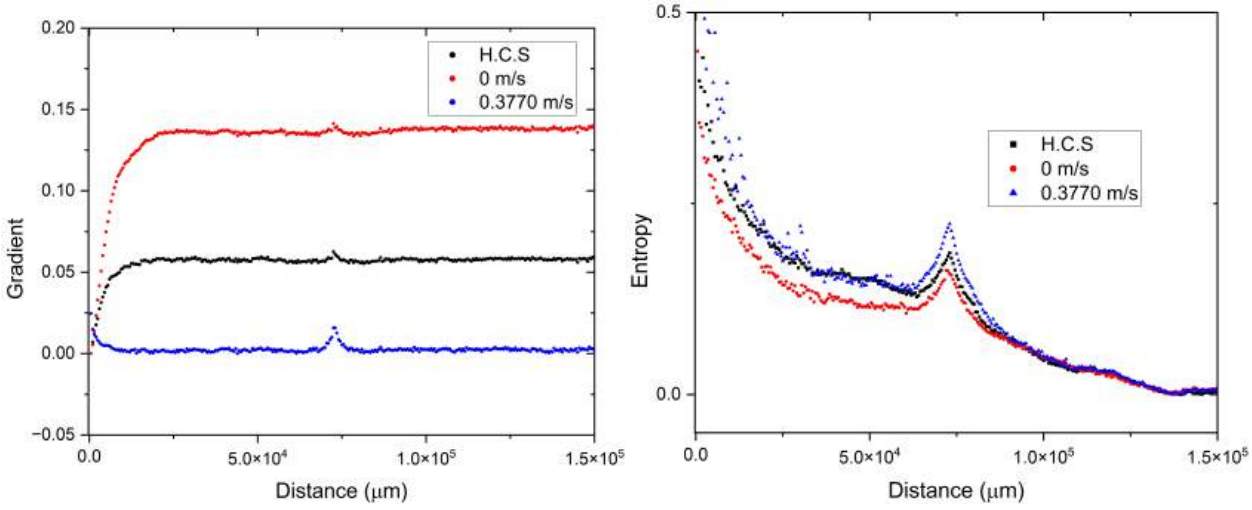

(a) Gradient metric (b) Entropy metric

Figure 4-27: Metrics for high spatial coherence source (H.S.C), stationary diffuser, and diffuser at ∼0.3770 m/s.

Plots for both metrics (Fig. 4-27) reconfirm controllable spatial coherence's impact on image quality.

To evaluate system performance with the 20 MP sensor configuration, resolution analysis followed the methodology previously established for the 2.3 MP camera. Characterized by a 1.4 μm pixel size, the 20 MP sensor inherently enables higher potential resolution. The reconstructed complex optical field amplitude at the USAF target's best-focus plane appears in Fig. 4-28.

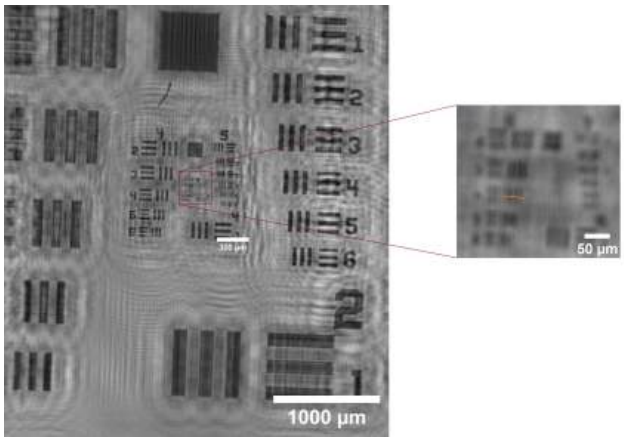

Figure 4-28: Reconstructed complex optical field amplitude at best-focus plane for USAF target

Resolution limit analysis revealed significant spatial coherence effects. Using a Schell-Gauss

source (S.G.S.), the system resolved element 5 of group 6 on the USAF target, corresponding to a resolution limit of $9.8 \pm 0.5 \mu m$. With a high spatial coherence source (H.C.S.), resolution only reached element 4 of group 6 ($11.0 \pm 0.4 \mu m$). These findings are evident in the intensity profile shown in Fig. 4-29.

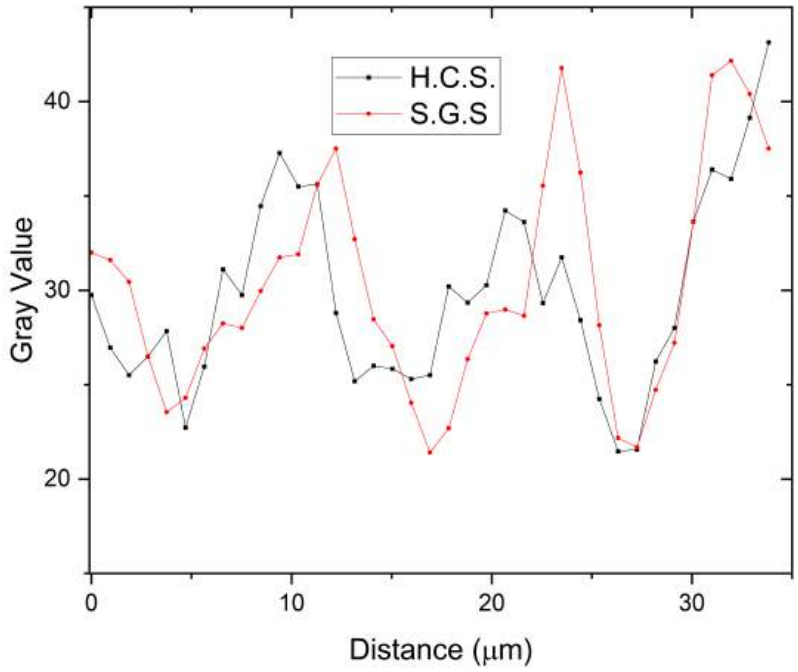

Figure 4-29: Intensity profile over element 4, group 6 of USAF target corresponding to Figure 4-28.

The resolution improvement from 11.0 μm (H.C.S.) to 9.8 μm (S.G.S.) despite high spatial coherence sources theoretically offering superior point spread function (PSF) behavior directly results from effective speckle suppression via the Schell-Gauss source's controllable spatial coherence. As discussed in prior variance and local contrast metric analyses, this speckle reduction enhances contrast and clarity, enabling finer feature discrimination essential for precise resolution limit determination in USAF patterns.
Furthermore, spatial coherence control through Schell-Gauss sources not only improves resolution but reduces high-coherence distortions. Lensless system resolution capability depends on factors including sensor pixel size and effective magnification. Here, combining a higher-resolution sensor (20 MP with 1.4 μm pixels) with optimized source coherence management achieves superior resolution limits.

A test verified metric capability to detect objects at different depth planes. Recordings of microspheres positioned at distinct planes are shown in Fig. 4-30 and Fig.4-31.
A critical finding, evident when comparing results from Fig. 4-30 and Fig. 4-31 with the amplitude reconstruction in Fig. 4-1, is the significant enhancement in suppressing

diffraction artifacts generated by microspheres. This optimization is directly attributed to the implementation of a 20 MP camera featuring substantially smaller pixels (1.4 μm), compared to the previous 2.3 MP camera with 4.8 μm pixels.

Pixel size reduction is critical as it enables denser and more precise sampling of high spatial frequencies present in diffraction patterns and complex interference fringes produced by microspheres. [8] In lensless microscopy, achievable lateral resolution is intrinsically tied to sensor pixel size. Smaller pixels permit the sensor to capture finer details and rapid oscillations of the holographic field – essential for avoiding aliasing and reconstructed image distortions. [42]

Furthermore, the higher megapixel count (20 MP) translates to either increased detection area or superior sampling density. This enhances the system's capacity to record complete diffraction patterns from objects, particularly those exhibiting wide-angle light scattering. Through denser sampling over an extended area, the effective numerical aperture (NA) of the detection system is increased. This improved sampling enables reconstruction algorithms to generate images with enhanced detail and significant reduction of artifacts such as diffraction rings and coherent background noise [20]. Consequently, superior high-frequency sampling yields more faithful object representation, mitigating undesirable diffraction effects while improving overall reconstruction quality.

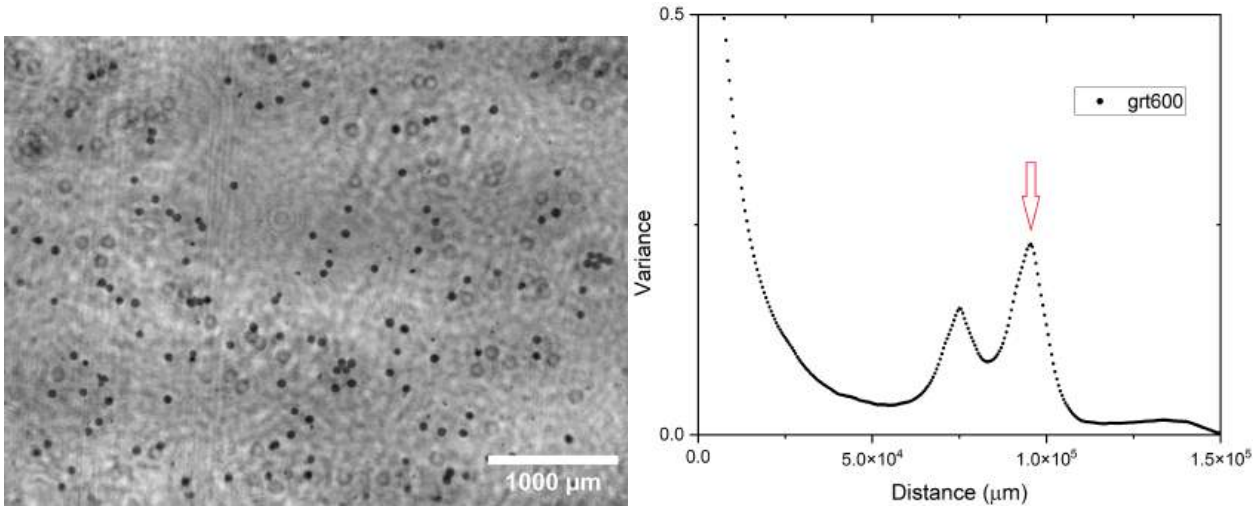

(a) (b)

Figure 4-30: (a) Amplitude reconstruction at 9.55 $\times 10^4 \mu$m. (b) Best-focus plane determination via intensity variance metric.

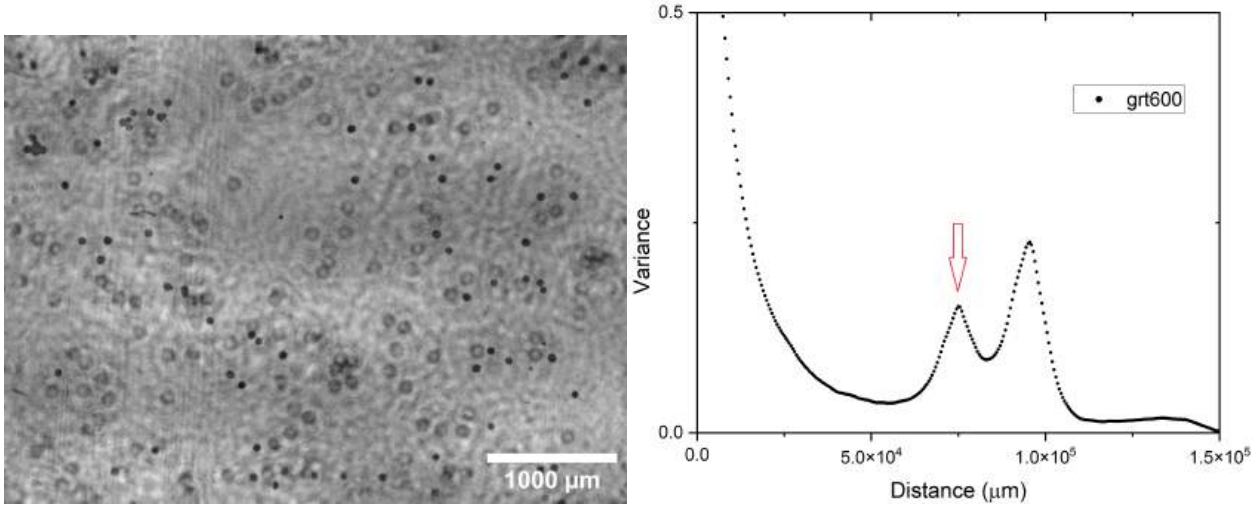

(a) (b)

Figure 4-31: (a) Amplitude reconstruction at 7.55 $\times 10^4 \mu$m. (b) Best-focus plane determination via intensity variance metric.

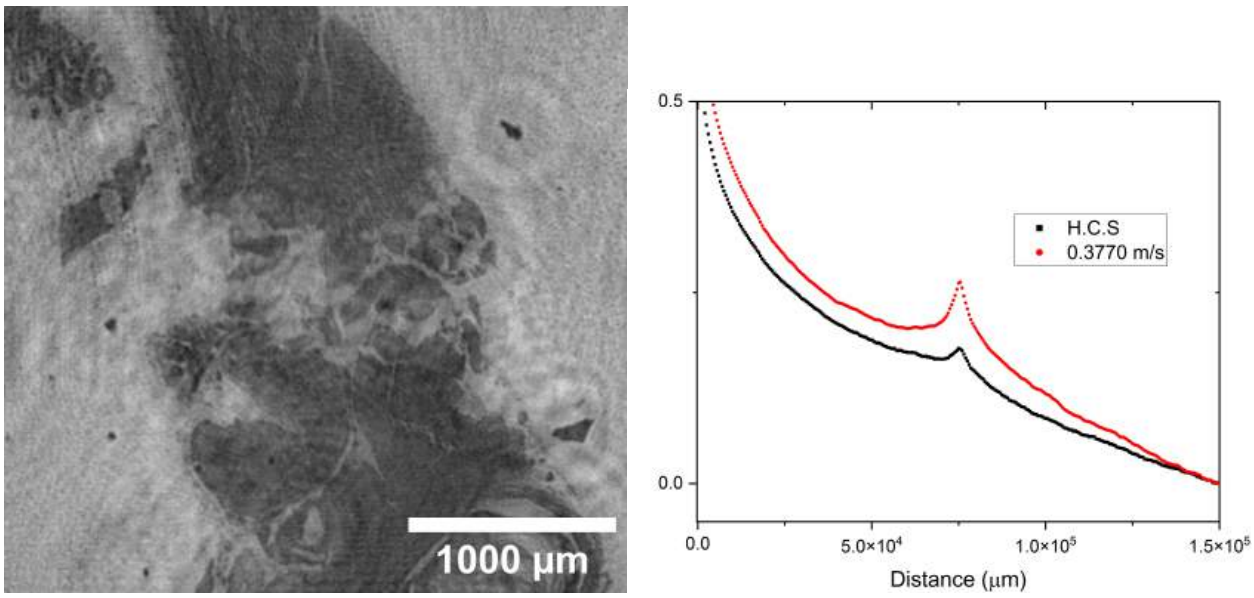

(a) (b)

Figure 4-32: (a) Amplitude reconstruction at 7.55 $\times 10^4 \mu$m for biological tissue sample. (b) Best-focus plane determination via intensity variance metric.

Comprehensive tests were conducted on biological samples, such as the tissue shown in Fig. 4.32(a), to evaluate focus metric performance when imaging inherently complex biological structures. Lensless microscopy offers significant advantages for such samples - wide field-of-view, low cost, and label-free imaging capability. However, reconstructing complex and

potentially transparent objects like cells or tissues requires careful coherence management to achieve clear, precise results.

Metric performance proved notably more efficient when using Schell-Gauss sources (partial coherence) compared to high spatial coherence sources. Fig. 4.32(b) demonstrates that even for intricate biological structures, controlled spatial coherence implementation significantly enhances metric precision in determining the optimal focus plane.

Chapter 5

Conclusions

A pseudo-thermal Schell-Gaussian illumination source was successfully implemented and characterized using a laser and rotating optical diffuser disk. Experimental results demonstrated that diffuser rotation velocity drastically reduces speckle contrast through temporal averaging of coherent noise patterns. This process transforms the speckle intensity distribution from exponential (static diffuser) to Gaussian - indicating improved uniformity and effective coherent noise suppression. Schell-Gauss behavior was verified via Young's double-slit experiment, where interference fringe visibility remained constant regardless of slit displacement (for fixed separation), confirming the source's spatial coherence depends solely on point separation, not absolute position.

The Intensity Variance and Local Contrast metrics proved most efficient and precise for best-focus plane determination in our system. Both exhibited sharper, more defined peaks with increasing diffuser velocity, indicating enhanced autofocus precision through spatial coherence reduction and speckle suppression. Though initially less effective for amplitude objects (e.g., USAF target), the Entropy metric showed significantly improved performance with phase objects (polystyrene microspheres) and higher-resolution sensors. Crucially, higher rotation velocities (lower spatial coherence) reduced autofocus metric uncertainties, yielding more stable and reliable focal plane measurements. Additionally, Fresnel and Angular Spectrum propagation methods produced virtually identical autofocus results under experimental conditions, validating their robustness and applicability.

Effective speckle suppression via spatial coherence control substantially improved reconstructed object contrast and detail visibility. Resolution limits decreased from $22.09 \pm 0.08 \mu m$ (stationary diffuser) to $17.59 \pm 0.06 \mu m$ (rotating diffuser). Using a high-resolution sensor (20 MP, 1.4 μm pixels), resolution further improved from $11.0 \pm 0.4 \mu m$ (high spatial coherence source) to $9.8 \pm 0.5 \mu m$ (Schell-Gauss source). This enhancement directly stems from speckle mitigation and the sensor's enhanced ability to sample fine details and high spatial frequencies, producing a more faithful object representation.

The implemented autofocus metrics successfully detected and focused objects at different depth planes. Moreover, the system operated efficiently with complex biological samples, highlighting the promising potential of lensless digital holographic microscopy with controlled spatial coherence sources - particularly for biomedical applications.

In summary, this research confirms that controlling illumination spatial coherence can increase the resolution of the reconstructed objects, image quality, and auto-focus precision through effective speckle noise suppression - particularly notable given no super-resolution algorithms were implemented.

Appendix A

Algorithm for reconstructing complex optical fields by Fresnel propagation and angular spectrum

```
%%%%%%%%%%%%%%%%%%%%%%%%%%%%%%%%%%%%%%%%%%%%%%%%%%%%%%%%%%%%
%%%%%%%%%%%%%%%%% XXXXXXXXXXX Algorithm for reconstructing complex optical fields by Fresnel propagation and angular spectrum XXXXXXXXXXX %%%%%%%%%%%%%%%%%
%%%%%%%%%%%%%%%%%%%%%%%%%%%%%%%%%%

clc
close all
clear all



lambda=0.542;

d=1225;
L=60000;

dx=4.7;
dy=dx;
k = (2.0*pi)/lambda;

%%
ruta='D:\MAESTRIA EN CIENCIA (OPTICA)\CUATRIMESTRE 2\ PTICA   DE FOURIER\miguel\microesferas\microesferas\';
```

```
ruta1='D:\MAESTRIA EN CIENCIA (OPTICA)\CUATRIMESTRE 2\ PTICA  DE FOURIER\miguel\microesferas\microesferas\Amplitud\2\';
ruta2='D:\MAESTRIA EN CIENCIA (OPTICA)\CUATRIMESTRE 2\ PTICA  DE FOURIER\miguel\microesferas\microesferas\fase\2';
ruta3='D:\MAESTRIA EN CIENCIA (OPTICA)\CUATRIMESTRE 2\ PTICA  DE FOURIER\miguel\microesferas\microesferas\fresnel\';

h=adquisicion([ruta,'\h2.bmp']);
h0=adquisicion([ruta,'\r1.bmp']);
h1=h0-h;
h1=h;


[NX,MY]=size(h1);

tx=-NX/2:1:NX/2-1;
ty=-MY/2:1:MY/2-1;

jx=dx*tx;
jy=dy*ty;

dvx=1/(NX*dx);
dvy=1/(MY*dy);
vx=dvx*tx;
vy=dvy*ty;

Auv=fft2(h1);
Auv=fftshift(Auv);




[x,y]=meshgrid((1:NX)*dx,(1:MY)*dy);
U = sqrt(h1)*exp(-1.j*k*sqrt(x.*x+y.*y+L^2));

U1=fft2(U);
U2=fftshift(U);



[U V]=meshgrid(vy,vx);
```

```
61
62 r=exp(1i*2*pi*d*(sqrt(1-(lambda^2)*(U.*U+V.*V)))/lambda);
63 Auvexp=Auv.*r;
64
65 X=fftshift(Auvexp);
66 rec1=ifft2(X);
67 rec1=255*abs(rec1)/max(max(abs(rec1)));
68
69 figure,image(vy,vx,rec1),colormap(gray(256)),axis square;
70 set(gcf,'Color',[0.5 0.5 1],'NumberTitle','on','Name','Patr n');
71 title('\bf Propagaci n de Fresnel');
72 imwrite(rec1,colormap(gray(256)),[ruta3,'\fres_',num2str(d),'.tif'])
     ↪ ;
73
74 %%%%%%%%%%%%%%%%%%%%%%%%%%%%%%%%%%%
75
76 [x,y]=meshgrid(1:(NX),1:(MY));
77 Auv=fft2(h1);
78 Auv=fftshift(Auv);
79
80 [U V]=meshgrid(vy,vx);
81
82 r=exp(1i*2*pi*d*(sqrt(1-(lambda^2)*(U.*U+V.*V)))/lambda);
83 Auvexp=Auv.*r;
84
85 X=fftshift(Auvexp);
86 rec2=ifft2(X);
87 rec3=rec2/max(rec2(:))*256;
88 figure,imagesc(abs(rec3)),colormap(gray(256));
89 title(['Reconstruccion en amplitud 2D   ',num2str(d),'  micras']);
90 %set(gcf,'Color',[0.5 0.5 1],'NumberTitle','on','Name','Patr n');
91 title('\bf Espectro Angular');
92 fa=angle(rec2);
93 fa1 = fa+(2*pi)*(fa<0);
94 fa1=fa1/max(fa1(:))*256;
95 rec1_view=256*rec2/(max(max(rec2)));
96 figure, imagesc(fa1), axis image, colorbar, colormap(gray);
97 title(['Reconstruccion en fase 2D   ',num2str(d),'  micras']);
98 imwrite(fa1,colormap(gray(256)),[ruta2,'\fa_',num2str(d),'.tif']);
99 imwrite(mat2gray(abs(rec3)),[ruta1,'\Amp_',num2str(d),'.tif']);
```

Appendix B

Algorithm for average contrast

```
1
2  close all
3  clear all
4  clc
5
6  [filenames, pathname] = uigetfile({'*.png;*.jpg;*.bmp;*.tif', 'Image
       ↪  Files'}, ...
7                                    'Select Images', 'MultiSelect', '
                                        ↪ on');
8
9
10 if isequal(filenames, 0)
11     error('No images were selected.');
12 end
13
14
15 % Cell Array
16 if ischar(filenames)
17     filenames = {filenames};
18 end
19
20
21 num_images = length(filenames);
22 img_sum = [];
23 img_list = cell(1, num_images);
24 intensity_data = struct();
25 excel_data = {'Imagen', 'Promedio', 'Desviaci n Est ndar', '
       ↪ M ximo', 'M nimo', 'Contraste de Speckle'};
26
```

```
27
28 for i = 1:num_images
29     img = imread(fullfile(pathname, filenames{i}));
30     img_list{i} = img;
31     if isempty(img_sum)
32         img_sum = double(img);
33     else
34         img_sum = img_sum + double(img);
35     end
36
37     % Calcular estad sticas de intensidad para la imagen actual
38     img_intensities = double(img(:));
39     intensity_mean = mean(img_intensities);
40     intensity_std = std(img_intensities);
41     intensity_max = max(img_intensities);
42     intensity_min = min(img_intensities);
43     speckle_contrast = intensity_std / intensity_mean;
44
45     % Stadistics
46     [~, name, ~] = fileparts(filenames{i});
47     var_name = sprintf('Ipromedio_%s', name);
48     intensity_data.(var_name) = struct('mean', intensity_mean,'std',
       ↪  intensity_std, 'max', intensity_max, 'min', intensity_min
       ↪ , 'speckle_contrast', speckle_contrast);
49
50     % Export Excel
51     excel_data(end+1, :) = {name, intensity_mean, intensity_std,
       ↪ intensity_max, intensity_min, speckle_contrast};
52
53     % Show stadistics
54     fprintf('Imagen %d: %s\n', i, filenames{i});
55     fprintf('  Promedio de intensidad: %.2f\n', intensity_mean);
56     fprintf('  Desviaci n est ndar de intensidad: %.2f\n',
       ↪ intensity_std);
57     fprintf('  Intensidad m xima: %d\n', intensity_max);
58     fprintf('  Intensidad m nima: %d\n', intensity_min);
59     fprintf('  Contraste de speckle: %.2f\n', speckle_contrast);
60 end
61
62 % Average
63 img_avg = img_sum / num_images;
64
```

```
% Saving Average
imwrite(uint8(img_avg), fullfile(pathname, 'imagen_promedio.png'));

%
all_intensities = [];
for i = 1:num_images
    all_intensities = [all_intensities; double(img_list{i}(:))];
end

overall_intensity_mean = mean(all_intensities);
overall_intensity_std = std(all_intensities);
overall_intensity_max = max(all_intensities);
overall_intensity_min = min(all_intensities);
overall_speckle_contrast = overall_intensity_std /
    ↪ overall_intensity_mean;

% Save stadistics
intensity_data.Ipromedio_global = struct('mean',
    ↪ overall_intensity_mean, 'std', overall_intensity_std, 'max',
    ↪ overall_intensity_max, 'min', overall_intensity_min, '
    ↪ speckle_contrast', overall_speckle_contrast);


base_name = filenames{1}(1:end-5); % Asumimos que todas las
    ↪ im genes tienen el mismo prefijo
mat_filename = sprintf('%s_intensity_data.mat', base_name);
save(fullfile(pathname, mat_filename), '-struct', 'intensity_data');

% saving .xls
xls_filename = sprintf('%s_intensity_data.xls', base_name);
xlswrite(fullfile(pathname, xls_filename), excel_data);


% figure;
% subplot(1, 2, 1);
% imshow(uint8(img_avg));
% title('Imagen Promedio');
%
subplot(1, 1, 1);
histogram(all_intensities);
title('Distribuci n de Intensidades');
xlabel('Intensidad');
```

```
102 ylabel('Frecuencia');
103
104 %
105 disp('Estad sticas de intensidad para todas las im genes
    ↪ combinadas:');
106 fprintf('  Promedio de intensidad: %.2f\n', overall_intensity_mean);
107 fprintf('  Desviaci n est ndar de intensidad: %.2f\n',
    ↪ overall_intensity_std);
108 fprintf('  Intensidad m xima: %d\n', overall_intensity_max);
109 fprintf('  Intensidad m nima: %d\n', overall_intensity_min);
110 fprintf('  Contraste de speckle: %.2f\n', overall_speckle_contrast);
```

Appendix C

Algorithm for calculating visibility

```
1
2
3  [filenames, pathname] = uigetfile({'*.jpg;*.png;*.bmp', 'Image Files
       ↪  (*.jpg, *.png, *.bmp)'; ...
4                                     '*.*', 'All Files (*.*)'}, ...
5                                     'Seleccione las im genes a
                                        ↪ analizar', ...
6                                     'MultiSelect', 'on');
7
8  if isequal(filenames, 0)
9      disp('No se seleccion  ninguna imagen.');
10     return;
11 end
12
13 %
14 outputFolder = uigetdir('', 'Seleccione la carpeta para guardar los
       ↪ resultados');
15 if outputFolder == 0
16     disp('No se seleccion  ninguna carpeta.');
17     return;
18 end
19
20 %
21 if ischar(filenames)
22     filenames = {filenames};
23 end
24
25
```

```
outputFilename = fullfile(outputFolder, 'Resultados_Visibilidad.xlsx');


results = cell(length(filenames), 3);


for i = 1:length(filenames)

    img = imread(fullfile(pathname, filenames{i}));


    if size(img, 3) == 3
        img = rgb2gray(img);
    end

    visibilities = zeros(800, 1);

    for row = 1:800
        profile = double(img(row, :)); % Obtener el perfil horizontal


        I_max = max(profile);
        I_min = min(profile);
        visibility = (I_max - I_min) / (I_max + I_min);
        visibilities(row) = visibility;
    end


    avg_visibility = mean(visibilities);
    std_visibility = std(visibilities);


    results{i, 1} = filenames{i};
    results{i, 2} = avg_visibility;
    results{i, 3} = std_visibility;

    fprintf('Promedio y desviaci n est ndar calculados para la imagen %s\n', filenames{i});
end

```

```
65
66 resultsTable = cell2table(results, 'VariableNames', {'Imagen', '
   ↪ Promedio_Visibilidad', 'Desviacion_Estandar'});
67 writetable(resultsTable, outputFilename);
68
69 disp('Proceso de c lculo de visibilidad completado y resultados
   ↪ almacenados.');
```

Appendix D

Auto-focus Metrics algorithm

```
1
2  clc;
3  clear;
4  close all;
5
6  %%
7  config = struct();
8  config.lambda = 0.532;
9  config.L = 40000;
10 config.dx = 2;
11 config.step_size = 100;
12 config.ruta = 'C:\Users\maomm\OneDrive\Documentos\TESIS\experimentos
   ↪ \2025\1 - febrero\200225\281024\h2\';
13 config.inicio_busqueda = 0;
14
15
16 metricas = {'Varianza', 'Gradiente', 'Entropia', 'ContrasteLocal', '
   ↪ SSIM'};
17 metodos = {'Fresnel', 'EspectroAngular'};
18
19
20 datos_completos = cell(0,6);
21
22 min_max_metrics = struct('Varianza', [inf, -inf],'Gradiente', [inf,
   ↪ -inf],'Entropia',[inf, -inf],'ContrasteLocal', [inf, -inf],'
   ↪ SSIM', [inf, -inf]);
23
24 resultados_optimos = cell(0,7);
25
```

```
26
27 holograma = im2double(imread(fullfile(config.ruta, 'h2.bmp')));
28 if size(holograma, 3) == 3
29     holograma = rgb2gray(holograma);
30 end
31 [NY, NX] = size(holograma);
32
33 % SSIM (Este es provisional)
34 holograma_ssim = (holograma - min(holograma(:))) ./ (max(holograma
       ↪ (:)) - min(holograma(:)) + eps);
35
36
37 [fx, fy] = meshgrid(...
38     (-NX/2:NX/2-1)/(NX*config.dx), ...
39     (-NY/2:NY/2-1)/(NY*config.dx));
40
41
42 for metodo = 1:length(metodos)
43     optimos = struct();
44     for met = 1:length(metricas)
45         if strcmp(metricas{met}, 'Entropia')
46             optimos.(metricas{met}) = struct('valor', inf, '
                   ↪ distancia', -1, 'desviacion', 0);
47         else
48             optimos.(metricas{met}) = struct('valor', -inf, '
                   ↪ distancia', -1, 'desviacion', 0);
49         end
50     end
51
52     for z = config.inicio_busqueda:config.step_size:config.L
53         % C lculo del kernel de propagaci n
54         if metodo == 1
55             H = exp(1i*(2*pi/config.lambda)*z) .* exp(-1i*pi*config.
                   ↪ lambda*z*(fx.^2 + fy.^2));
56         else
57             H = exp(1i*(2*pi/config.lambda)*z*sqrt(1 - (config.
                   ↪ lambda^2)*(fx.^2 + fy.^2)));
58         end
59
60
61         campo = ifft2(ifftshift(fftshift(fft2(holograma)) .* H));
62         amplitud = abs(campo);
```

```
63
64      amplitud_normalizada = (amplitud - min(amplitud(:))) ./ (max
           ↪ (amplitud(:)) - min(amplitud(:)) + eps);
65
66
67      [var_val, var_std] = calcularVarianza(amplitud);
68      [grad_val, grad_std] = calcularGradiente(amplitud);
69      [ent_val, ent_std] = calcularEntropia(amplitud);
70      [cont_val, cont_std] = calcularContraste(amplitud);
71      [ssim_val, ssim_std] = calcularSSIM(amplitud_normalizada,
           ↪ holograma_ssim);
72
73      metricas_val = struct('Varianza', var_val,'Gradiente',
           ↪ grad_val,'Entropia', ent_val,'ContrasteLocal',
           ↪ cont_val,'SSIM', ssim_val);
74
75      metricas_std = struct('Varianza', var_std,'Gradiente',
           ↪ grad_std,'Entropia', ent_std,'ContrasteLocal',
           ↪ cont_std,'SSIM', ssim_std);
76
77
78      for met = 1:length(metricas)
79          current_val = metricas_val.(metricas{met});
80          min_max_metrics.(metricas{met}) = [...
81              min(current_val, min_max_metrics.(metricas{met})(1))
                   ↪ , max(current_val, min_max_metrics.(metricas{
                   ↪ met})(2))];
82      end
83
84
85      for met = 1:length(metricas)
86          datos_completos = [datos_completos; {metodos{metodo},
               ↪ metricas{met},z,metricas_val.(metricas{met}),NaN,
               ↪ ...  % ValorNorm
87              metricas_std.(metricas{met})}];
88
89          current_val = metricas_val.(metricas{met});
90          current_std = metricas_std.(metricas{met});
91          if (strcmp(metricas{met}, 'Entropia'))
92              if current_val < optimos.(metricas{met}).valor
93                  optimos.(metricas{met}).valor = current_val;
94                  optimos.(metricas{met}).distancia = z;
```

```
95                      optimos.(metricas{met}).desviacion = current_std
                           ↪ ;
96                  end
97              else
98                  if current_val > optimos.(metricas{met}).valor
99                      optimos.(metricas{met}).valor = current_val;
100                     optimos.(metricas{met}).distancia = z;
101                     optimos.(metricas{met}).desviacion = current_std
                           ↪ ;
102                 end
103             end
104         end
105     end
106
107     for met = 1:length(metricas)
108         resultados_optimos = [resultados_optimos; { metodos{metodo},
               ↪ metricas{met},optimos.(metricas{met}).distancia,
               ↪ optimos.(metricas{met}).valor,NaN, % ValorNorm
109              optimos.(metricas{met}).desviacion,char("M nimo" +
                    ↪ string(strcmp(metricas{met}, 'Entropia')) + "
                    ↪ M ximo")}];
110     end
111 end
112
113
114 for i = 1:size(datos_completos,1)
115     metrica = datos_completos{i,2};
116     min_val = min_max_metrics.(metrica)(1);
117     max_val = min_max_metrics.(metrica)(2);
118     datos_completos{i,5} = (datos_completos{i,4} - min_val) / (
           ↪ max_val - min_val + eps);
119
120     if strcmp(metrica, 'Entropia')
121         datos_completos{i,5} = 1 - datos_completos{i,5};
122     end
123 end
124
125 for i = 1:size(resultados_optimos,1)
126     metrica = resultados_optimos{i,2};
127     min_val = min_max_metrics.(metrica)(1);
128     max_val = min_max_metrics.(metrica)(2);
```

```
129     resultados_optimos{i,5} = (resultados_optimos{i,4} - min_val) /
            ↪ (max_val - min_val + eps);
130
131     if strcmp(metrica, 'Entropia')
132         resultados_optimos{i,5} = 1 - resultados_optimos{i,5};
133     end
134 end
135
136
137 nombre_archivo = fullfile(config.ruta, 'Resultados_Completos_h2.xlsx
        ↪ ');
138 if exist(nombre_archivo, 'file'), delete(nombre_archivo); end
139
140
141 tabla_completa = cell2table(datos_completos,...
142     'VariableNames', {'Metodo','Metrica','Distancia','ValorCrudo','
            ↪ ValorNormalizado','DesviacionEstandar'});
143 writetable(tabla_completa, nombre_archivo, 'Sheet', 'Datos_Completos
        ↪ ');
144
145
146 tabla_optimos = cell2table(resultados_optimos,...
147     'VariableNames', {'Metodo','Metrica','MejorDistancia','
            ↪ ValorCrudo','ValorNormalizado','DesviacionEstandar','
            ↪ TipoOptimizacion'});
148 writetable(tabla_optimos, nombre_archivo, 'Sheet', '
        ↪ Resultados_Optimos');
149 %% For acces to the auxiliar functions open the url: "https://drive.
        ↪ google.com/file/d/1qQFcfiskb-bqYJcjqmU2-VwsCuCoucOd/view?usp=
        ↪ drive_link"
```

Bibliography

[1] E. Wolf. New theory of partial coherence in the space–frequency domain. part i: spectra and cross spectra of steady-state sources. *J. Opt. Soc. Am.*, 72(3):343–351, Mar 1982. URL: https://opg.optica.org/abstract.cfm?URI=josa-72-3-343, doi:10.1364/JOSA.72.000343.

[2] A. S. Galande, H. P. Gurram, A. P. Kamireddy, V. S. Venkatapuram, Q. Hasan, and R. John. Quantitative phase imaging of biological cells using lensless inline holographic microscopy through sparsity-assisted iterative phase retrieval algorithm. *Journal of Applied Physics*, 132(24):243102, 12 2022. arXiv:https://pubs.aip.org/aip/jap/article-pdf/doi/10.1063/5.0123677/16520829/243102_1_online.pdf, doi:10.1063/5.0123677.

[3] H. Kim, G. Song, J. You, C. Lee, and M. Jang. Deep learning for lensless imaging. *J. Kor. Phy. Soc.*, 81, 02 2022. doi:10.1007/s40042-022-00412-2.

[4] X. Zhang, B. Wang, S. Li, K. Liang, H. Guan, Q. Chen, and C. Zuo. Lensless imaging with a programmable fresnel zone aperture. *Sci. Adv.*, 11(12):eadt3909, 2025. URL: https://www.science.org/doi/abs/10.1126/sciadv.adt3909, arXiv:https://www.science.org/doi/pdf/10.1126/sciadv.adt3909, doi:10.1126/sciadv.adt3909.

[5] G. Gbur. *Singular Optics*. 11 2016. doi:10.1201/9781315374260.

[6] K. M. Molony, B. M. Hennelly, D. P. Kelly, and T. J. Naughton. Reconstruction algorithms applied to in-line gabor digital holographic microscopy. *Opt. Com.*, 283(6):903–909, 2010. URL: https://www.sciencedirect.com/science/article/pii/S0030401809011419, doi:10.1016/j.optcom.2009.11.012.

[7] C. P. D'Almeida. *Development of lens-free holographic microscopes using multiheight and multispectral phase recovery methods*. PhD thesis, Instituto de Física de São Carlos, Universidade de São Paulo, São Carlos, 2023.

[8] S. O. Isikman, W. Bishara, and A. Ozcan. Partially coherent lensfree tomographic microscopy [invited]. *Appl. Opt.*, 50(34):H253–H264, Dec 2011. URL: https://opg.optica.org/ao/abstract.cfm?URI=ao-50-34-H253, doi:10.1364/AO.50.00H253.

[9] Y. Bian, W. Wang, A. Hussian, C. Kuang, H. Li, and X. Liu. Experimental analysis and designing strategies of lens-less microscopy with partially coherent illumination. *Opt. Com.*, 434:136–144, 2019. URL: https://www.sciencedirect.com/science/article/pii/S0030401818309106, doi:10.1016/j.optcom.2018.10.035.

[10] A. Hassan, S. Khan, K. Rasul, and A. Hussain. Lensless on-chip led array microscope using amplitude and phase masks. *J. Opt. Soc. Am.*, 37:3652–3659, 11 2020. doi:10.1364/JOSAB.396076.

[11] J.M. Rodenburg. Ptychography and related diffractive imaging methods. 150:87–184, 2008. URL: https://www.sciencedirect.com/science/article/pii/S1076567007000031, doi:10.1016/S1076-5670(07)00003-1.

[12] Dennis Gabor. Holography, 1948-1971. *Science*, 177(4046):299–313, 1972. URL: https://www.science.org/doi/abs/10.1126/science.177.4046.299, arXiv:https://www.science.org/doi/pdf/10.1126/science.177.4046.299, doi:10.1126/science.177.4046.299.

[13] P. Etchepareborda, P. Connolly, J. Henneberger, and J. Crosier. Distortion free angular spectrum method for digital inline holographic microscopy. *Dig. Hol. and 3-D Imag. 2022*, page Th2A.3, 2022. URL: https://opg.optica.org/abstract.cfm?URI=DH-2022-Th2A.3, doi:10.1364/DH.2022.Th2A.3.

[14] F. Zhang, G. Pedrini, and W. Osten. Reconstruction algorithm for high-numerical-aperture holograms with diffraction-limited resolution. *Opt. Lett.*, 31(11):1633–1635, Jun 2006. URL: https://opg.optica.org/ol/abstract.cfm?URI=ol-31-11-1633, doi:10.1364/OL.31.001633.

[15] B. K. Chen, P. Sidorenko, O. Lahav, O. Peleg, and O. Cohen. Multiplexed single-shot ptychography. *Opt. Lett.*, 43(21):5379–5382, Nov 2018. URL: https://opg.optica.org/ol/abstract.cfm?URI=ol-43-21-5379, doi:10.1364/OL.43.005379.

[16] L. Waller, S. Shan Kou, Colin J. R. Sheppard, and G. Barbastathis. Phase from chromatic aberrations. *Opt. Exp*, 18(22):22817–22825, Oct 2010. URL: https://opg.optica.org/oe/abstract.cfm?URI=oe-18-22-22817, doi:10.1364/OE.18.022817.

[17] T. Colomb, F. Montfort, Jonas K., N. Aspert, E. Cuche, A. Marian, F. Charrière, S. Bourquin, P. Marquet, and C. Depeursinge. Numerical parametric lens for shifting, magnification, and complete aberration compensation in digital holographic microscopy. *J. Opt. Soc. Am. A*, 23(12):3177–3190, Dec 2006. URL: https://opg.optica.org/josaa/abstract.cfm?URI=josaa-23-12-3177, doi:10.1364/JOSAA.23.003177.

[18] S Amann, M. von Witzleben, and S. Breuer. 3d-printable portable open-source platform for low-cost lens-less holographic cellular imaging. *Sci. Rep.*, 9, 08 2019. doi:10.1038/s41598-019-47689-1.

[19] H. Ram, A. Galande, and R. John. Nanometric depth phase imaging using low-cost on-chip lensless inline holographic microscopy. *Opt. Eng.*, 59, 10 2020. doi:10.1117/1.OE.59.10.104105.

[20] R. Corman. *2D/3D lensless imaging : prototype and applications*. Number 2020UPASS042. March 2020. URL: https://theses.hal.science/tel-02944689.

[21] Y. Rivenson, Y. Zhang, H. Günaydın, D. Teng, and A. Ozcan. Phase recovery and holographic image reconstruction using deep learning in neural networks. *Light Sci. Appl.*, 7:17141, 2017. doi:10.1038/lsa.2017.141.

[22] C. L. Curl, C. J. Bellair, T. Harris, B. E. Allman, P. J. Harris, A. G. Stewart, A. Roberts, K. A. Nugent, and L. M. Delbridge. Refractive index measurement in viable cells using quantitative phase-amplitude microscopy and confocal microscopy. *Cytometry Part A*, 65:88–92, 2005. doi:10.1002/cyto.a.20134.

[23] J. Birdi, S. Rajora, M. Butola, and K. Khare. True 3d reconstruction in digital holography. *J. of Phys. Phot.*, 2(4):044004, oct 2020. doi:10.1088/2515-7647/abb586.

[24] J. Jonkman, C. M. Brown, and R. W. Cole. Chapter 7 - quantitative confocal microscopy: Beyond a pretty picture. In J. C. Waters and T. Wittman, editors, *Quantitative Imaging in Cell Biology*, volume 123 of *Methods in Cell Biology*, pages 113–134. Academic Press, 2014. URL: https://www.sciencedirect.com/science/article/pii/B9780124201385000070, doi:10.1016/B978-0-12-420138-5.00007-0.

[25] M. Molaei and J. Sheng. Imaging bacterial 3d motion using digital in-line holographic microscopy and correlation-based de-noising algorithm. *Opt. Express*, 22(26):32119–32137, Dec 2014. URL: https://opg.optica.org/oe/abstract.cfm?URI=oe-22-26-32119, doi:10.1364/OE.22.032119.

[26] M. Sanz, J. Á. Picazo-Bueno, L. Granero, J. García, and V. Micó. Multi-illumination single-holographic-exposure lensless fresnel (mishelf) microscopy using 4 channels. *Imaging and Applied Optics 2019 (COSI, IS, MATH, pcAOP)*, page JW2A.1, 2019. URL: https://opg.optica.org/abstract.cfm?URI=MATH-2019-JW2A.1.

[27] J. W. Goodman. *Introduction to Fourier Optics*. Roberts & Company, 3rd edition, 2005.

[28] L. Repetto, F. Pellistri, E. Piano, and C. Pontiggia. Gabor's hologram in a modern perspective. *American Journal of Physics*, 72(7):964–967, 07 2004. arXiv:https://pubs.aip.org/aapt/ajp/article-pdf/72/7/964/8505383/964_1_online.pdf, doi:10.1119/1.1652041.

[29] T. C. Magalhães and J. M. Rebordão. Simulation of partially coherent light propagation using parallel computing devices. In *Proc. SPIE 10453, 104531U*, 2017. doi:10.1117/12.2272339.

[30] H. Tobon-Maya, S. Zapata-Valencia, E. Zora-Guzmán, C. Buitrago-Duque, and J. Garcia-Sucerquia. Open-source, cost-effective, portable, 3d-printed digital lensless holographic microscope. *Appl. Opt.*, 60(4):A205–A214, Feb 2021. URL: https://opg.optica.org/ao/abstract.cfm?URI=ao-60-4-A205, doi:10.1364/AO.405605.

[31] T. Shimobaba, J. Weng, T. Sakurai, N. Okada, T. Nishitsuji, N. Takada, A. Shiraki, N. Masuda, and T. Ito. Computational wave optics library for c++: Cwo++ library. *Comp. Phys. Com.*, 183(5):1124–1138, 2012. doi:10.1016/j.cpc.2011.12.027.

[32] J. Garcia-Sucerquia, W. Xu, S. K. Jericho, P. Klages, M. H. Jericho, and H. J. Kreuzer. Digital in-line holographic microscopy. *Appl. Opt.*, 45(5):836–850, Feb 2006. URL: https://opg.optica.org/ao/abstract.cfm?URI=ao-45-5-836, doi:10.1364/AO.45.000836.

[33] T. van Dijk, G. Gbur, and T. D. Visser. Shaping the focal intensity distribution using spatial coherence. *J. Opt. Soc. Am. A*, 25(3):575–581, Mar 2008. doi:10.1364/JOSAA.25.000575.

[34] G. Gbur and T. D. Visser. Can spatial coherence effects produce a local minimum of intensity at focus? *Opt. Lett.*, 28(18):1627–1629, Sep 2003. doi:10.1364/OL.28.001627.

[35] Y. Shen, H. Sun, D. Peng, Y. Chen, Q. Cai, D. Wu, F. Wang, Y. Cai, and S. A. Ponomarenko. Optical image reconstruction in 4f imaging system: Role of spatial coherence structure engineering. *Applied Physics Letters*, 118(18):181102, 05 2021. arXiv:https://pubs.aip.org/aip/apl/article-pdf/doi/10.1063/5.0046288/13008374/181102_1_online.pdf, doi:10.1063/5.0046288.

[36] B. Yinxu, T. T. Xing, K. Jiao, Q. Kong, Jiaxiong W., Xiaofei Y., Shenmin Y., Yannan J., Renbing S., Hua S., and Cuifang K. Computational portable microscopes for point-of-care-test and tele-diagnosis. *Cells*, 11(22), 2022. URL: https://www.mdpi.com/2073-4409/11/22/3670, doi:10.3390/cells11223670.

[37] M. W. Hyde. Independently controlling stochastic field realization magnitude and phase statistics for the construction of novel partially coherent sources. *Photonics*, 8(2), 2021. URL: https://www.mdpi.com/2304-6732/8/2/60, doi:10.3390/photonics8020060.

[38] Y. Peng, S. Choi, J. Kim, and G. Wetzstein. Speckle-free holography with partially coherent light sources and camera-in-the-loop calibration. *Sci. Adv.*, 7, 11 2021. doi:10.1126/sciadv.abg5040.

[39] C. Buitrago-Duque, H. Tobón-Maya, A. Gómez-Ramírez, S. I. Zapata-Valencia, M. J. Lopera, C. Trujillo, and J. Garcia-Sucerquia. Open-access database for digital lensless holographic microscopy and its application on the improvement of deep-learning-based autofocusing models. *Appl. Opt.*, 63(7):B49–B58, Mar 2024. doi:10.1364/AO.507412.

[40] D. Naik, G. Pedrini, M. Takeda, and W. Osten. Spectrally resolved incoherent holography: 3d spatial and spectral imaging using a mach–zehnder radial-shearing interferometer. *Optics Letters*, 39:1857–1860, 03 2014. doi:10.1364/OL.39.001857.

[41] J. Pu, S. Nemoto, and X. Liu. Beam shaping of focused partially coherent beams by use of the spatial coherence effect. *Appl. Opt.*, 43(28):5281–5286, Oct 2004. doi:10.1364/AO.43.005281.

[42] S. Oh, C. Escobedo, and A. Brolo. *Miniature Fluidic Devices for Rapid Biological Detection*. 01 2018. doi:10.1007/978-3-319-64747-0.

[43] B. M. and Wolf E. *Principles of Optics*. Cambridge University Press, 7th edition, 1999.

[44] P. Picart, M. Gross, P. Marquet, S. Coëtmellec, D. Lebrun, M. Brunel, J. Desse, A. El Mallahi, C. Minetti, F. Dubois, B. Rappaz, N. Pavillon, M. Georges, N. Verrier, and M. Atlan. *New Techniques in Digital Holography*. 02 2015.

[45] J. W. Goodman. *Statistical Optics*. Wiley Series in Pure and Applied Optics. John Wiley & Sons, Hoboken, NJ, 2 edition, 2015.

[46] T. C. Poon. *Digital Holography and Three-Dimensional Display*. 01 2006. doi:10.1007/0-387-31397-4.

[47] K. Khare, M. Butola, and S. Rajora. *Fourier Optics and Computational Imaging*. 01 2023. doi:10.1007/978-3-031-18353-9.

[48] O. Korotkova. *Theoretical Statistical Optics*. 09 2021. doi:10.1142/12230.

[49] A. T. Friberg and E. Wolf. Relationships between the complex degrees of coherence in the space–time and in the space–frequency domains. *Opt. Lett.*, 20(6):623–625, Mar 1995. URL: https://opg.optica.org/ol/abstract.cfm?URI=ol-20-6-623, doi:10.1364/OL.20.000623.

[50] A. S. Ostrovsky, G. Martínez-Niconoff, P. Martínez-Vara, and Miguel A. Olvera-Santamaría. The van cittert-zernike theorem for electromagnetic fields. *Opt. Express*, 17(3):1746–1752, Feb 2009. URL: https://opg.optica.org/oe/abstract.cfm?URI=oe-17-3-1746, doi:10.1364/OE.17.001746.

[51] Olga Korotkova. *Random Light Beams: Theory and Applications*. 01 2014. doi:10.1201/b15471.

[52] G. Piquero, R. Borghi, and M. Santarsiero. Gaussian schell-model beams propagating through polarization gratings. *J. Opt. Soc. Am. A*, 18(6):1399–1405, Jun 2001. URL: https://opg.optica.org/josaa/abstract.cfm?URI=josaa-18-6-1399, doi:10.1364/JOSAA.18.001399.

[53] Milo Hyde. *Computational Optical Coherence and Statistical Optics*. 09 2023. doi:10.1117/3.2652240.

[54] F. J. Torcal-Milla and L. M. Sanchez-Brea. Gaussian-schell-model beams propagating through rough gratings. *J. Opt. Soc. Am. A*, 28(3):308–313, Mar 2011. URL: https://opg.optica.org/josaa/abstract.cfm?URI=josaa-28-3-308, doi:10.1364/JOSAA.28.000308.

[55] J. C. G. de Sande, Rosario Martínez-Herrero, Gemma Piquero, Massimo Santarsiero, and Franco Gori. Pseudo-schell model sources. *Opt. Express*, 27(4):3963–3977, Feb 2019. URL: https://opg.optica.org/oe/abstract.cfm?URI=oe-27-4-3963, doi:10.1364/OE.27.003963.

[56] M. Zhong. *Propagation of Partially Coherent Light in Optical Systems*. Friedrich-Schiller-Universität Jena, 2017. URL: https://books.google.com.mx/books?id=yEJ7OAEACAAJ.

[57] G. Gbur. Partially coherent beam propagation in atmospheric turbulence. *Progress in Optics*, 59:225–281, 2014. doi:10.1364/josaa.31.002038.

[58] G. Wu, B. Luo, S. Yu, A. Dang, and H. Guo. The propagation of electromagnetic gaussian–schell model beams through atmospheric turbulence in a slanted path. *J. Opt.*, 13(3):035706, jan 2011. URL: https://dx.doi.org/10.1088/2040-8978/13/3/035706, doi:10.1088/2040-8978/13/3/035706.

[59] S. O. Isikman, W. Bishara, and A. Ozcan. Partially coherent lensfree tomographic microscopy (invited). *Appl. Opt.*, 50(34):H253–H264, Dec 2011. URL: https://opg.optica.org/ao/abstract.cfm?URI=ao-50-34-H253, doi:10.1364/AO.50.00H253.

[60] T.C. Poon and year = 2014 month = 03 pages = title = Introduction to Modern Digital Holography with MATLAB isbn = 9781107016705 doi = 10.1017/CBO9781139061346 Liu, J.P.

[61] Z. Mei. Generalized schell-model sources. *Opt. Express*, 28(26):39058–39066, Dec 2020. URL: https://opg.optica.org/oe/abstract.cfm?URI=oe-28-26-39058, doi:10.1364/OE.413241.

[62] O. Korotkova, Serkan Sahin, and Elena Shchepakina. Multi-gaussian schell-model beams. *J. Opt. Soc. Am. A*, 29(10):2159–2164, Oct 2012. URL: https://opg.optica.org/josaa/abstract.cfm?URI=josaa-29-10-2159, doi:10.1364/JOSAA.29.002159.

[63] G. Gbur and T.D. Visser. Chapter 5 - the structure of partially coherent fields. volume 55 of *Progress in Optics*, pages 285–341. Elsevier, 2010. URL: https://www.sciencedirect.com/science/article/pii/B9780444537058000059, doi:10.1016/B978-0-444-53705-8.00005-9.

[64] A. Beck and M. Teboulle. A fast iterative shrinkage-thresholding algorithm for linear inverse problems. *SIAM Journal on Imaging Sciences*, 2(1):183–202, 2009. arXiv:https://doi.org/10.1137/080716542, doi:10.1137/080716542.

[65] L. I. Rudin, S. Osher, and E. Fatemi. Nonlinear total variation based noise removal algorithms. *Physica D: Nonlinear Phenomena*, 60(1):259–268, 1992. URL: https://www.sciencedirect.com/science/article/pii/016727899290242F, doi:10.1016/0167-2789(92)90242-F.

[66] C. E. Shannon. A mathematical theory of communication. *Bell System Technical Journal*, 27(3):379–423, 1948.

[67] F. Niknam, H. Qazvini, and H. Latifi. Holographic optical field recovery using a regularized untrained deep decoder network. *Scientific Reports*, 11(1):10903, may 2021. doi:10.1038/s41598-021-90312-5.

[68] E. Hecht. *Optics*. Springer-Verlag, 5 edition, 2002.

[69] J. W. Goodman. *Speckle Phenomena in Optics: Theory and Applications*. Roberts and Company Publishers, Englewood, CO, 2007.

[70] D. S. Mehta, D. N. Naik, R. K. Singh, and M. Takeda. Laser speckle reduction by multimode optical fiber bundle with combined temporal, spatial, and angular diversity. *Appl. Opt.*, 51(12):1894–1904, Apr 2012. URL: https://opg.optica.org/ao/abstract.cfm?URI=ao-51-12-1894, doi:10.1364/AO.51.001894.

[71] J. Manni and J. Goodman. Versatile method for achieving 1 *Optics Express*, 20:11288–11315, 05 2012. doi:10.1364/OE.20.011288.

[72] M. Wang, S. Feng, and J. Wu. Pixel super-resolution lensless in-line holographic microscope with hologram segmentation. *Chin. Opt. Lett.*, 17(11):110901, Nov 2019. URL: https://opg.optica.org/col/abstract.cfm?URI=col-17-11-110901.